

# **Characteristics of siphon flow under submerged discharge conditions**

Warda Mansour Ahmed

A Thesis  
In  
The Department  
of  
Building, Civil and Environmental Engineering

Presented in Partial Fulfillment of the Requirements  
for the Degree of  
Doctor of Philosophy (Civil Engineering) at  
Concordia University  
Montreal, Quebec, Canada

April 2021

© Warda Ahmed, 2021

**CONCORDIA UNIVERSITY**  
**SCHOOL OF GRADUATE STUDIES**

This is to certify that the thesis prepared

By:                   Warda Ahmed

Entitled:           Characteristics of siphon flow under submerged discharge  
                          conditions

and submitted in partial fulfillment of the requirements for the degree of

Doctor Of Philosophy (Civil Engineering)

complies with the regulations of the University and meets the accepted standards with respect to originality and quality.

Signed by the final examining committee:

_____	Chair
Dr. Rabindranath Raut	
_____	External Examiner
Dr. Jueyi Sui	
_____	External to Program
Dr. Georgios Vatistas	
_____	Examiner
Dr. Michelle Nokken	
_____	Examiner
Dr. Chunjiang An	
_____	Thesis Co-Supervisor
Dr. Samuel Li	
_____	Thesis Co-Supervisor
Dr. Amruthur Ramamurthy	

Approved by

\_\_\_\_\_  
Dr. Michelle Nokken, Graduate Program Director

4/12/2021

\_\_\_\_\_  
Dr. Mourad Debbabi, Dean  
Gina Cody School of Engineering and Computer Science

## **Abstract**

### **Characteristics of siphon flow under submerged discharge conditions**

**Warda Mansour Ahmed, Ph.D.**

**Concordia University, 2021**

Water reservoirs serve such essential purposes as water supply, irrigation, and hydroelectric power developments. Their effective and safe operations need reliable hydraulic structures for flow control. Siphon spillways are a flow control structure, with two main advantages: 1) no moving parts required and thus less susceptible to breakdown; 2) the ability to pass full discharge with a minimal increase of reservoir water level. The second advantage makes it easier to maintain target water levels as water resources while to ensure safe operations. The design of a siphon spillway uses one discharge head only, termed the design head, which is derived from statistical analysis of hydrological data for the reservoir region. However, under climate change, most existing siphons have been or are expected to be subject to actual discharge heads larger than their design heads. In other words, climate change results in submerged exit condition for siphon flow.

Previous studies of siphons focus on their hydraulic performance under free discharge condition. How submergence affects the flow is a question, not addressed previously. The flow over the crest of a siphon is highly curved. It is a challenge to deal with the curved boundary surface of the crest in siphon analysis. Streamline curvatures, three-dimensional vorticities and other subtle characteristics of the velocity and pressure fields remain to be discovered. Existing studies limit to a qualitative description of siphon flow and oversimplify flow mechanisms. The purpose of this research is to improve our understanding of siphon flow characteristics in a range of submerged exit conditions; to reveal any changes in the hydraulic performance of siphons, compared to free discharge conditions; and ultimately to contribute to an improved design of siphons. This research took the approach of combining laboratory experiments with mathematical modelling. The experiments used a scaled model siphon. It was fabricated and tested in the Hydraulics Laboratory at Concordia University. A series of experiments were conducted to determine the discharge coefficient in a range of flow rates. A three-dimensional computational fluid dynamics (CFD) model was established for predicting the velocity and pressure fields as well as turbulence quantities. The CFD model used mesh refinement for regions close to solid boundaries and computed two-phase flow. The free surface of reservoir was tracked using the volume-of-fluid (VOF) method. Turbulence closure was obtained using the RNG k- $\epsilon$  model.

The CFD model predicted detailed distributions of the flow field, including curvilinear flow features in the crest region. The flow characteristics corresponded to various conditions of submergence at the downstream exit of the siphon conduit, and included primary flow velocity, secondary flow velocity, turbulence kinetic energy, and pressure. The predicted discharge coefficient compared well with experimental data. The predicted mean-flow velocities were validated using estimates from the potential flow theory.

The experimental and computational results lead to the following findings: 1) The flow in the upstream reservoir is relatively uniform, with smooth movement toward the siphon entrance. At the entrance, the flow contracts, causing the pressure to drop below the hydrostatic pressure level in the upper corner of the entrance. Under the impact of centrifugal forces, the flow at the crest is forced to move in the extrados direction, causing secondary flow and an increased velocity above the crest. 2) The velocity rapidly increases near the crest, and reaches the maximum at a very small height from the crest surface. In the zone above the boundary layer, the velocity decreases gradually before it starts to rapidly decrease near the crown surface. 3) Flow separation occurs just a short distance downstream of the crest. Eddies start to form on the crest and develop along the lower leg of the siphon. Further downstream, the flow contracts by a deflector, creating flow separation on the downstream side. 4) The pressures differ along the siphon conduit, with negative values in the crest region. The pressure decrease is proportional to the increase of velocity. Negative pressures at the crest surface may drop to water vapour pressure at the prototype scale. 5) The discharge coefficient is a parameter of practical importance. It allows one-to-one determination of siphon discharge from the head which is simple to measure. Values of the discharge coefficient range from 0.62 to 0.68 under submerged exit conditions. These values are larger than those under free discharge conditions.

This study has contributed to a better understanding of flow behaviours in a region bounded by curved boundaries. The CFD modelling strategies discussed in this research can be applied to analyse complex flows in similar hydraulic structures. The pressure data reported can possibly be used to assess risks of cavitation in siphon spillways. In conclusion, the siphon flow is a complex flow, with curvatures, three dimensionality and turbulence. Through laboratory experiments and mathematical modelling, this research sheds lights on the flow characteristics such as discharge performance, velocity distribution, and pressure distribution.

## **Acknowledgements**

It is great pleasure to express my sincere appreciation to Dr. S. Samuel Li, Department of Building, Civil, and Environmental Engineering for his valuable guidance, advice, and instructions. It is great honor to work under his supervision.

I would like to acknowledge my thanks to Dr. A. S. Ramamurthy, Department of Building, Civil, and Environmental Engineering for his encouragement, and his kind supervision.

Cordial and special thanks to my beloved husband and our dearly loved kids, who gave me enormous encouragement and support along this journey. I owe them very special gratitude.

Most importantly to my mother and siblings who despite the distance have always been the source of strength towards the accomplishment of this thesis.

I acknowledge with gratitude the financial support I received from The Libyan Ministry of Education, Sirte University and Gina Cody School of Engineering and Computer Science at Concordia University.

## Table of Contents

Abstract.....	iii
Table of Contents.....	vi
List of Figures.....	ix
List of Tables.....	xv
Notation.....	xvi
1. Introduction.....	1
1.1. Background.....	1
1.2. Classification of spillways.....	1
1.3. Cavitation potential.....	8
1.4. Important issues.....	8
1.5. Research objectives.....	10
1.6. Research contributions.....	10
2. Literature Review.....	11
2.1. Introduction.....	11
2.2. Experimental investigation.....	13
2.3. Analytical investigation.....	16
2.4. Numerical investigation.....	23
3. Laboratory Experiments of Siphon Flow.....	27
3.1. Introduction.....	27
3.2. Experimental setup.....	29
3.2.1 Flume system.....	29
3.2.2 Head water tank.....	30
3.2.3 Siphon.....	31
3.2.4 V-notch tank.....	33
3.2.5 Flow control.....	34
3.2.6 Measurement instruments.....	34
3.3. Methods for data analysis.....	36

3.3.1	Determination of flow rate through the siphon conduit .....	36
3.3.2	Determination of the discharge coefficient of siphon flow .....	37
3.4	Experimental results and discussions .....	38
3.5	Conclusions .....	40
4.	Numerical Modelling of Flow through Siphon Spillway .....	42
4.1.	Introduction .....	42
4.2.	Reynolds-averaged continuity and momentum equations.....	43
4.2.1	Continuity equations.....	44
4.2.2	The volume of fluid method .....	44
4.2.3	Momentum equations .....	45
4.3.	Turbulence closure .....	46
4.3.1	The standard k- $\epsilon$ model .....	47
4.3.2	The RNG k- $\epsilon$ model .....	48
4.3.3	Realizable k- $\epsilon$ model .....	49
4.4.	Description of model parameters.....	50
4.4.1	Geometry .....	50
4.4.2	Free surface tracking .....	51
4.4.3	Grid generation .....	52
4.5.	Simulation setup .....	55
4.5.1	Boundary conditions.....	55
4.5.2	Discretization.....	56
4.5.3	Initialization.....	56
4.5.4	Solution procedure.....	57
4.5.5	Solution accuracy .....	57
4.6.	Results .....	59
4.6.1	Independence of model results on mesh configurations.....	59
4.6.2	Evaluation of the suitability of models for turbulence closure.....	61
4.6.3	Velocity distribution.....	63

4.6.4	The pressure distribution over the siphon crest .....	72
4.6.5	Comparison of discharge coefficient $C_d$ .....	77
4.7.	Conclusions .....	79
5.	Distributions of Mean Flow Velocity and Turbulence .....	81
5.1.	Introduction .....	81
5.2.	Energy cascade .....	81
5.3.	Energy spectrum .....	83
5.4.	Turbulence intensity and turbulence kinetic energy .....	84
5.5.	Flow separation .....	85
5.6.	Distributions of the mean flow velocity .....	86
5.6.1	Longitudinal distribution of flow velocity .....	88
5.6.2	Cross-sectional distribution of flow velocity .....	90
5.7.	Distribution of turbulence kinetic energy .....	100
5.7.1	Longitudinal distribution of turbulence kinetic energy .....	100
5.7.2	Cross-sectional distribution of turbulence kinetic energy .....	103
5.8	Conclusions .....	107
6.	Conclusions .....	109
6.1.	Discussions and conclusions .....	109
6.2.	Further studies .....	112
7.	References .....	116
8.	Appendix A: Data sheets of gauge pressures from numerical predictions .....	120

## List of Figures

Figure 1-1. Classification of the outlet-works, (A-1 to A-5, and C-1 to C-5) shown different types of spillways (from Khatsuria, 2004) .....	2
Figure 1-2. Trough spillway ( <a href="http://hydropedia.blogspot.ca/2014/03/spillway.html">http://hydropedia.blogspot.ca/2014/03/spillway.html</a> , accessed on June 1, 2017) and photo of Glory Hole Spillway at Lake Berryessa, California, U.S. ( <a href="https://www.usbr.gov/newsroom/stories/detail.cfm?RecordID=58763">https://www.usbr.gov/newsroom/stories/detail.cfm?RecordID=58763</a> ).....	3
Figure 1-3. Shape of overflow spillway (from Houghtalen et al., 2017) and photo of Cleveland dam overflow spillway in North Vancouver. B.C., Canada. ( <a href="http://www.williamzhang.com/">http://www.williamzhang.com/</a> ) .....	4
Figure 1-4. Longitudinal profile of ogee spillway (from Nalluri and Featherstone, 2009), and photo of Rend Lake Spillway, Illinois, U.S. ( <a href="https://www.pinterest.ca/pin/68609594297759152/">https://www.pinterest.ca/pin/68609594297759152/</a> ). 5	
Figure 1-5. Side channel spillway (Houghtalen et al., 2017) and photo of Revelstoke side channel spillway, Revelstoke, B.C., Canada ( <a href="https://www.pinterest.ca/pin/54817320442348907">https://www.pinterest.ca/pin/54817320442348907</a> ).....	6
Figure 1-6. Typical siphon (Michael D. Meyer, 2005) and photo of Brent Reservoir siphon spillway, London, UK ( <a href="https://canalrivertrust.org.uk/news-and-views/media-centre/filming-and-photography/our-filming-and-photography-locations/brent-reservoir-welsh-harp">https://canalrivertrust.org.uk/news-and-views/media-centre/filming-and-photography/our-filming-and-photography-locations/brent-reservoir-welsh-harp</a> ).....	7
Figure 1-7. Cavitation bubble collapse process (Machado, 2009).....	8
Figure 2-1. General concepts on spillways and siphon.....	12
Figure 2-2. Five flow stages (Head 1971) .....	13
Figure 2-3. Comparison of head-discharge curves for full scale model and 1:5 scale for the siphon (Ervine and Oliver 1980) .....	15
Figure 2-4. Flow over spillway in physical plane (Cassidy 1965) .....	16
Figure 2-5. Free-surface profiles and pressure distributions for standard spillway (Cassidy 1965) .....	17
Figure 2-6. Flow over spillway (Cassidy 1970).....	18
Figure 2-7. Discharge-minimum pressure characteristics of standard spillway (Cassidy 1970)..	19
Figure 2-8. Open channel flow (Dressier 1978) .....	20

Figure 2-9. Curvilinear coordinates defined by channel boundary (Dressier 1978)..... 20

Figure 2-10. Air-regulated siphon model (Ali and Pateman 1980) ..... 21

Figure 2-11. Variation of discharge coefficient with dimensionless head (Tadayon and Ramamurthy 2013) ..... 25

Figure 3-1 Schematic of the experimental setup used to conduct experiments, showing an upstream head tank-section, a siphon section, and a downstream channel-section. Measurement devices include point gauges and a sharp-crested V-notch weir. .... 29

Figure 3-2 Photo of the hydraulic flume in the Water Resources Laboratory at Concordia University. The flume was used for experiments of siphon flow in this study. .... 30

Figure 3-3 The honeycomb plate consisting of a large number of pipe cells, resembling the one used in this study. (<https://www.pinterest.ca/pin/443112050841637716/>) ..... 31

Figure 3-4 Photo of the laboratory model siphon spillway used in this study..... 32

Figure 3-5 Setup of siphon spillway experiments. (a) design of the crest, crown and entrance of the siphon; (b) discharge under submerged exit conditions ( $h_2/d$  well above unity)..... 33

Figure 3-6 Photo of a typical tailgate in a flume channel. <https://armfield.co.uk/product/c4-mkii-multi-purpose-teaching-flume/>) ..... 34

Figure 3-7 A point gauge in a flume channel to produce measurements of water level and flow depths. (<https://armfield.co.uk/product/c4-mkii-multi-purpose-teaching-flume/>)..... 35

Figure 3-8 Flow over a V-notch weir: (a) cross-sectional view; (b) a longitudinal section. The total energy head of the approach flow on the weir is the sum of the static head  $H$  and the velocity  $V_0^2/2g$ .  $\theta$  is the notch angle. .... 36

Figure 4-1. Longitudinal section of the siphon spillway showing the siphon in the middle, water reservoir to the left of the siphon, and a rectangular flume channel to the right. .... 43

Figure 4-2. Three sections of the model domain, where the length of the reservoir (water tank) section is  $L_1 = 80$  cm, the length of the siphon is  $L_2 = 77.54$ cm, and the length of the downstream flume section is  $L_3 = 80$  cm..... 51

Figure 4-3. Three-dimensional geometry of the siphon and connecting sections. .... 52

Figure 4-4. Sectional view of finite volume mesh in the centre plane  $z = 0.0625$  m ..... 53

Figure 4-5. Sectional view of finite volume mesh, showing inflation near walls. .... 54

Figure 4-6. 3-D view of finite volume mesh..... 54

Figure 4-7. Geometry of the siphon spillway model domain, and three types of boundaries: 1) inlet; 2) outlet; 3) solid walls. .... 56

Figure 4-8 Vertical profiles of the longitudinal velocity component at the siphon crest section, showing values of  $U_1$  at different elevations above the crest for runs RN2G, RN3G and RN4G.  $U_{max}$  is the maximum value of  $u$  at the section,  $d$  is the throat depth from the crest to the crown at the crest section, and  $d = 5.715$  cm. .... 59

Figure 4-9. Vertical profiles of pressure  $P$  at the siphon crest section, showing values of  $P$  at different elevations above the crest for Runs RN2G, RN3G and RN4G. The numerical values of  $P$  are provided in a data sheet in Appendix A (Table A1)..... 60

Figure 4-10. Vertical profiles of the longitudinal velocity component at the siphon crest section, showing values of  $U_1$  at different elevations above the crest for Runs SK4, RL4 and RN4 (Table 4.3).  $U_{max}$  is the maximum value of  $U$  at the section,  $d$  is the distance from the crest to the crown at the crest section. The numerical values of  $U$  are provided in a data sheet in Appendix A (Table A2). .... 61

Figure 4-11. Vertical profiles of pressure  $P$  at the crest section, showing values of  $P$  at different elevations above the crest for Runs SK4, RL4 and RN4. The numerical values of  $U$  are provided in a data sheet in Appendix A (Table A3). .... 62

Figure 4-12. Distribution of velocity vectors in the centre plane  $z = 0.125$  m for Run RN4. This plane is assumed to be a plane of symmetry..... 63

Figure 4-13. Velocity vectors at the conduit exit in the center plane  $z = 0.125$  m for Run RN4. 64

Figure 4-14. The locations of nine selected vertical lines along which distributions of the longitudinal velocity component are to be plotted..... 65

Figure 4-15 Vertical profiles of the longitudinal velocity component in the crest region, showing values of  $u$  for run RN4 (Table A4) at different elevations above the lower surface of the siphon conduit. The streamwise and lateral coordinates are: (a)  $(x, z) = (1.615, 0.125)$  m, which is the plane of symmetry; (b)  $(x, z) = (1.615, 0.0625)$  m, which is at the middle between the plane of symmetry and the sidewall; (c)  $(x, z) = (1.615, 0.005)$  m, which is near the sidewall. The three locations are labelled as vertical lines 2, 8 and 4 in Figure 4.13..... 66

Figure 4-16. Vertical profiles of the longitudinal velocity component in the crest region, showing values of  $U$  for simulation RN4 (Table A5) at different elevations above the lower surface of the siphon conduit. The streamwise and lateral coordinates are: (a)  $(x, z) = (1.67, 0.125)$  m; (b)  $(x, z) = (1.67, 0.0625)$  m; (c)  $(x, z) = (1.67, 0.005)$  m. The three locations are labelled as vertical lines 1, 7 and 9 in Figure 4.13..... 68

Figure 4-17 Vertical profiles of the longitudinal velocity component in the crest region, showing values of  $U$  for simulation RN4 (Table A6) at different elevations above the lower surface of the siphon conduit. The streamwise and lateral coordinates are: (a)  $(x, z) = (1.73, 0.125)$  m; (b)  $(x, z) = (1.73, 0.0625)$  m; (c)  $(x, z) = (1.73, 0.005)$  m. The three locations are labelled as vertical lines 3, 6 and 5 in Figure 4.13..... 69

Figure 4-18. Vertical profiles of the longitudinal velocity  $U$  at the crest: (a) potential flow solution from Dressler (1978); (b) numerical solution from Run RN4 (Table A8), in comparison to the potential flow solution. .... 71

Figure 4-19. Vertical distributions of pressure from the siphon crest to the crown in the centre-line at  $x = 1.644$  m and  $z = 0.125$  m, for RN4 (Table A7). .... 72

Figure 4-20. Vertical distributions of pressure for simulation RN4 in the centre-plane  $z = 0.125$  m. The longitudinal coordinate is: (a)  $x = 1.63$  m; (b)  $x = 1.64$  m; (c)  $x = 1.66$  m. The siphon crest and crown are located at  $x = 1.644$  m. .... 74

Figure 4-21. Vertical distributions of pressure for simulation RN4 in the centreline plane  $z = 0.06$  m. The longitudinal coordinate is: (a)  $x = 1.63$  m; (b)  $x = 1.644$  m; (c)  $x = 1.66$  m. The siphon crest and crown are located at  $x = 1.644$  m. .... 75

Figure 4-22. Vertical distributions of pressure for simulation RN4 in the centreline plane  $z = 0.005$  m. The longitudinal coordinate is: (a)  $x = 1.63$  m; (b)  $x = 1.644$  m; (c)  $x = 1.66$  m. The siphon crest and crown are located at  $x = 1.644$  m. .... 77

Figure 4-23. Variation of the discharge coefficient with normalized head ..... 78

Figure 5-1. Eddie energy transfer. (Richardson, 1922) ..... 82

Figure 5-2. Empirical results for spectra (Pope, 2000), where  $\kappa_1$  is the wavenumber (in  $m^{-1}$ ), and  $E_{11}$  is the energy spectrum (in  $kg\ m^2\ s^{-2}$ )...... 84

Figure 5-3. Boundary-layer flow showing the point of separation  $S$  (Schlichting, 2000)...... 85

Figure 5-4 Selected cross sections: (a) view in the  $xy$  plane; (b) 3-D view..... 87

Figure 5-5. A longitudinal section at  $z = 0.125$  m (the plane of symmetry), showing contours of the magnitude of mean flow velocity,  $\sqrt{U^2 + V^2 + W^2}$  (in m/s), for Run RN4 (Table 4.1). The largest magnitude occurred near the crest. .... 88

Figure 5-6. A longitudinal section at  $z = 0.0625$  m (the middle between the plane of symmetry at  $z = 0.125$  m and the sidewall  $z = 0$ ), showing contours of the magnitude of mean flow velocity,  $\sqrt{U^2 + V^2 + W^2}$  (in m/s), for Run RN4 (Table 4.1). The largest magnitude occurred near the crest. .... 89

Figure 5-7. Flow velocity distributions at cross-section P-C (Figure 5.4): (a) contours of the 3-D flow velocity's magnitude (Equation 5.15); (b) vectors of the 2-D secondary flow velocity (Equation 5.16). The left edges of the panels are the plane of symmetry, and the right edge is the sidewall. .... 91

Figure 5-8. Flow velocity distributions at cross-section P-00 (Figure 5.4). Other remarks are the same as in Figure 5.7. .... 92

Figure 5-9. Flow velocity distributions at cross-section P-1 (Figure 5.4). Other remarks are the same as in Figure 5.7. .... 93

Figure 5-10. Flow velocity distributions at cross-section P-2 (Figure 5.4). Other remarks are the same as in Figure 5.7. .... 95

Figure 5-11. Flow velocity distributions at cross-section P-7 (Figure 5.4). Other remarks are the same as in Figure 5.7. .... 96

Figure 5-12. Flow velocity distributions at cross-section P-12 (Figure 5.4). Other remarks are the same as in Figure 5.7. .... 97

Figure 5-13. Flow velocity distributions at cross-section P-13 (Figure 5.4). Other remarks are the same as in Figure 5.7. .... 98

Figure 5-14. Flow velocity distributions at the siphon exit cross-section  $x = 2.28$  m. Other remarks are the same as in Figure 5.7. .... 99

Figure 5-15. Vertical section at  $z = 0.02$  m, showing longitudinal distribution of  $k$ . The model time was  $t = 22.8$  s; the upstream and downstream reservoirs' water levels (Figure 4.1) were  $H_1 = 2.20$  m, and  $H_2 = 0.432$  m, respectively. .... 100

Figure 5-16. Vertical section at  $z = 0.125$  m, showing longitudinal distribution of  $k$ . The model time was  $t = 22.8$  s; the upstream and downstream reservoirs' water levels (Figure 4.1) were  $H_1 = 2.20$  m, and  $H_2 = 0.432$  m, respectively. .... 101

Figure 5-17. Vertical section at  $z = 0.074$  m, showing longitudinal distribution of  $k$ . time was  $t = 22.8$  s; the upstream and downstream reservoirs' water levels (Figure 4.1) were  $H_1 = 2.20$  m, and  $H_2 = 0.432$  m, respectively. .... 101

Figure 5-18. Vertical section at  $z = 0.125$  m, showing longitudinal distribution of  $k$ . The model time was  $t = 13$  s. The upstream and downstream reservoirs' water levels (Figure 4.1) were  $H_1 = 2.16$  m, and  $H_2 = 0.314$  m, respectively. .... 102

Figure 5-19. Vertical section at  $z = 0.125$  m, showing longitudinal distribution of  $k$ . The model time was  $t = 19$  s. The upstream and downstream reservoirs' water levels (Figure 4.1) were  $H_1 = 2.20$  m, and  $H_2 = 0.416$  m, respectively. .... 103

Figure 5-20. Distribution of  $k$  at cross-section P-00 (Figure 5.4). The left edges of the panel is the plane of symmetry, and the right edge is the sidewall. .... 104

Figure 5-21. Distribution of  $k$  at cross-section P-C (Figure 5.4). Other remarks are the same as in Figure 5.20. .... 104

Figure 5-22. Distribution of  $k$  at cross-section P-5 (Figure 5.4). Other remarks are the same as in Figure 5.20. .... 105

Figure 5-23. Distribution of  $k$  at cross-section P-11 (Figure 5.4). Other remarks are the same as in Figure 5.20. .... 106

Figure 5-24. Distribution of  $k$  at cross-section P-13 (Figure 5.4). Other remarks are the same as in Figure 5.20. .... 107

## List of Tables

Table 3-1 Scaling ratios of forces used in physical hydraulic models.....	28
Table 3-2 Hydraulic conditions and discharge coefficient for experiments under submerged exit conditions. The vertical datum is located at the obvert of the exit of the siphon. ....	39
Table 4-1 The grid resolutions and initial conditions for five model runs. the purpose of these runs was to confirm the independence of numerical results on mesh configuration and to evaluate the suitability of turbulence closure models. ....	58
Table 4-2 Hydraulic conditions for numerical simulations and laboratory experiments of siphon flow. ....	79

## Notation

The following symbols have been used in this thesis:

A	Cross-sectional area ( $\text{m}^2$ )
b	Width of siphon conduit (m)
B	Width of the downstream channel of the physical model(m)
$C_d$	Discharge coefficient
$C_\mu$	Empirical closure constant
$C_L$	Energy loss coefficient
$C_{1\varepsilon}, C_{2\varepsilon}$	Empirical closure constants
d	Vertical distance between the siphon spillway crest and crown (m)
$E_{11}$	Energy spectrum ( $\text{kg m}^2 \text{s}^{-2}$ )
Fr	Froude number
g	Acceleration due to gravity ( $\text{m s}^{-2}$ )
$G_b$	Generation of turbulence kinetic energy due to buoyancy
$G_k$	Generation of turbulence kinetic energy due to the mean velocity gradients
h	Head on the spillway (m)
$h_D$	Water head over the Ogee spillway crest (m)
H	Static head on the V-notch weir (m)
$H_d$	Design head physical model (m)
$H_1$	Water level measured at the upstream reservoir ( $Z$ in chapter two) (m)

$H_2$	Water level measured at downstream flume (m)
$H_x$	Spatial derivative of the free surface elevation (m)
$I$	Turbulence intensity
$I_o$	Length scale of the larger eddies
$k$	Specific turbulence kinetic energy ( $m^2 s^{-2}$ )
$kN$	Local shallowness parameter
$L$	Length of the numerical model from the inlet of the upstream reservoir to the outlet of the downstream flume (m)
$L_p$	Prototype length (m)
$L_m$	Length in the laboratory model (m)
$N$	Water depth in open channel (m)
$P$	Siphon front wall height (m)
$Q$	Discharge ( $m^3 s^{-1}$ )
$R_i$	Curvature radius (m)
$R_o$	Crown radius (m)
$Re$	Reynolds number
$R_\lambda$	Taylor-scale Reynolds number
$Re_\eta$	Kolmogorov Reynolds number
$S_{ij}$	Mean strain-rate tensor ( $s^{-1}$ )
$S_k, S_\varepsilon$	Source terms

$U$	Time-averaged velocity vector ( $\text{m s}^{-1}$ )
$U_i$	Mean velocity component ( $\text{m s}^{-1}$ )
$U_{\max}$	Maximum velocity ( $\text{m s}^{-1}$ )
$u$	Longitudinal flow velocity ( $\text{m s}^{-1}$ )
$u_x$	Spatial derivatives of the horizontal velocity component ( $\text{m s}^{-1}$ )
$u_t$	Temporal derivatives of the horizontal velocity ( $\text{m s}^{-1}$ )
$(u_1, u_2, u_3)$	Velocity components in the Cartesian coordinates $(x_1, x_2, x_3)$ ( $\text{m s}^{-1}$ )
$(u'_1, u'_2, u'_3)$	Fluctuating velocity components ( $\text{m s}^{-1}$ )
$(U_1, U_2, U_3)$	Time-averaged velocities ( $\text{m s}^{-1}$ )
$(u', v', w')$	Fluctuating velocity components in the x, y, and z direction ( $\text{m s}^{-1}$ )
$v$	Vertical flow velocity ( $\text{m s}^{-1}$ )
$V_o$	Average velocity of the V-notch weir ( $\text{m s}^{-1}$ )
$\vec{V}_p$	Magnitude of the primary flow velocity vector ( $\text{m s}^{-1}$ )
$\vec{V}_s$	Secondary flow velocity vector of ( $\text{m s}^{-1}$ )
$v_w$	Velocity at any point above the weir ( $\text{m s}^{-1}$ )
$w$	Lateral flow velocity ( $\text{m s}^{-1}$ )
$Wb$	Weber's Number
$(x, y, z)$	Coordinates in the longitudinal, vertical, and lateral directions
$(x_1, x_2, x_3)$	Equivalent to $(x, y, z)$

$Y$	Water depth at any point above the siphon crest (m)
$Y_m$	Contribution of the fluctuating dilatation in compressible turbulence to the overall dissipation rate
$\delta p$	Relative error in percentage
$\alpha_a$	Air volume of fraction in the computational cell
$\alpha_w$	Water volume of fraction in the computational cell
$\delta_{ij}$	Kronecker symbol
$\nu_T$	Kinematic eddy viscosity ( $\text{m}^2 \text{s}^{-1}$ )
$\varepsilon$	Dissipation rate of turbulent kinetic energy ( $\text{m}^2 \text{s}^{-3}$ )
$\lambda$	Length ratio of corresponding side of prototype and laboratory models
$\mu_{eff}$	Effective viscosity ( $\text{m}^2 \text{s}^{-1}$ )
$\eta$	Length scale (m)
$u_\eta$	Velocity scale ( $\text{m s}^{-1}$ )
$\tau_{ij}$	Specific Reynolds stress tensor ( $\text{m}^2 \text{s}^{-2}$ )
$\tau_w$	Wall shear stress ( $\text{m}^2 \text{s}^{-2}$ )
$\kappa_1$	Wavenumber ( $\text{m}^{-1}$ )

# Chapter One

## 1. Introduction

### 1.1. Background

Flow control is one of the main design aspects in hydraulic engineering practice. Flow control facilities are important and necessary to handle floods and protect the reservoir (dam). Reservoirs are structures constructed to capture water and achieve a good management of water resources. In some cases, hydraulic structures regulate the flow in the systems and pass water to canals or pipelines. Outlet works are devices used to drain water from a reservoir as needed to serve specific purposes like irrigation, flood control, and power generation benefit from high storage level. In general, the water level in the reservoir will be kept at a high level without exceeding the safety limit. Also, it is a good practice to keep the reservoir water level low before floods occur in flood season (Linsley and Franzini, 1971). Depending on the site conditions and the hydraulic particularities, the outlet work structures vary in different designs (Figure 1.1). Spillways are most common outlet structures that are used in many dams, as well as in drainage systems.

The purpose of a spillway is to evacuate excess water, which cannot be stored in the reservoir, or to bypass the overflow. Gated spillways have gates that control the flow rate from the system. In contrast, ungated spillways are not regulated by a gating mechanism; when the water level exceeds the crest of the spillway, the flow automatically goes out of the reservoir. The rate of discharge of an uncontrolled spillway can only be regulated by the amount of water within the reservoir.

### 1.2. Classification of spillways

Spillways are classified according to their features, such as the shape and the suitability of site (Coleman et al., 2004).

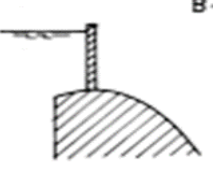
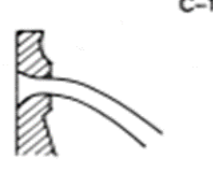
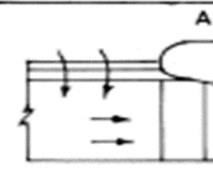
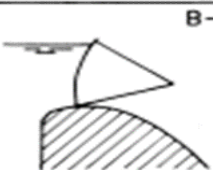
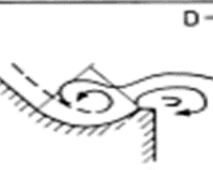
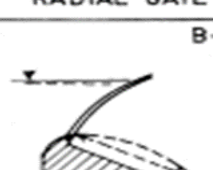
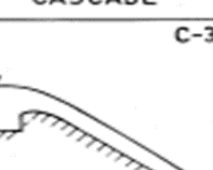
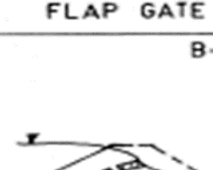
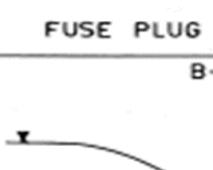
A	B	C	D
INLET	REGULATION	CHANNEL	OUTLET
 <p>A-1 OVERFLOW</p>	 <p>B-1 SLUICE GATE</p>	 <p>C-1 FREE FALL</p>	 <p>D-1 STILLING BASIN</p>
 <p>A-2 COLLECTING CHANNEL</p>	 <p>B-2 RADIAL GATE</p>	 <p>C-2 CASCADE</p>	 <p>D-2 ROLLER BUCKET</p>
 <p>A-3 SHAFT SPILLWAY</p>	 <p>B-3 FLAP GATE</p>	 <p>C-3 SPILLWAY CHUTE</p>	 <p>D-3 SKY JUMP</p>
 <p>A-4 SIPHON</p>	 <p>B-4 FUSE PLUG</p>	 <p>C-4 FREE FLOW TUNNEL</p>	 <p>D-4 PLUNGE POOL</p>
 <p>A-5 ORIFICE</p>	 <p>B-5 UN REGULATED</p>	 <p>C-5 PRESSURE TUNNEL</p>	

Figure 1-1. Classification of the outlet-works, (A-1 to A-5, and C-1 to C-5) shown different types of spillways (from Khatsuria, 2004)

Five main types of uncontrolled spillways are described below:

1. Shaft Spillway (Figure 1.2a and 1.2.b): This type of spillway is used in cases where it is not possible to use an overflow spillway. These types of spillways consist of a horizontal crest at the upstream and a vertical shaft in a horizontal channel downstream of the dam.

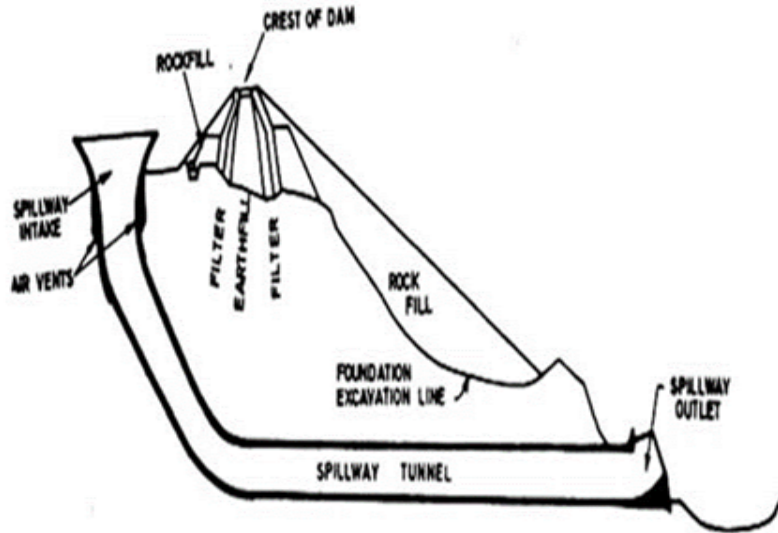


Figure 1-2. Trough spillway (<http://hydropedia.blogspot.ca/2014/03/spillway.html>, accessed on June 1, 2017) and photo of Glory Hole Spillway at Lake Berryessa, California, U.S. (<https://www.usbr.gov/newsroom/stories/detail.cfm?RecordID=58763>)

2. Free overflow spillway (Figure 1.3): This is one of the simplest types. It consists of a low weir with a thin crest leading to a nearly vertical downstream face. Uses of the free

overflow spillway include low earth dams, low gravity dams, and low thin arch dams. Free overflow spillways are not appropriate for high dams.

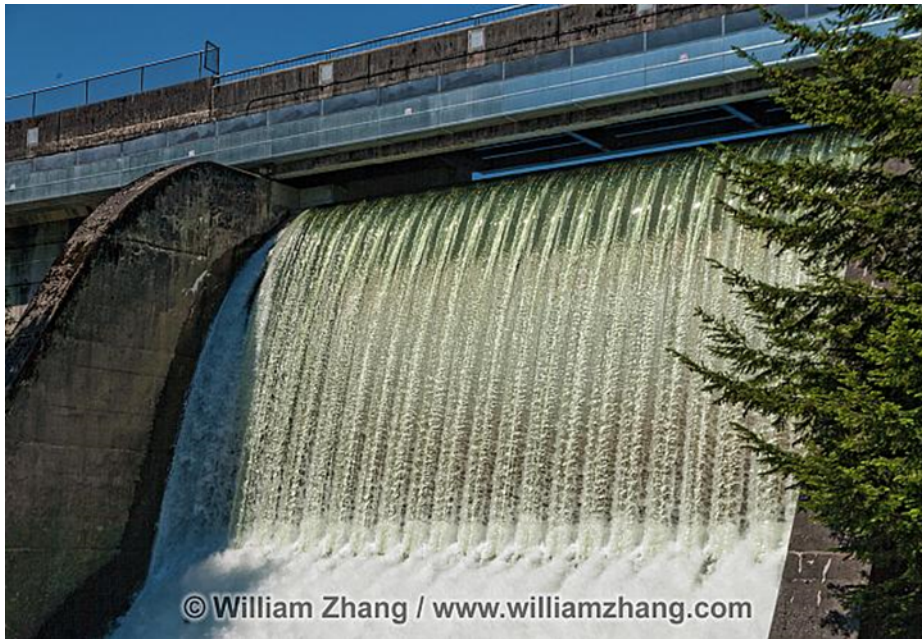
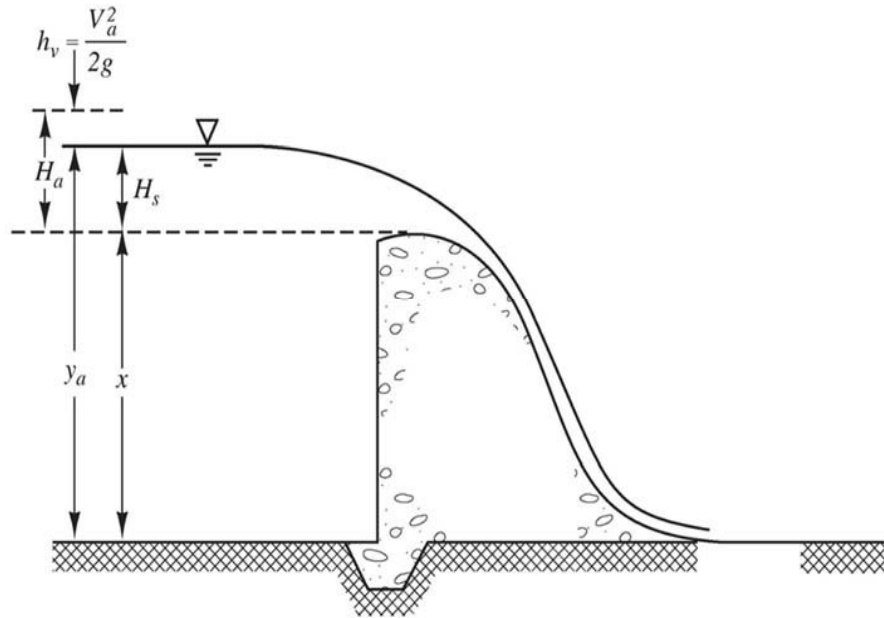


Figure 1-3. Shape of overflow spillway (from Houghtalen et al., 2017) and photo of Cleveland dam overflow spillway in North Vancouver, B.C., Canada. (<http://www.williamzhang.com/>)

3. The ogee spillway (Figure 1.4): This is a modified version of an overflow spillway. Uses of the ogee spillways include high gravity and arch dams. Water falls quietly from the crest to follow the profile of the spillway.

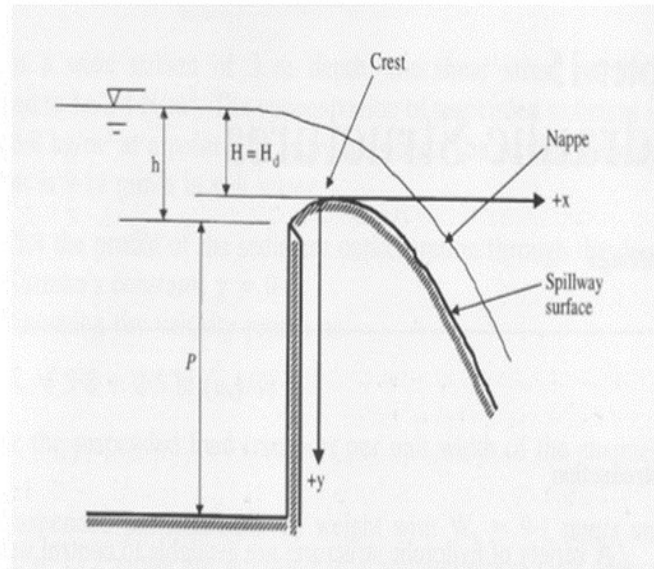


Figure 1-4. Longitudinal profile of ogee spillway (from Nalluri and Featherstone, 2009), and photo of Rend Lake Spillway, Illinois, U.S. (<https://www.pinterest.ca/pin/68609594297759152/>)

4. Side channel spillway (Figure 1.5): Regarding this type of spillway, overflow water is carried away by a side channel, once the water level rises above the crest. This is used when a valley exists at the side of the reservoir.

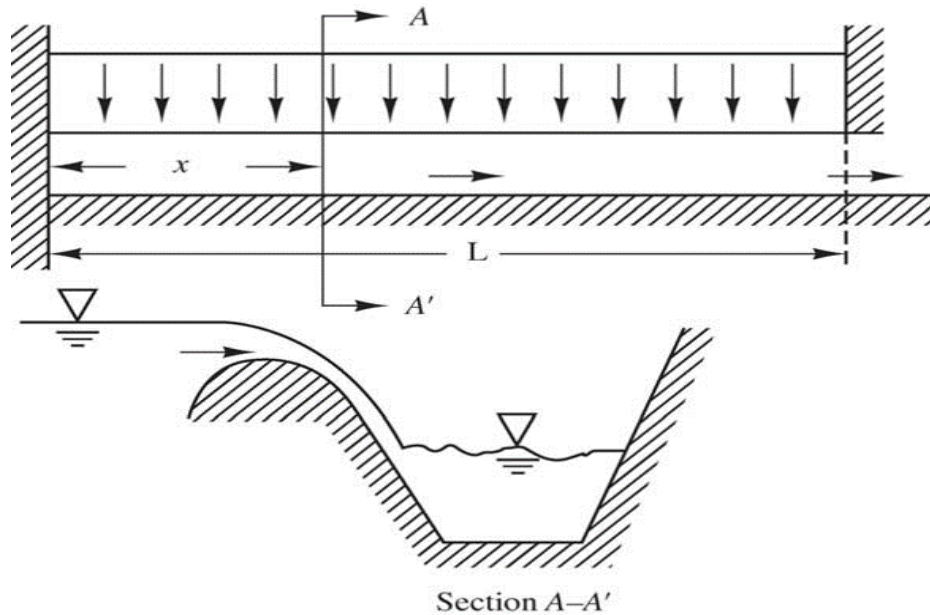


Figure 1-5. Side channel spillway (Houghtalen et al., 2017) and photo of Revelstoke side channel spillway, Revelstoke, B.C., Canada (<https://www.pinterest.ca/pin/54817320442348907>)

5. Siphon spillway: This type of spillway has frequently been used for open-channel water level control. Siphon is a different reservoir spillway, compared to other types of spillways. When siphonic action happens, siphon discharges a large amount of water quickly until the upstream water level falling below the siphon inlet level.

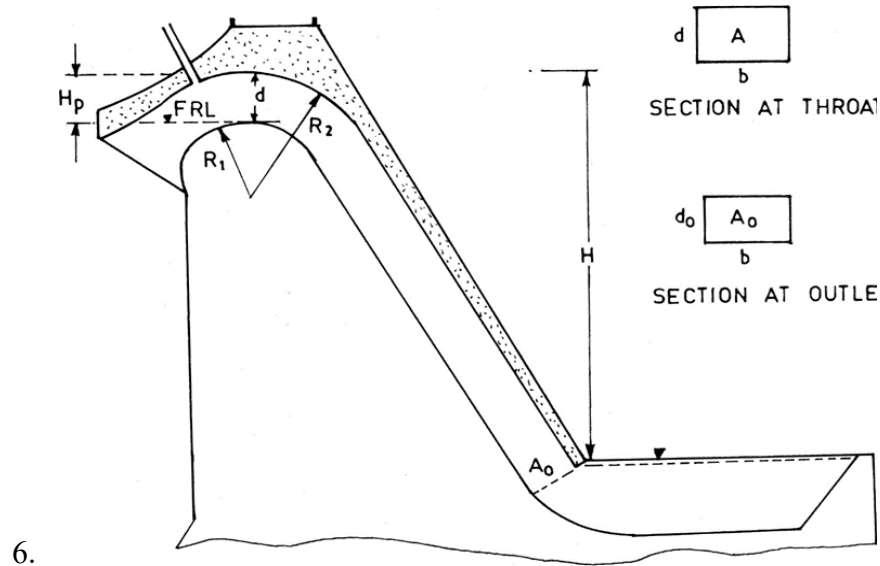


Figure 1-6. Typical siphon (Michael D. Meyer, 2005) and photo of Brent Reservoir siphon spillway, London, UK (<https://canalrivertrust.org.uk/news-and-views/media-centre/filming-and-photography/our-filming-and-photography-locations/brent-reservoir-welsh-harp>)

Siphon consists of a closed U-shaped conduit system. Its cross-section can be rectangular or circular (Figure 1.6). As the water level in the reservoir rises above the crest, the incoming flow is discharged like the flow over a weir (free flow). Siphon priming occurs when the water level rises and the air from the downstream cannot access the conduit.

### 1.3. Cavitation potential

It is well known that in static conditions, if the water pressure drops below the water vapour pressure, the water will undergo a phase transition from the liquid phase to vapor. In a siphon spillway, when the water flow over the crest, the velocity becomes high, which induce low pressure. The pressure on the crest section must be managed to ensure that it does not become too strongly negative. When the pressure becomes largely negative pressure, it can cause cavitation, the destabilization of the siphon and maybe failure. The negative pressure risk and the cavitation can be estimated in terms of the maximum discharge capacity of the siphon. When flow conditions cause the water pressure to be below vapour pressure, cavitation occurs in this region. When vapour bubbles formed in a low-pressure region migrate to a higher-pressure region, they collapse explosively, with a loud noise (Figure 1.7). Thus, cavitation is a serious problem that can destroy the hydraulic structure. This research has investigated the possibility of cavitation and minimum pressure values.

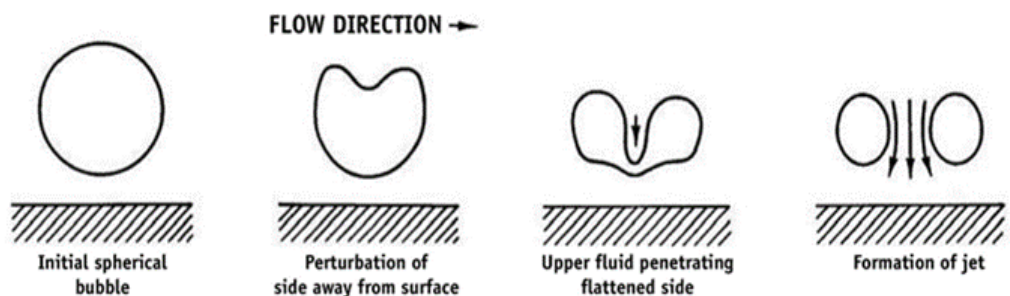


Figure 1-7. Cavitation bubble collapse process (Machado, 2009)

### 1.4. Important issues

The siphon spillway has great hydraulic features. Large discharge capacity is one such advantage. Also, there are no moving components, and it carries an almost constant flowrate. Analysis of the

mean characteristics of flow in a siphon is an important engineering issue. The curved boundaries at the crest create streamlines with vertical curvature. This curvature can significantly affect the flow characteristics. A review of the literature indicates that several studies have given information about siphons, including simplification and characterisation of siphons and their functions. Head (1971) studied an air-regulated siphon and characterised its design and performance. He stated that the flow could run through the siphon in two different states. Either the flow is free with a free surface or the flow is under pressure. In the free surface condition, the siphon acts as a weir. In contrast, in the under-pressure condition, it acts as an orifice. Subsequently, Head (1975) experimentally studied a low-head-regulated siphon. Savage and Johnson (2001) studied the flow over an Ogee spillway experimentally and numerically. The main purpose of Savage and Johnson's (2001) study was to compare their experimental and numerical results with the existing results from the U.S. Bureau of Reclamation's (USBR, 1977) and the U.S. Army Corps of Engineers' (USACE, 1990) design reports. Babaeyan-Koopaei et al. (2002) presented a case study on the hydraulic performance of the Brent Reservoir siphon spillway. More recently, a few numerical studies have also been reported. For instance, Tadayon and Ramamurthy (2013) used the RNG  $k-\epsilon$  model to obtain the coefficient of discharge for a siphon spillway. They validated their model predictions using results from experiments of flow in a physical model of the siphon spillway.

However, the mechanisms of flow through the siphon have often been oversimplified. For instant, all the previous studies dealt with the flow through the siphon as free flow condition. Siphon discharges under submerged conditions have not been thoroughly investigated in the past. Furthermore, they did not address the possibility of cavitation.

With rapid advances in computational hydraulics to help solve the equations governing fluid flow, engineers now must decide which methods to use to evaluate existing and proposed spillway designs. Today there are several commercially available software tools for modeling and simulation of multi-phase flows. However, efficient modeling still requires a great level of theoretical knowledge and experience within specific disciplines. All the information that will be provided will assist the engineers to design efficient siphons and avoid cavitation.

### **1.5. Research objectives**

The aim of this study is to extend the previous work on siphon spillways and to understand the flow characteristics of the siphon spillway experimentally and numerically in order to:

- Analyse the features of curvilinear flow at the crest section, in particular the velocity distribution and the magnitude and location of the maximum velocity between the lower and upper boundaries on the crest.
- Expand the study involving the velocity data and wall pressure data to indirectly estimate the pressure distributions in the crest region.
- Determine the discharge coefficients for the case of submerged flow.
- Construct three-dimensional (3-D) computational model of flow through the siphon to obtain the pressure distribution and velocity distribution.
- Demonstrate the validity of the numerical model by using the experimental results.
- Determine the turbulent kinetic energy distribution and the intensity of the secondary flow.
- Lastly, study cavitation phenomena.

### **1.6. Research contributions**

This research has made the following contributions:

- Help to acquire a better understanding of the curvilinear flow characteristics in the region of rounded crest.
- Provide a CFD model to analyze water flow in similar hydraulic structures.
- Use pressure data and allow the possibility to validate the cavitation potential in the spillway.

## Chapter Two

### 2. Literature Review

#### 2.1. Introduction

A review of the literature of the studies on spillways in general and siphon spillways in particular, is presented in this chapter. It details three different but complementary techniques. These techniques are: field observations, laboratory measurements, and mathematical analysis.

Siphon spillways have been investigated and have received an interest in experimental studies, analytical analysis.

It is a good practice to keep the reservoir water level low before floods occur (Linsley and Franzini 1971). There are several types of spillways used on dams, including an overflow spillway, a side-channel spillway, and a siphon spillway (Houghtalen et al. 2017). Fundamentals of their hydraulic designs and efficiencies can be found in textbooks.

Previously, extensive investigations of the problem of flow over an overflow spillway have been reported in the literature (Cassidy 1965, 1970, 1975; Castro-Orgaz 2008; Hager 1987; Peltier et al. 2018; Savage and Johnson 2001; USBR 1987; Vermeyen 1991; Vermeyen et al. 1992), leading to an impressive progress in understanding the ideal crest profiles, discharge characteristics, flow velocity, and pressure distribution.

Regarding siphon spillways, the reliability of action, simplicity and permanence of construction, automatic water-level regulation, less maintenance and operation expenses, and a large discharge capacity are the parameters that make the siphon spillways very an efficient hydraulic structure. At the beginning, water flows through the siphon due to the push of atmospheric pressure on the free surface at the reservoir. When the upstream water level rises

higher than the siphon entrance and the siphon exit is submerged, the siphonic action starts (Head, 1971).

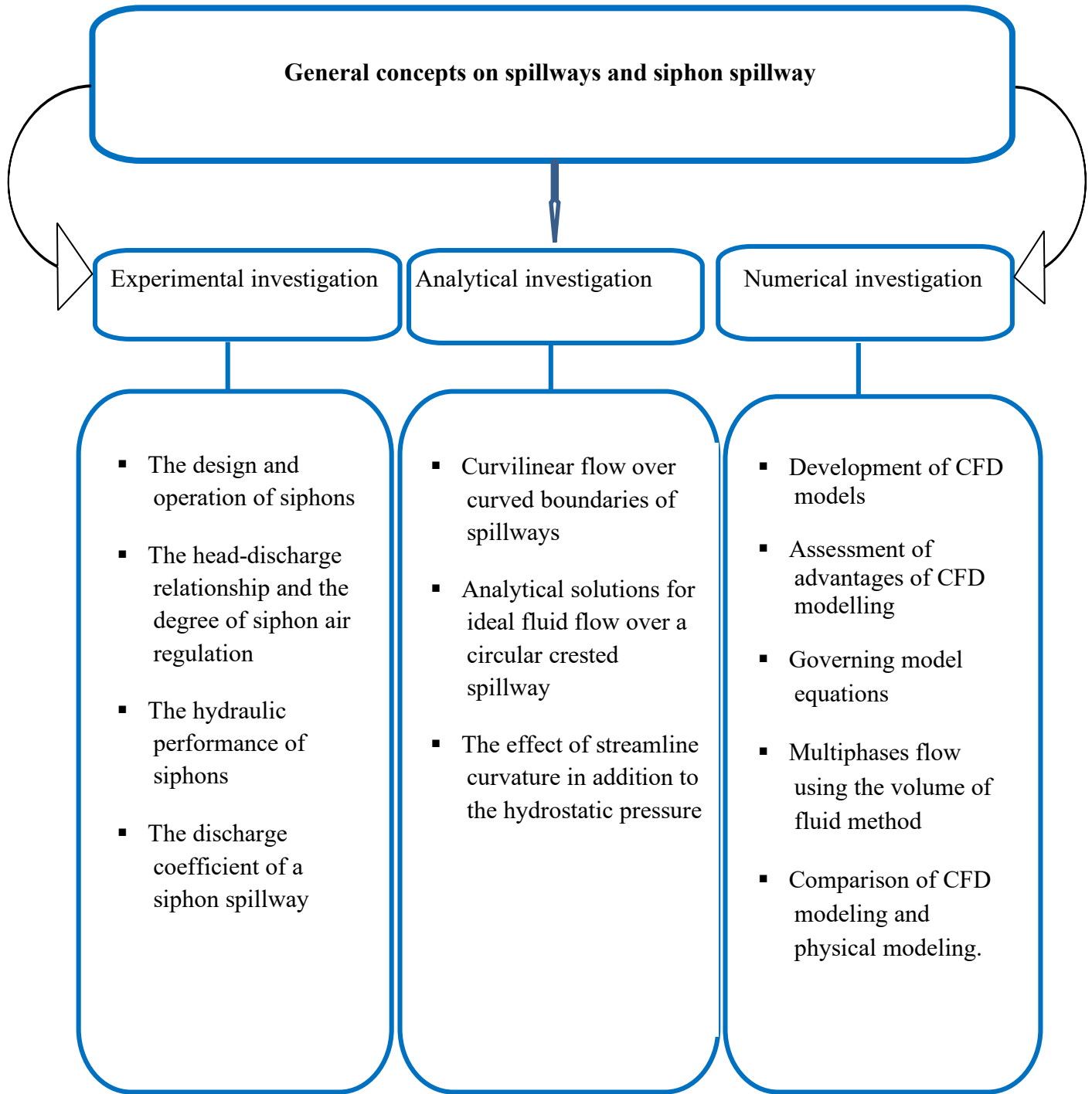


Figure 2-1. General concepts on spillways and siphon

## 2.2. Experimental investigation

Previously, several researchers have conducted laboratory studies of the characteristics of flow through a siphon spillway. Head (1971) investigated one of the conventional siphons. This type of siphon is called an air-regulated siphon. Head (1971) studied the shape and design of this type of siphon and also explained in detail its operation. The study assessed the ability of the siphon in controlling the flood flow. Generally speaking, it can adjust automatically and pass smoothly the overflow water that is above the design maximum and keep the water level upstream of the siphon almost constant. Head (1971) identified five stages of operation in a low-head, air-regulated siphon system. These stages are weiring flow, deflected nappe, depressed nappe, air partialised flow and blackwater flow (Figure 2.2).

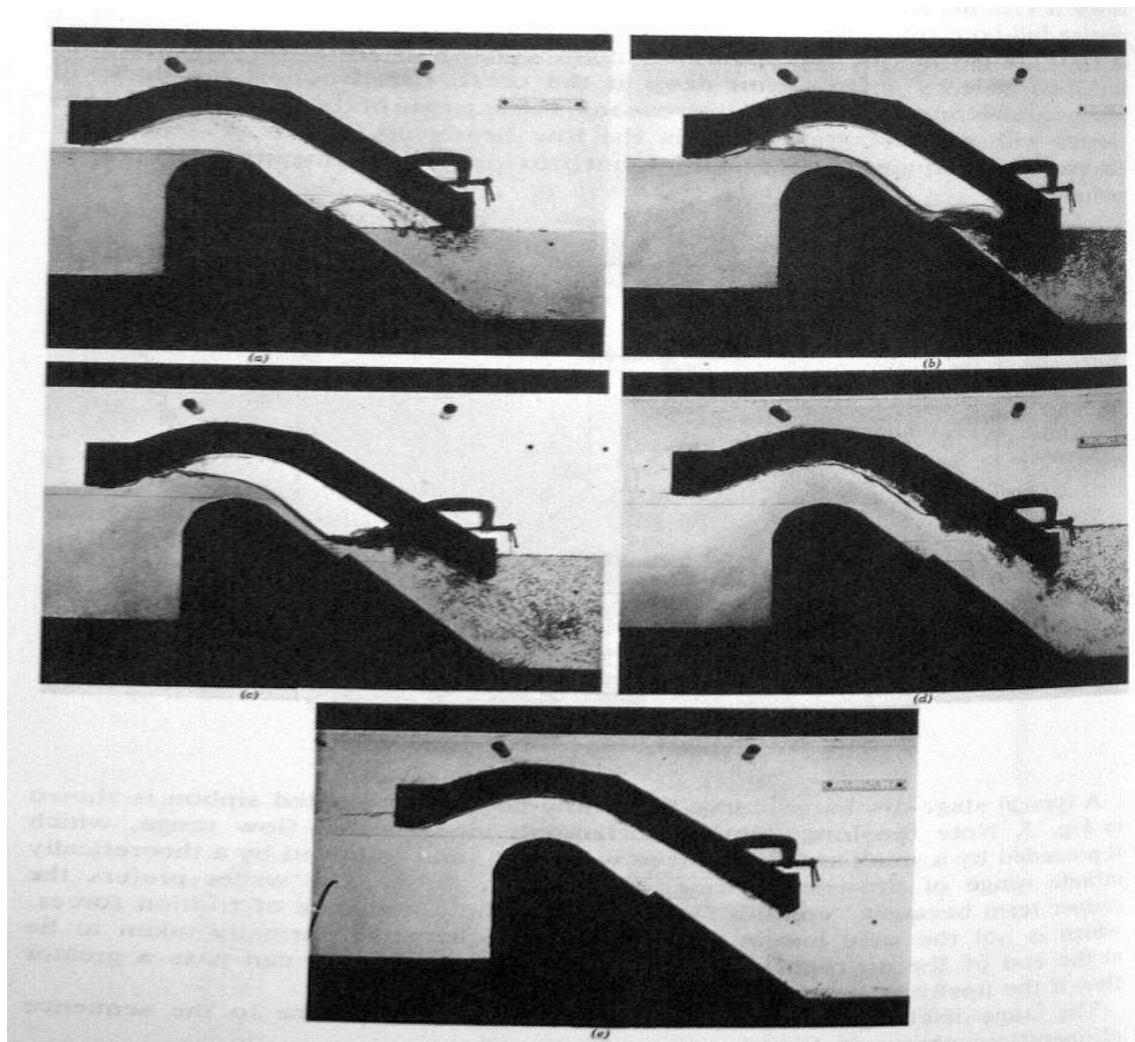


Figure 2-2. Five flow stages (Head 1971)

As the water level in the reservoir rises above certain normal level, the water is discharged in a way similar to the free flow over a weir. Siphonic action will begin when the outlet is obstructed either by tailwater submergence or by the use of a jet deflector to prevent downstream air from accessing the siphon conduit. Initially, during priming, air and water enter the conduit from the entrance (air-regulated or aerated flow). With further rises of water level, the conduit operates as a closed conduit, and no air entrainment is included in this flow, which is termed blackwater flow. Head (1971) discovered the stage between the blackwater siphon and the air-regulated siphon. At that stage, air-regulated siphon automatically adjusts the flow discharge to maintain the upstream water level relatively constant. This laboratory investigation is of great value as a design guide. However, it has limitations because the mechanism and flow features have not been predicted, and for this reason, further researches are required.

In a further study, Head (1975) conducted experiments of a regulated siphon. He found that the action of siphon depends on the continual evacuation of air at the outlet and the intake of air at the inlet. Therefore, the crest level, the shape and the level of siphon inlet, the level of downstream lip, and the shape and the position of the deflector are important features that require special care to be taken into account in the design of the siphon. These studies have made it very clear about the siphon work mechanism and the considerations required when designing the siphon. However, the studies did not address the question of the flow itself and did not study the effect of boundary conditions on the flow. They did not explore the distribution of the velocity nor the distribution of pressure and did not address some of the phenomena associated with hydraulic flow, such as cavitation. This study significantly extends Head's (1971, 1975) studies and investigates the features of the flow passing the siphon crest, with much more details about the velocity and pressure.

Through their 24-year study, Ervine and Oliver (1980) described the performance of air-regulated siphon spillways. The main aim of their long-term study was to investigate the head-discharge relationship and to determine the degree of siphons' air regulation. The study was conducted using a group of prototype siphons. Physical models of siphon at scale 1:5 and 1:10 were used in Ervine and Oliver (1980) and the result were compared with prototype models' results as shown in Figure 2.3.

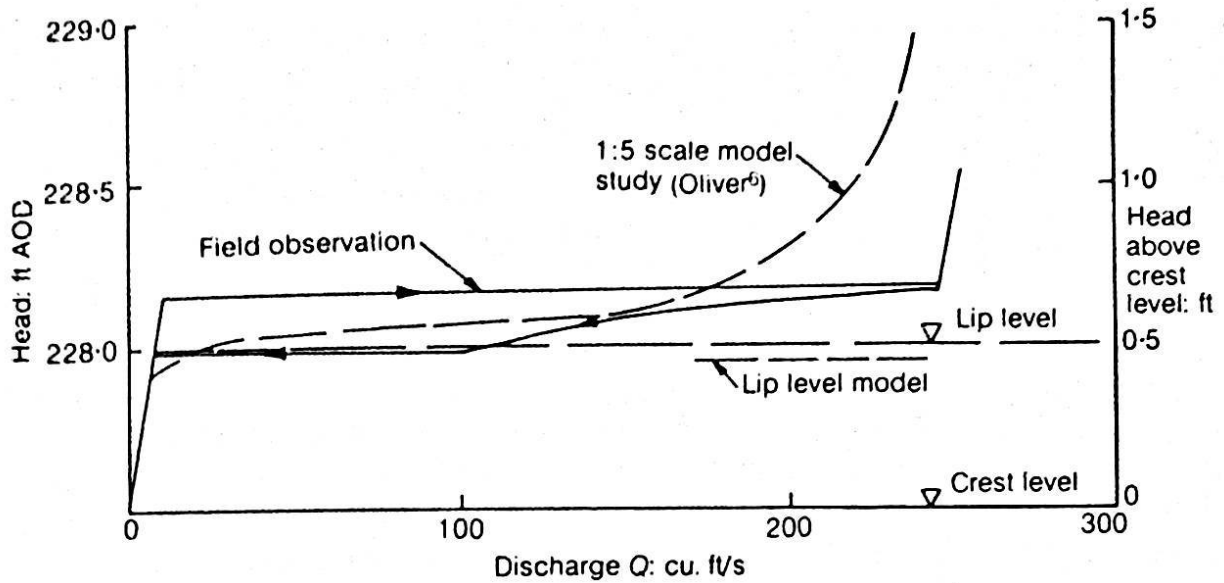


Figure 2-3. Comparison of head-discharge curves for full scale model and 1:5 scale for the siphon (Ervin and Oliver 1980)

It was concluded that a siphon spillway can pass extremely high discharge at almost constant water level in the reservoir. Also, the study showed that the height of the inlet lip increases the degree of air regulation while wind factor slightly increases upstream water level. The authors pointed out some limitations in their work, which cause misleading prediction of the prototype performance. These limitations are due to: the vortices at the inlet cause a steepening that show in the head-discharge curve of the physical model and does not appear on the same curve of the full-scale siphon. The scaled physical model gave lower discharge coefficients than the full-scale model. This is another study that deals with only the flow stages and the effect of siphon's geometry on the flow, while the flow elements such as velocity and pressure were not specifically analysed. This research has covered the deficiency and investigated the flow characteristics in the siphon crest region in details.

Babaeyan-Koopaei et al. (2002) presented a case study on the hydraulic performance of the Brent Reservoir siphon spillway. They discussed in detail the problem of the hydraulic performance of the Brent Reservoir siphons. A physical model was used to investigate the hydraulic performance of siphons. The model was constructed using a 1:10 scale; it provided model dimensions that satisfy the Froude number scaling law. The experimental study was carried out in two parts. In the first part, the existing geometry was examined. The results showed that the

siphon suddenly primed at discharges between 2.5 and 3 m<sup>3</sup>/s, with a sudden sweep out of air pockets. This is simply because the bell mouths are already submerged. Therefore, the air regulation should be improved, and the air inlet should possibly be redesigned. In the second part of the experiments, various options were studied to improve the air inlet and establish stable siphon condition over a range of discharges. It was found that cutting an air slot into the spillway hood at an appropriate level will provide the most stable conditions. This solution provides the best air-regulated stability and improves the siphon spillway capacity. The importance of Babaeyan-Koopaei et al.'s (2002) study lies in being a practical example of the hydraulic performance of siphon spillway.

### 2.3. Analytical investigation

Curvilinear flow over curved boundaries of spillways have been investigated and have received an interest in analytical analysis. Cassidy (1965) reported an analytic solution for an ideal fluid flow over a circular crested spillway (Figure 2.4). The purpose of the solution was to determine the discharge coefficients, free-surface profiles and pressure distributions resulting from irrational flow.

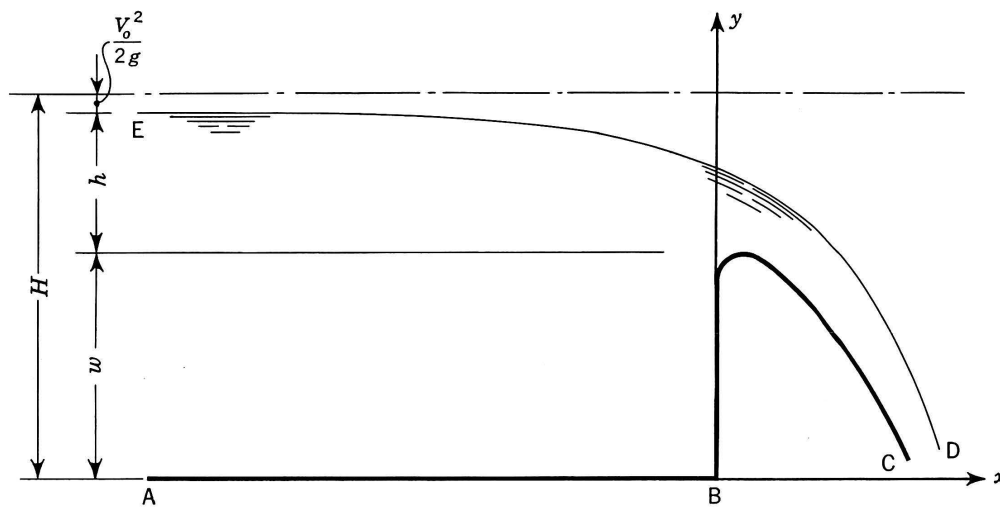


Figure 2-4. Flow over spillway in physical plane (Cassidy 1965)

Assuming that the viscosity, surface energy, and solid surface roughness are negligible, the study expressed the flow characteristics as:

$$f = f\left(\frac{y}{h_D}, \frac{x}{h_D}, \frac{w}{h_D}, \frac{h}{h_D}\right) \quad (2.1)$$

where  $y$  is the vertical coordinate,  $x$  is the horizontal coordinate,  $h$  is the head on the spillway,  $h_D$  is the water depth over spillway crest, and  $w$  is the spillway height. As results from the study, water surface profile, discharge coefficient and the pressure distribution were computed numerically and investigated experimentally (Figure 2.5).

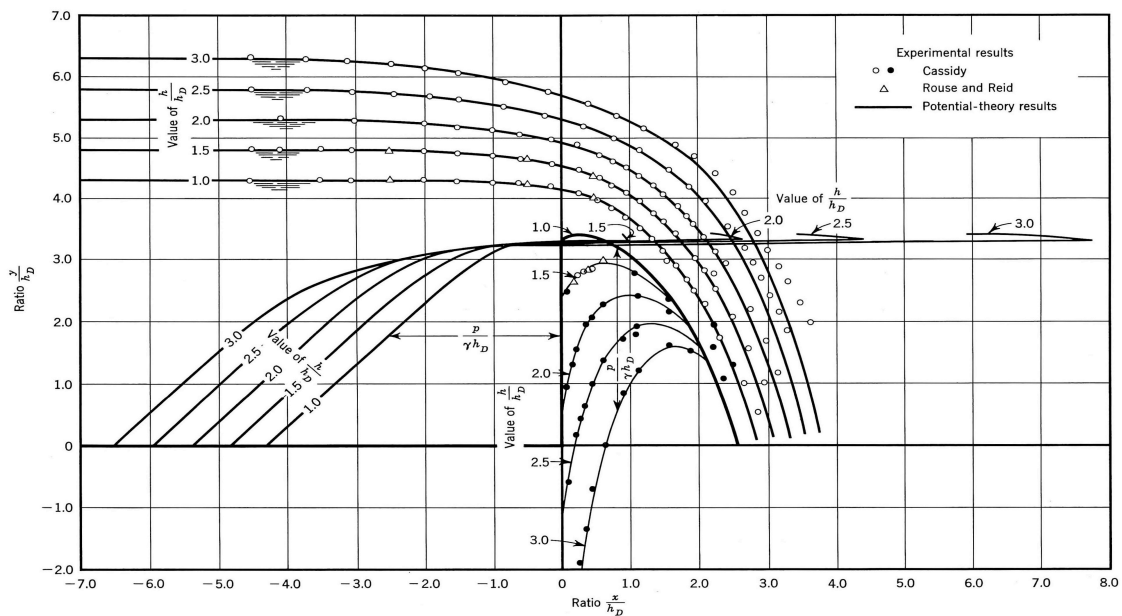


Figure 2-5. Free-surface profiles and pressure distributions for standard spillway (Cassidy 1965)

No solutions were available for use before the study of Cassidy (1965). Thus, the study was considered an important study. However, the study has some limitations:

- The solution is valid only for flow with a high Reynolds number and over smooth boundaries because of the assumption that the effects of viscosity and solid surface roughness are negligible.
- Because the way to determine the location of water surface was by trial-and-error procedures, an error is highly expected.
- Another disadvantage relates to the practicability of the solution, which requires a large computer storage capacity.

Posteriorly, Cassidy (1970) presented a mathematical method for analysing the flow over a standard-shaped spillway. The purpose of the study was to design ungated standard shaped spillway to operate at water head higher than the design head minimum pressure that can be less than atmospheric pressure. Based on the assumption that the influence of both the Reynolds number and the Froude number could be neglected, the discharge coefficient for an overflow ungated spillway was determined as:

$$\frac{Q}{Lh^{3/2}} = \phi\left(\frac{h_D}{H}, \frac{h}{h_D}\right) \quad (2.2)$$

where  $H$  is the height of spillway,  $h_D$  is the design head for siphon, and  $h$  is the head on the spillway (Figure 2.6).

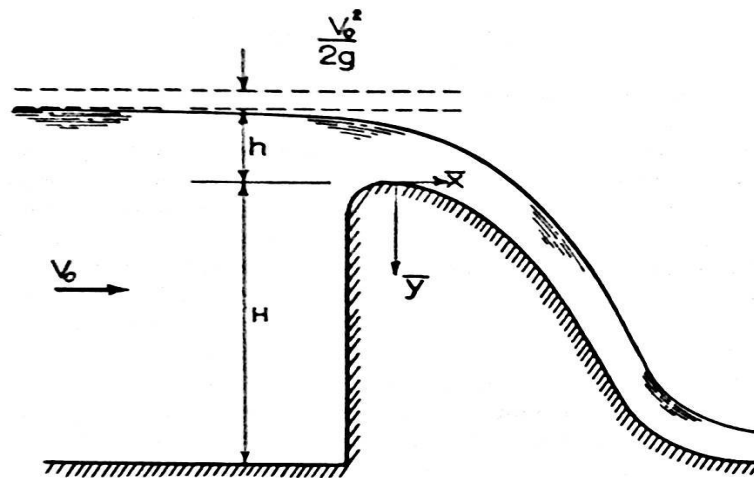


Figure 2-6. Flow over spillway (Cassidy 1970)

The minimum crest pressure was also expressed as a function of the spillway design head and the spillway height:

$$\frac{P_{min}}{\gamma h} = f\left(\frac{h_D}{H}, \frac{h}{h_D}\right) \quad (2.3)$$

Cassidy (1970) found that spillway crest can pass the maximum flow rate for high head operation with the minimum pressure occurring on the crest. This minimum value of the pressure can be the vapor pressure.

Three physical models were constructed and tested in order to verify Equation (2.1) and Equation (2.2). Experimental data of discharge coefficient and minimum pressure of the flow over the spillway crest were presented in dimensionless form (Figure 2.7).

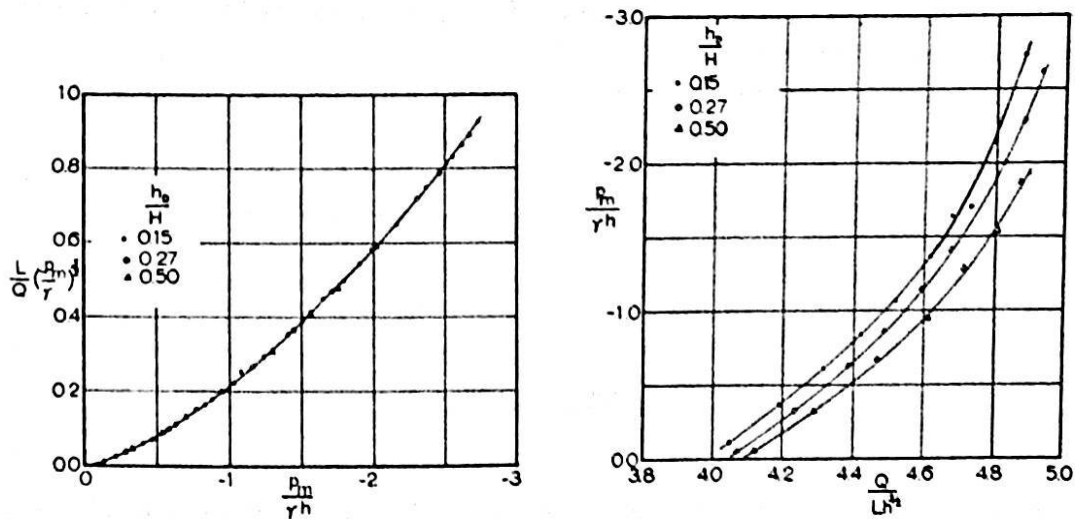


Figure 2-7. Discharge-minimum pressure characteristics of standard spillway (Cassidy 1970)

Although the study of Cassidy (1970) has developed important rules that must be taken into account in the design of spillways, there are some limitations and disadvantages due to

- the assumption of a negligible influence of the Reynolds number,
- the use of a calibrated elbow meter for measurements of flow discharge over the crest that gave inaccurate result.

Considering flows over a range of Reynolds numbers, this study accurately predicts prototype performance. Also, to produce results of high accuracy, this study uses a standard 60° V-notch weir for discharge measurements, with an accuracy of 3%.

One may use a system of two nonlinear equations to analyse flow in open channels

$$u_t + uu_x + gH_x + g \tan \theta = 0 \quad (2.4)$$

$$H_t + uH_x + Hu_x = 0 \quad (2.5)$$

where  $u_x$  and  $u_t$  are the spatial and temporal derivatives of the horizontal velocity component,  $H_x$  is the spatial derivative of the free surface elevation, and  $g$  is the gravity (Figure 2.8).

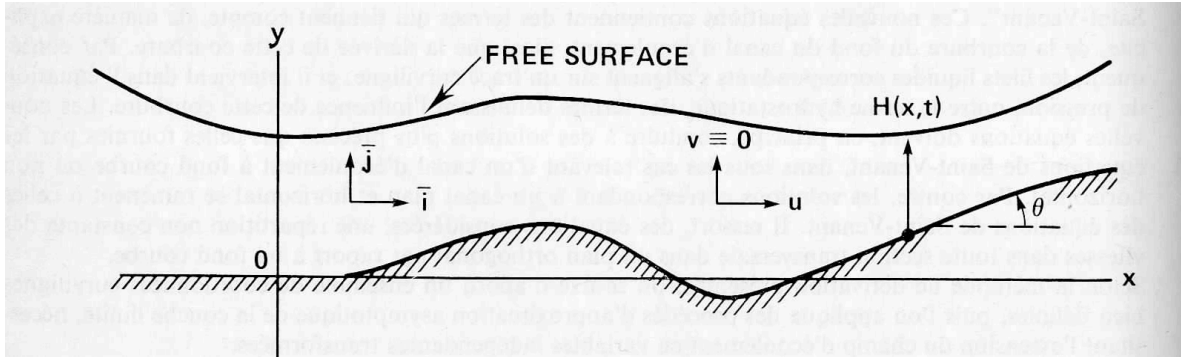


Figure 2-8. Open channel flow (Dressier 1978)

In this theory, the vertical velocity component  $v(x, t)$  has been considered to be equal to zero and the pressure is hydrostatic pressure. Therefore, these equations are not valid in the case of curved boundaries where  $v(x, t) \neq 0$ , and the pressure is not hydrostatic pressure.

Dressier (1978) derived new equations for flow over a curved open-channel surface. The new equations include new terms. These additional terms express the curvature and its derivative of the channel floor where its curvature radius is  $r=1/k$  and water depth is  $N$ . In the new equations, Dressier (1978) represented the pressure term to include the effect of streamlines curvature in addition to the hydrostatic pressure.

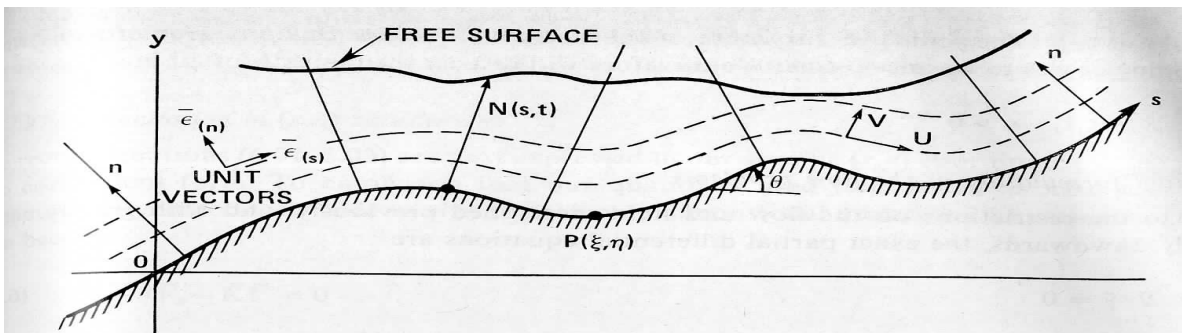


Figure 2-9. Curvilinear coordinates defined by channel boundary (Dressier 1978).



To validate the theoretical equations (Equation 2.6), a series of laboratory experiments were conducted. Models of different scales were used to compute the discharge coefficient and the effect of different siphons shapes and scales on the flow. Nine three-dimensional models were built and examined. The models were built to scales of 1/240, 1/133.5, 1/100, 1/78.9, 1/50, 1/64.9, 1/30, 1/25 and 1/10. As part of their study, Ali and Pateman (1980) compared their results obtained from mathematical analysis with laboratory results and reported a good agreement. The main disadvantage of their study was that they used inaccurate measuring instruments such as Wight for measuring discharges and orifice plates for measuring velocity. The instrument is appropriate only for relatively small discharges. Using orifice plates to measure the velocity cause large losses.

Ervine and Oliver (1980) have described the full-scale behaviour of air-regulated siphon spillways. They obtained a head-discharge relationship and the air regulation degree and discussed the stability and safety of siphon operation. The degree of air regulation becomes better, and the degree of air removal increases as the inlet lip level increases. This is an evidence that several external factors such as the wind and the shape of the inlet and the outlet may influence the flow through the siphon.

Ramamurthy et al. (1992) developed a momentum model of flow past a weir. They assumed that the slope and curvature of the streamlines vary linearly above the weir crest except in a small depth below the free water surface. Later, Ramamurthy and Diep (1994) published a study about irrotational curvilinear flow past a weir. In their study, the discharge coefficient  $C_d$  was computed mathematically and validated with  $C_d$  obtained from direct discharge measurement. Ramamurthy and Diep (1993) adapted the Dressier equation of curvilinear flow over a circular crested weir. Because the flow in the Dressier theoretical model depending on the shallow depth, this model can be adapted to study the flow under different hydraulic conditions. The discharge coefficient, flow streamlines and pressure distribution were obtained. The results from the theoretical model were validated using experimental data. They assumed that the flow is steady subcritical and two-dimensional. Also, they assumed that surface tension and viscosity do not affect the flow characteristics. In addition, they neglected the crest boundary layer thickness  $\delta$  because  $\delta$  is small in comparison to the over crest water head. Under these assumptions, Ramamurthy and Diep (1993) obtained the velocity profile as

$$\frac{u}{U_{max}} = \frac{[1 - (\frac{p}{\gamma H_1})_{cr}]^{0.5}}{(1 + \frac{y}{R})} \quad (2.7)$$

In existing theoretical models, the momentum analysis of flow, velocity field in region of the crest, and pressure distribution were analysed to study the characteristics of the flow over various types of free flow structures such as broad crested weir and long crested weir. Yet, it is very important to study the curvilinear flow behavior over the crest in case of the siphon spillway.

#### 2.4. Numerical investigation

Computational fluid dynamics (CFD) modelling allows us to simulate flow behaviour in hydraulic structures with reasonable accuracy and in an efficient manner. Savage and Johnson (2001) studied the flow behaviour over an ogee-crested spillway using a scaled physical model and a two-dimensional numerical model. In ogee-crest spillway studies, it is clear that the majority of the studies have focused on the crest section of the spillway. This is logical in that the crest is the location where flow transitions from subcritical to supercritical flow take place. The main aim of Savage and Johnson's (2001) study was to compare the results of physical and numerical models with existing literature results for flow over an uncontrolled ogee crest. The existing results were interpolated from reports of the U.S. Army Corps of Engineers (USACE, 1990) and U.S. Bureau of Reclamation (USBR, 1977). The physical model had a design head of  $H_d = 301$  mm and was built in a flume of approximately 0.30 m wide, 10 m long, and 1.22 m deep. Discharge and pressure data were recorded under ten different flow conditions ranging from  $h/H_d = 0.07$  to 1.20, where  $h$  is the effective head upstream above the crest. Results from the two-dimensional numerical model were analyzed. The ogee crested spillway was defined as an obstacle in the rectangular domain, using the fractional area/volume obstacle representation (FAVOR) method. The free surface was computed using a modified volume-of fluid (VOF) method. Non-dimensional discharge curves were used to compare the results. Pressures are compared at low, mid, and high flow conditions. The results show that there is reasonable agreement between the physical and numerical models for both pressures and discharges. These results were validated against data interpolated from the USACE's (1990) and USBR's (1977) reports, and good agreement was obtained.

High performance computers and more efficient numerical methods are available today. The behavior of ogee spillways can be investigated numerically at reasonable computing expenses. In the case of Savage and Johnson (2001), given that the CFD model achieved a good agreement with physical models, it is worth further extending the numerical work. The model can be used to extend the experimental results, in particular to investigate the effect of an increase in the flow rate and to study the velocity and pressure distributions in both subcritical and supercritical flow. For many types of spillways, the pressure over curved boundaries may be different from the hydrostatic pressure values. The differences in pressure in the curved bed are mainly due to centrifugal forces. small change in the pressure values specially if applied on large area can produce significantly different forces. for this reason and to provide accurate results, numerical modeling is sufficiently useful to analyzing 3D flow field.

More recently, a few numerical studies have been reported. For instance, Tadayan and Ramamurthy (2012) used the RNG k- $\epsilon$  model to obtain the coefficient of discharge for a siphon spillway. They validated their model predictions using results of experiments from a physical model of siphon spillway. They used the physical siphon model and a 3-D numerical model of siphon spillway and investigated curvilinear flow and the discharge coefficient.

A physical siphon spillway model was built and tested in a rectangular channel to determine the coefficient of discharge through the siphon over a range of Reynolds numbers. The siphon and the sidewalls were made of Plexiglas plates to allow for flow visualization. In cases where the conduit exit was not completely submerged, a deflector was placed at the bottom face of the lower leg to guarantee that the siphon was air-regulated.

The Reynolds-averaged Navier–Stokes equations along with the RNG k- $\epsilon$  model were used to predict the coefficient of discharge. The free surface profile was computed by using the volume of fluid method.

The data obtained from a test on a laboratory siphon model was used to evaluate the results predicted by the numerical simulations. Numerical models are less costly in terms of time and expenses compared to a physical model. With fewer resources, it is possible to made use of numerical models and to estimate siphon flow characteristics for slightly altered geometric end conditions and flow configurations.

In this way, a numerical model can generate siphon discharge coefficients. In Tadayon and Ramamurthy (2012), the results showed that regarding the relationship between  $C_d$  and  $\Delta H/d$ , the numerical predictions are in better agreement with experimental results at higher Reynolds numbers (higher  $\Delta H/d$ ) than at lower ones, as was expected (Figure 2.11).

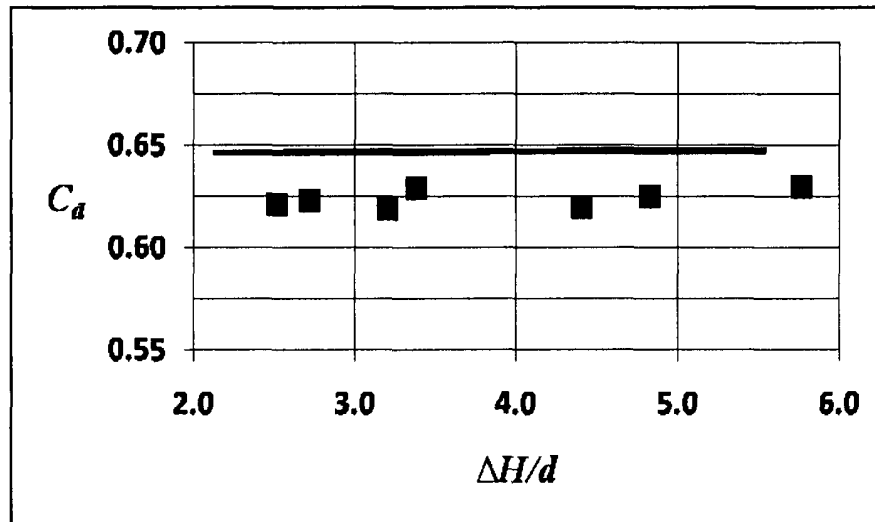


Figure 2-11. Variation of discharge coefficient with dimensionless head (Tadayon and Ramamurthy 2013)

- Experimental Data
- Numerical Results

Tadayon and Ramamurthy 2013 obtained a reasonable agreement between the numerical predictions and the experimental results.

In terms of cavitation potential in the spillways, there has been intensive studies on cavitation on flow over spillways. Researchers have attempted to find a way to predict the cavitation in spillways and measure the level of the cavitation damages by relating flow velocity and pressure with cavitation in spillways.

Frizzell et al. (2013) used experiments in a specialized reduced ambient pressure chamber to study cavitation in existing stepped spillway. using acoustic emissions technology, they studied the critical flow features that led to cavitation. The results verified the locations and patterns of cavitation occur in the low-pressure region.

Wan et al. (2018) predicted the cavitation potential of a high velocity flow in a chute spillway. They calculated the cavitation index based on the pressure and velocity numerical results

to characterize the possibility of cavitation. experimental results were validated the numerical results.

Kermani et al. (2018) studied numerically the intensity of cavitation damage and cavitation region on spillways. They used fuzzy k-nearest neighbor algorithm method to determine cavitation damage level in the spillways. They found that fuzzy-kNN model is efficient and the results can be used to help design the spillways and obtain the cavitation phenomena.

Cavitation damage on spillways investigated experimental using modeling under controlled laboratory conditions, numerically using different numerical moldings, and using a prototype-scale investigation. Yusuf and Micovic (2020) investigated a full-size spillway to determine the cavitation damage. the newly resurfaced spillway was used intensively for 300 hours before the sign of damage appears on the concrete surfaces. They obtained the cavitation index for a variety of operating conditions. the results were used opportunistically to calibrate a numerical model to promote limits that can be used to design safe spillways and avoid cavitation.

## **2.5 Summary**

The literature review shows that the design process of the siphon spillway is reasonably well understood. Several studies discussed experimental and numerical approaches to determining the discharge coefficient,  $C_d$ , of a siphon spillway and produced good results. However, the mechanisms of flow through the siphon have often been oversimplified. For instant, all the previous studies dealt with the flow through the siphon under free flow condition. Siphon discharges under submerged conditions have not been thoroughly investigated in the past.

Furthermore, the previous studies have not addressed the possibility of cavitation. Further research on this special type of spillway is required. Further research is needed to investigate discharge efficiency more comprehensively. This includes the case of a submerged outlet and its influence on flow behavior. This study will determine in detail the velocity and pressure distributions, which are important part of comprehensive flow characteristics.

## Chapter Three

### 3. Laboratory Experiments of Siphon Flow

#### 3.1. Introduction

Researchers and engineers rely on three complementary techniques to deal with complex fluid flow systems typical of many hydraulic engineering projects. The three techniques are:

- Field measurements,
- laboratory measurements,
- mathematical analysis.

Laboratory measurements using a physical hydraulic model are an incomparable tool of communication. The hydraulic model provides a three-dimensional and complete overall appreciation of a hydraulic engineering project and facilitates the explanation of the hydraulic phenomena. The hydraulic model is one elaborate method for obtaining flow features and representing the real-world prototype. Although other methods have achieved impressive successes in the field of hydraulic engineering, the physical scale model is an interactive way to study the properties of water flow. To conduct scale laboratory experiments that can be used as a tool for finding technically optimal solutions of hydraulic engineering problems, three necessary conditions for complete similarities between a hydraulic model and a prototype must be considered, namely geometric similarity, kinematic similarity and dynamic similarity.

To achieve geometric similarity, the hydraulic model must be the same shape as the prototype. All dimensions in two systems must have the same scale ratio:

$$\lambda = \frac{L_p}{L_m} \quad (3.1)$$

where  $\lambda$  is the length ratio of corresponding side of the two systems,  $L_p$  is the real prototype length, and  $L_m$  is the length in the laboratory model.

To achieve kinematic similarity, it is required that the hydraulic model and the prototype have the same length scale ratio and the same time scale ratio; thus, the velocity scale ratio will be the same for both. Under this similarity streamline patterns for the flow over the hydraulic model and the prototype will be similar. To achieve dynamic similarity, the ratios between different forces in full prototype scale must be the same in the hydraulic model scale. This requires that the hydraulic model and prototype have the same dimensionless parameters as listed in Table 3.1.

Table 3-1 Scaling ratios of forces used in physical hydraulic models

Dimensionless parameter	Force ratio	Mathematic expression (hydraulic model)	Mathematic expression (prototype)
Reynolds Number	Inertia force/viscous force	$Re_m = \frac{U_m L_m}{\nu_m}$	$Re_p = \frac{U_p L_p}{\nu_p}$
Froude Number	Inertia force/Gravity	$Fr_m = \frac{U_m}{\sqrt{g L_m}}$	$Fr_p = \frac{U_p}{\sqrt{g L_p}}$
Weber's Number	Inertia/Surface tension	$Wb_m = \frac{U_m^2}{\sigma_m / (\rho_m L_m)}$	$Wb_p = \frac{U_p^2}{\sigma_p / (\rho_p L_p)}$

In Table 3.1, the subscripts  $m$  and  $p$  refer to the scaled hydraulic model and the prototype, respectively.  $U_m$  and  $U_p$  are the characteristic flow velocities (in m/s);  $L_m$  and  $L_p$  are the characteristic lengths (in m);  $\nu_m$  and  $\nu_p$  (having the same value) are the kinematic viscosity of the water (in m<sup>2</sup>/s);  $\sigma_m$  and  $\sigma_p$  (having the same value) are the surface tension of the water (in N/m);  $\rho_m$  and  $\rho_p$  (having the same value) are the density of the water (in kg/m<sup>3</sup>);  $g$  is the acceleration due the gravity (m/s<sup>2</sup>).

Although the other methods (such as CFD) may have the ability to model hydraulic performance, physical modeling plays a key role in the process of hydraulic design, the optimisation of hydraulic structures, and the assurance of safe operations of the hydraulic structures. Also, physical modeling is the basis with which all other methods are compared (Savage & Johnson 2001). Although the laboratory experiments of siphon flow in this study were performed at a scale hydraulic model that was smaller than the normally observed scale in the field, it provides some insight into how water flows through the siphon behave in the field and reality.

In this chapter, detailed information about experimental work is presented. The focus is on considerations, assumptions, and experimental results for the purpose of evaluating the results from CFD modeling. The hydraulic aspects that are investigated are mainly the characteristics of flows along the siphon spillway such as the discharge coefficient and efficiency.

## 3.2. Experimental setup

### 3.2.1 Flume system

The flume system consists of a siphon spillway that is installed in a glass flume, a sump, a pump, pipes, a head tank, and a V-notch sharp-crested weir. A head tank (reservoir) is attached to the flume at the upstream section SC 2 (Figure 3.1). To create submerged flow at the siphon exit, a barrier (tailgate) is installed at the end of the flume. In this study, the tailgate raises the tailwater level at the downstream section SC 3. The flow rate from the pump is controlled using an adjustable valve. The maximum flow rate that could be obtained in the laboratory from the sump is  $25 \text{ m}^3/\text{s}$ .

The laboratory set-up is a recirculation system whereby it is set up in a way that allows the flow to be re-used. The conceptual laboratory setup is shown in Figure 3.1. A sketch (not to scale) of the flume and the flow loop is presented in the figure.

The flume channel has a rectangular cross section with clear glass side walls, with a working section of complete visibility of the flow and a steel bottom. The channel connects a siphon at upstream and discharges water at downstream into a V-notch tank. A floating polystyrene plate is placed at the water surface just 15 cm from the siphon exit to attenuate waves in the flume channel due to strong turbulence of the flow through the siphon.

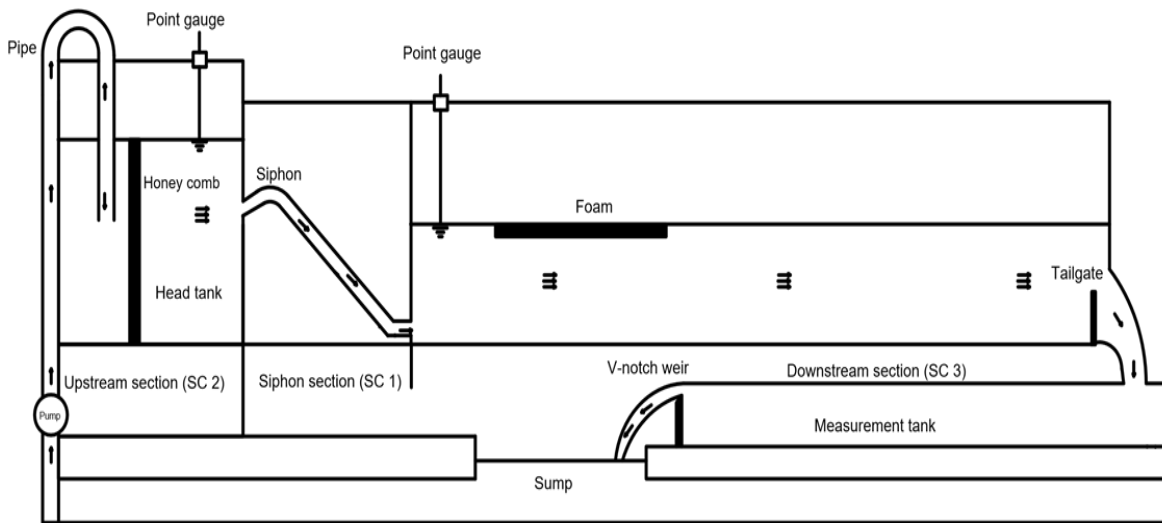


Figure 3-1 Schematic of the experimental setup used to conduct experiments, showing an upstream head tank-section, a siphon section, and a downstream channel-section. Measurement devices include point gauges and a sharp-crested V-notch weir.



Figure 3-2 Photo of the hydraulic flume in the Water Resources Laboratory at Concordia University. The flume was used for experiments of siphon flow in this study.

During an experiment, clear water is taken from an underground water storage tank (sump) available in the Water Resources Laboratory. The capacity of the sump is high enough to supply the demand of water for the experimental facilities with no interruption. A pump installed on the sump lifts water to the head tank. The sump is filled with the city water when needed. To connect the experimental facilities such as the sump, pump, and the head tank, six-inch PVC pipes are used. Some of the pipes have elbows, bends, and valves for flow control.

### 3.2.2 Head water tank

The flume is supplied with water by an elevated head tank. The purpose of this tank is to guarantee a steady and consistent water flow to the siphon. The head tank was designed with a volume of approximately  $1.8 \text{ m}^3$ . Tank dimensions are sufficient to guarantee that no boundaries influence siphon flow and it can safely hold enough water for experiments. Inside the head tank, water flows over a ramp and through a horizontal contraction. These devices were installed inside the head tank to force streamline contractions and hence damp turbulence in the reservoir water. An overflow control opening was provided at the upstream edge of the tank and enables the head tank

water level to be controlled independently of the siphon flow behaviour. It was positioned in such a way that it isolates overflow from the siphon model. The tank as well as the flume are fixed on an elevated steel structure that can support the system when fully operating (Figure 3.2).

The honeycomb is a plate made of stacks sections of small pipes on top of each other. It was placed in the head tank upstream of the siphon to attenuate flow irregularities and evenly distribute the flow. Honeycomb can eliminate turbulence as the water is forced to flow through the pipe cells (Figure 3.3).

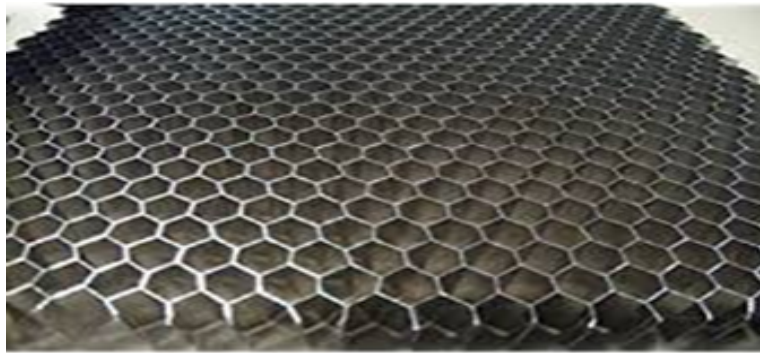


Figure 3-3 The honeycomb plate consisting of a large number of pipe cells, resembling the one used in this study. (<https://www.pinterest.ca/pin/443112050841637716/>).

### 3.2.3 Siphon

A laboratory model siphon spillway (Figure 3.4) was designed to discharge water under a negative pressure or gauge pressure below the standard atmospheric pressure (in Figure 3.4 the tubes attached to the model are piezometers to measure the wall pressure which not included in this study). The spillway was fabricated using clear acrylic (plexiglass) sheets and rods. The plastic material used was relatively easy to form into shape and produce curved surfaces and had a roughness height much smaller than the spillway conduit width and height. The small roughness height ensured negligible frictional losses of flow energy as water passed through the siphon conduit during an experiment. Prototype siphons are built using building materials such as concrete. For concrete surfaces, the roughness is higher than the smooth acrylic surfaces roughness which makes the discharge coefficient, in reality, is less than in the laboratory. The clear sidewalls of the siphon spillway were transparent for flow visualisation.

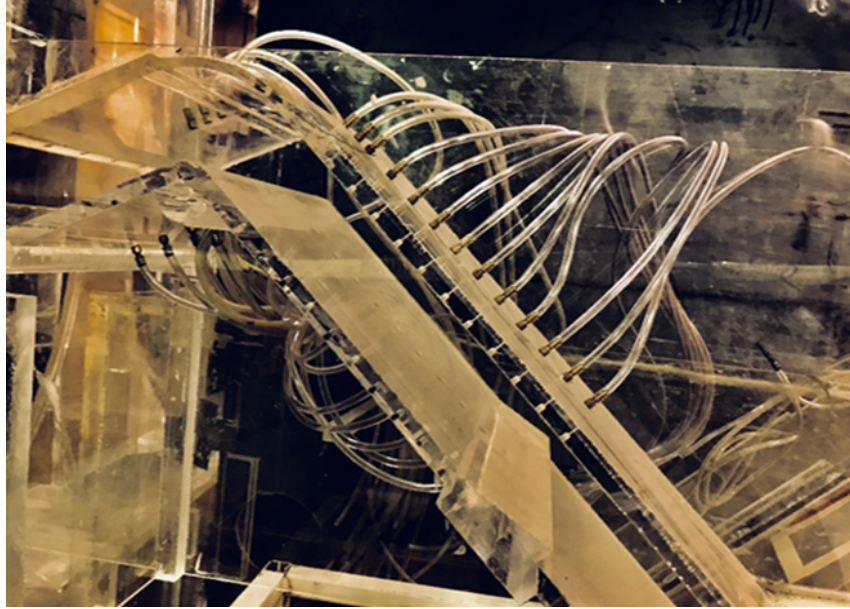
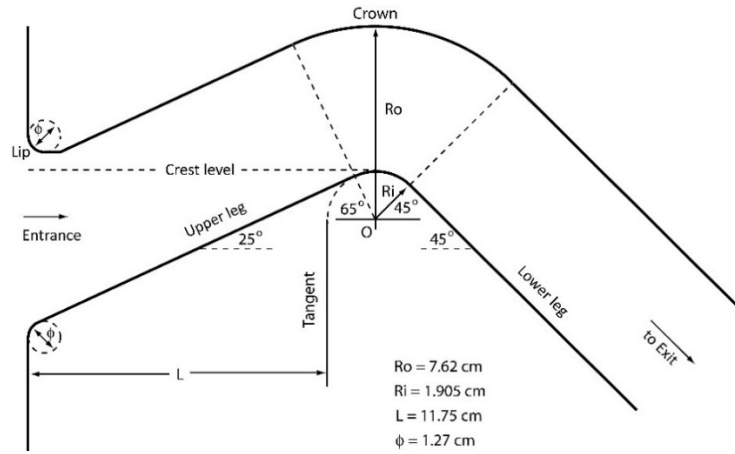


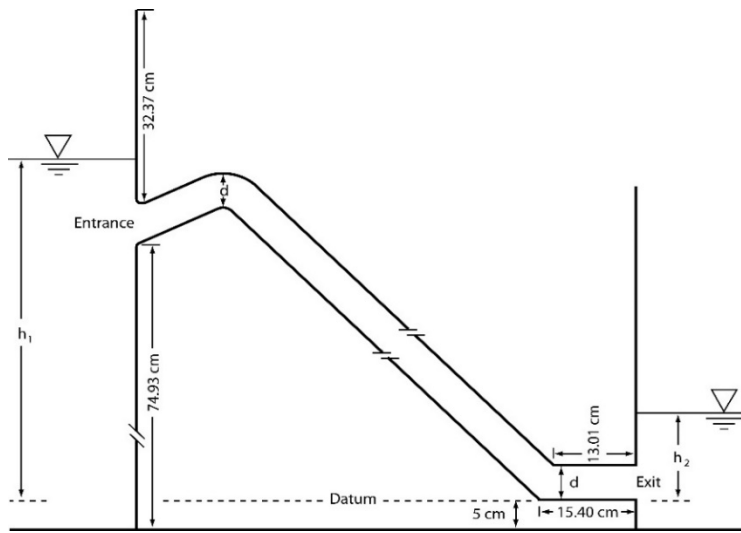
Figure 3-4 Photo of the laboratory model siphon spillway used in this study.

The siphon spillway had a rectangular, smooth entrance. The spillway conduit had a constant cross section of 25.1 cm wide ( $b = 25.1$  cm) and 5.71 cm high (the vertical distance between the spillway crest and crown  $d = 5.71$  cm). The crest and crown profile curves had a radius of 1.83 cm and 7.4 cm, respectively. Along the flow path, downstream of the crest and crown profile curves, there was a straight, tangential (to the curves) conduit section with a rectangular exit at its downstream end. The geometric details of the siphon model are given in Figure 3.5.

From previous studies, it is clear that the shape of the entrance, the geometry of the outlet, the depth of water downstream, and the size and position of the deflector can affect the flow over the siphon crest and influence the siphon discharge coefficient,  $C_d$ . For this reason, it is important to take these variables into account and verify the configuration of the entrance, crest radius, deflector shape and position, and outlet geometry. The design approach was based on Head (1975), with modifications.



(a)



(b)

Figure 3-5 Setup of siphon spillway experiments. (a) design of the crest, crown and entrance of the siphon; (b) discharge under submerged exit conditions ( $h_2/d$  well above unity).

### 3.2.4 V-notch tank

The V-notch tank is the last reservoir for recirculating water before it flows to the underground sump by gravity. The purpose of this tank is to collect the flow that comes from the flume channel and pass it over a 60° V-notch weir to measure the flow rate. The tank has a length of 304.8 cm, a width of 60.96 cm and a height of 91.44 cm (or 120"×24"×36"). These dimensions are suitable for the space available in the laboratory and give an enough volume for accurate measurements of discharge during experiments. A honeycomb plate is installed inside the tank to damp turbulence and thus improve measurement accuracy.

### 3.2.5 Flow control

A centrifugal pump provided water supply from the sump to the head tank and generated water recirculation. The flow discharge and the amount of water entering the flume system were controlled using an adjustable valve. At the downstream end of the flume channel, a tailgate was raised or lowered to regulate the downstream water level (Figure 3.1). An example of tailgates is shown in Figure 3.6. The water surface levels in the head tank and the downstream flume channel of the physical model were controlled to maintain different submergence degree at the siphon exit. Subsequently, the flow falls into a collection tank that is equipped with a V-notch weir to measure the water discharge.

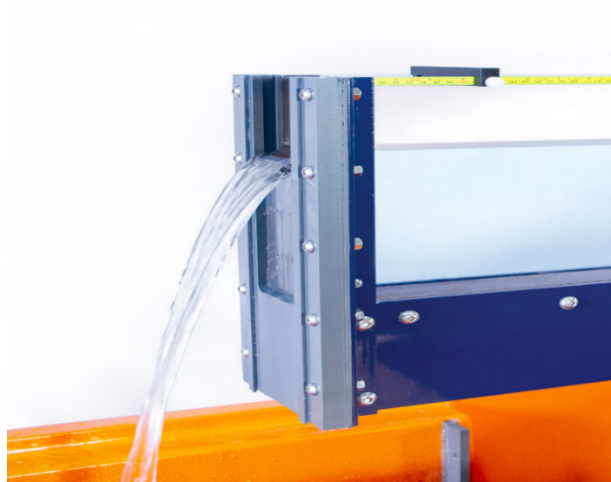


Figure 3-6 Photo of a typical tailgate in a flume channel. <https://armfield.co.uk/product/c4-mkii-multi-purpose-teaching-flume/>

### 3.2.6 Measurement instruments

In this study, experiments were performed using the siphon spillway model with different combinations of upstream and downstream water levels. Laboratory measurements were made using several instruments. The upstream and downstream water levels were measured using point gauges. These gauges had an accuracy of  $\pm 0.1$  mm. An example of point gauges, along with their mounting railing and an instrument carrier to facilitate positioning is shown in Figure 3.7. The carrier is a carriage that uses the instrument rails along the top of the flume channel and operates vertically and perpendicularly to the flume bed to provide both longitudinal and transverse movement.

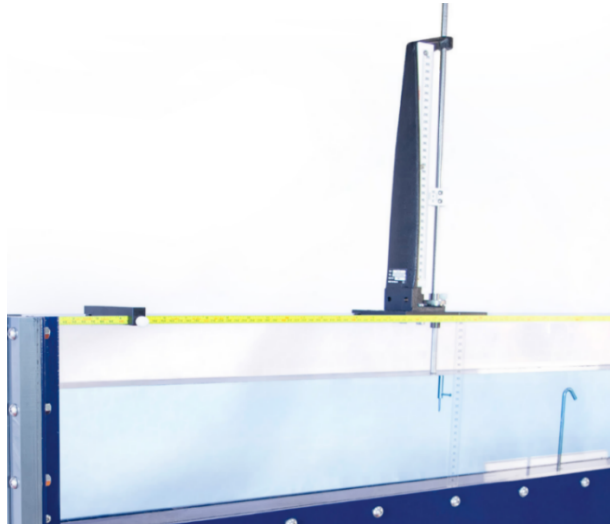
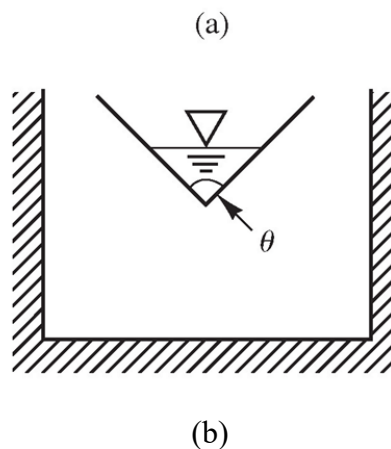


Figure 3-7 A point gauge in a flume channel to produce measurements of water level and flow depths. (<https://armfield.co.uk/product/c4-mkii-multi-purpose-teaching-flume/>)

Flow rates or discharges were measured using a standard  $60^\circ$  V-notch weir ( $\theta = 60^\circ$ ). The United States Bureau of Reclamation (USBR) 1987 suggested that the Kindsvater-Shen relationship can be used for a V-notch weir of any angle between  $25^\circ$  and  $100^\circ$ . In Figure 3.8, the flow in the approach channel has a cross-sectionally average velocity of  $V_o$  and a static head  $H$  on the weir.

The flow velocity varies from point to point in the weir opening plane. The total discharge over the weir is obtained by integrating the point velocity over all the elements of the weir opening.



(Figure 3.8 continued)

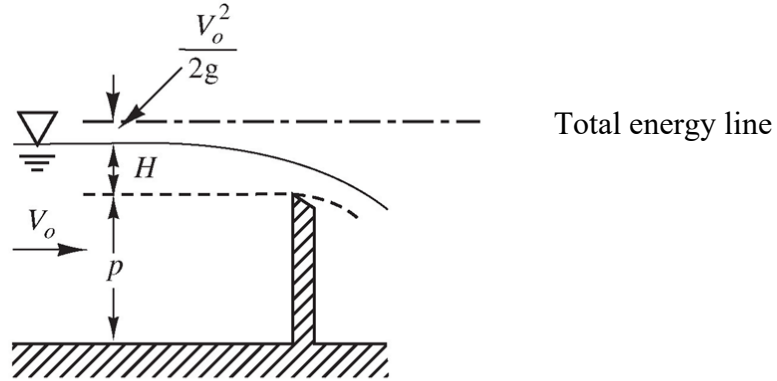


Figure 3-8 Flow over a V-notch weir: (a) cross-sectional view; (b) a longitudinal section. The total energy head of the approach flow on the weir is the sum of the static head  $H$  and the velocity  $V_o^2/2g$ .  $\theta$  is the notch angle.

### 3.3. Methods for data analysis

#### 3.3.1 Determination of flow rate through the siphon conduit

Assume that the siphon flow rate  $q$  (Figure 3.1; Figure 3.4) is steady. The flow rate  $q$  will be the same as the discharge  $Q$  of flow over the V-notch weir (Figure 3.8). Assume that the V-notch flow does not contract as it passes over the weir and that the pressure is atmospheric across the whole depth over the weir (Figure 3.8b). From the Bernoulli equation, the velocity,  $v_w$ , at any point directly above the weir can be obtained as

$$v_w = \sqrt{2gh} \quad (3.2)$$

where  $h$  is the depth being measured downwards from the total energy line, and not from the upstream water surface (Figure 3.8b);  $g$  is the gravity. The discharge can be calculated as

$$Q = \int_0^H 2(H-h) \tan\left(\frac{\theta}{2}\right) \sqrt{2gh} dh \quad (3.3)$$

$$Q = \frac{8}{15} \sqrt{2g} \tan\left(\frac{\theta}{2}\right) H^{5/2} \quad (3.4)$$

The result given by Equation (3.4) has not taken into account the effects of the flow contraction over the weir and the approach flow velocity head  $V_o^2/2g$ . The effects may be expressed by a

discharge coefficient  $C$ . Values of  $C$  range from 0.585 to 0.611 (Henderson 1966, p. 178). In this study we used  $C = 0.61$  Equation (3.4) then becomes

$$Q = \frac{8}{15} C \sqrt{2g} \tan\left(\frac{\theta}{2}\right) H^{5/2} \quad (3.5)$$

During an experiment, the static head of the approach flow  $H$  is measured using a point gauge (Figure 3.7). The discharge over the weir is determined using Equation (3.5).

### 3.3.2 Determination of the discharge coefficient of siphon flow

The siphon spillway was primed during an experiment (Figure 3.1). Consider that the siphon spillway has lowered the reservoir water level considerably; however, it is still operating under pressure flow (Figure 3.5). The Bernoulli's equation between the upstream reservoir and the downstream flume section (Figure 3.5) can be written as

$$h_1 + \frac{P_1}{\rho g} + \frac{V_1^2}{2g} = h_2 + \frac{P_2}{\rho g} + \frac{V_2^2}{2g} + h_L \quad (3.6)$$

The subscript 1 on the left side of this equation denotes the upstream reservoir or upstream water body (Figure 3.5);  $h_1$  is the water surface elevation of the upstream reservoir above a vertical datum,  $P_1$  is the gauge pressure at the water surface ( $P_1 = 0$ ),  $\rho$  is the density of water, and  $V_1$  is the velocity at which the upstream water surface lowers as water flows through the siphon conduit. In reality,  $V_1$  is very small, and the velocity head  $V_1^2/2g$  is negligible, compared to  $h_1$ . The subscript 2 on the right side of Equation (3.6) denotes the downstream water body (Figure 3.5), and similarly  $P_2 = 0$  and  $V_2^2/2g = 0$ .

In Equation (3.6),  $h_L$  is the sum of flow energy head losses that occur as water passes through the siphon entrance, conduit and exit. The head losses occur because of flow separation, turbulent eddy motion, and friction at the solid walls of the conduit. It is convenient to express  $h_L$  in terms of the velocity head based on the cross-sectionally averaged siphon flow velocity,  $V_s$ , as  $h_L = C_L V_s^2/2g$ , where  $C_L$  is an energy loss coefficient.  $V_s$  is equal to siphon flow rate  $q$  divided by the cross-section area  $A$  of the siphon conduit. Thus, Equation (3.6) reduces to

$$C_L \frac{q^2}{2gA^2} = h_1 - h_2 \quad (3.7)$$

This equation states that the energy head available to drive siphon flow is  $Dh = h_1 - h_2$  (Gribbin 2014, p. 96). For given values of  $Dh$  and  $A$ , the larger the value of  $C_L$  (due to severer flow separation and stronger turbulent eddy motion in the siphon conduit), the lower the flow rate  $q$  carried by the siphon. In other words, the discharge efficiency of the siphon is inversely proportional to the value of  $C_L$ . One may express the discharge coefficient as  $C_d = 1/C_L$  and rewrite Equation (3.7) as

$$q = C_d A \sqrt{2g\Delta h} \quad (3.8)$$

When the siphoning action occurs, the siphon acts as a pipe. Estimates of the Reynolds number  $Re_m$  of the hydraulic model (Table 3.1) are obtained using the following characteristic velocity  $U_m = \sqrt{2g\Delta h}$  and characteristic length  $L_m = 2A/(d + b)$ , which is the hydraulic radius multiplied by a factor of four. The Reynolds number is given by

$$Re_m = \frac{2A\sqrt{2g\Delta h}}{(d + b)v_w} \quad (3.9)$$

where  $v_w$  is the viscosity of water.

### 3.4 Experimental results and discussions

Six experiments (Table 3.2) of siphon flows under submerged exit conditions in a range of  $h_1$  and  $h_2$  values (Figure 3.5) were carried out. Each of the experiments reached a state of equilibrium, after  $h_1$ ,  $h_2$  and  $q$  had adjusted to constant values. Different constant values were achieved by controlling the pump valve and the tailgate. At a selected flow rate  $q$  (by setting the valve opening), when the tailgate was pivoted up to raise the downstream water level  $h_2$  for a larger submergence, the upstream water level  $h_1$  adjusted itself. In each experiment, the flow was allowed to adjust itself until a dynamic balance was reached before making measurements.

For each experiment, point gauge measurements of the static head  $H$  of the approach flow in the V-notch tank were made multiple times. This was to confirm that the point gauge readings showed no significant changes. Equation (3.5) took  $H$  as input and gave the discharge  $Q$  over the weir. In the upstream tank, point gauge measurements of the water levels at a few locations around the centreline were made and the average of the readings gave the value of  $h_1$ . The same procedures were followed to obtain the value of  $h_2$ . At an equilibrium, the siphon flow rate  $q$  was equal to  $Q$ .

Equation (3.8) gave the value of the discharge coefficient  $C_d$ . The results are presented in Table 3.2.

Table 3-2 Hydraulic conditions and discharge coefficient for experiments under submerged exit conditions. The vertical datum is located at the obvert of the exit of the siphon.

Experiment	$q$ (m <sup>3</sup> /s)	$h_1$ (m)	$h_2$ (m)	$Dh/d$	$h_2/d$	$Re_m$	$C_d$
E1	0.024	0.515	0.153	6.307	2.666	249003	0.625
E2	0.025	0.507	0.178	5.732	3.101	237382	0.683
E3	0.024	0.468	0.106	6.307	1.847	249003	0.625
E4	0.022	0.519	0.210	5.383	3.659	230054	0.620
E5	0.024	0.562	0.225	5.871	3.920	240251	0.648
E6	0.024	0.527	0.175	6.132	3.049	245540	0.634

In this study, the model spillway was tested at six different submergence levels, with  $1.8 < h_2/d < 4$ . The design of the siphon was selected on the basis of a study done by Head (1975). The Reynolds number is high enough to overcome viscous effects, which are negligible at prototype scale. In Chapter Four, the experimental results of  $C_d$  will be used for comparisons with values of  $C_d$  at different dimensionless heads from numerical simulations. The head normalisation allows a comparison in the simplest form. The calculated discharge coefficient from the physical hydraulic model serves as a basis for CFD computations.

The experimental results of siphon flow offer useful data for verifying the accuracy of numerical results. The experimental and numerical results can be presented in terms of the discharge coefficient as it varies with the hydraulic head. Such study gives a considerable aid in the design and operation of the siphon. The high Reynolds number in all the measurements is high,

indicating that the flows are fully turbulent. The effect of viscosity decreases as the Reynolds number increases; numerical results should become closer to experimental results at higher  $\Delta h/d$ . The discharge coefficient in the case of submerged exit is about 0.62 to 0.67. Tadayon and Ramamurthy (2013) reported that the discharge coefficient in the case of free flow is between 0.62 and 0.63. Therefore, the two cases have essentially the same  $C_d$  values.

A practical challenge in the experimental work was due to the fact that the individual experiments were conducted on different dates. However, it was often desirable to achieve certain flow rates among the experiments. The accuracy of the pump was good in terms of flow rate. The water flow rate delivered by the pump well matches the required/desired value of flow. Also, the pump was sensitive to any small change made with the adjustive valve. However, the delivered flow was unsteady flow at the beginning of turning on the pump or at the time when changing the flow rate for different experiments. For this reason, five-minutes waiting time was required before starting to take measurements.

Although the flow entering the head tank from the pump is turbulent flow, the honeycomb, ramp, and the horizontal contraction that were built inside the head tank played a significant role in regulating the flow before it entered the siphon. The downstream flume channel is a narrow open channel. This classification is based on its aspect ratio or the ratio of the channel width to the flow depth. A channel is classified as a narrow open channel if its aspect ratio smaller than five and a wide channel if its aspect ratio is large than 10 (Chow 1959, p. 26). The narrow open channels show that strong secondary flow is developed due to the effect of the sidewalls. In this study, all the measurements were taken at the centreline of the flume to avoid possible sidewall effect.

### **3.5 Conclusions**

A closed loop flume system was used in the laboratory to drive water flow through a siphon spillway. The ultimate purpose of this study is to build a siphon model with high discharge efficiency or high siphon discharge coefficient. The flume system consists of a flume channel, a head tank, a V-notch tank, a pump and an underground water storage sump. The head tank (reservoir) was attached to the spillway conduit's entrance on the upstream side, which allowed the reservoir water level to rise above the flume sidewall height. A tailgate was fixed downstream of the flume to control the water level. Tests were performed on the siphon model with different combinations of upstream and downstream water levels. The discharge coefficient data for the

siphon experiments will be used to verify the accuracy of the numerical results presented in the next chapter.

In summary, for the first time, experiments of a siphon spillway under submerged exit conditions have been conducted. The dimensionless submergence levels range from  $h_2/d = 1.86$  to 3.94. The dimensionless driving head  $\Delta h/d$  reaches 6.34. The experiments produce the discharge coefficient  $C_d$  that has a mean value of 0.64 and a standard deviation of 0.024. The  $C_d$  values show little changes from those for a siphon of similar design under free discharge conditions. The  $C_d$  values from this study reflect realistic flow situations with negligible viscous effects inside the siphon and with the dominance of gravity as the driving force.

## Chapter Four

### 4. Numerical Modelling of Flow through Siphon Spillway

#### 4.1. Introduction

This chapter presents the theory and procedures of three-dimensional CFD modelling, including the specifications of initial and boundary conditions, solution techniques and numerical accuracy. The results of velocity and pressure distributions obtained from three-dimensional modelling are discussed. Three different  $k-\varepsilon$  models are used for turbulence closure and their performances are assessed. Also, this chapter provides a comparison of the model results produced from three different mesh sizes.

In open channels, almost all the flows are turbulent flows (Tennekes et al. 1972). Turbulent flow is naturally unsteady flow that is characterised by high levels of fluctuating vorticity, rotational, and three-dimensionality (Tennekes et al. 1972).

Siphon spillways are used to regulate water levels in flood protection structures. Siphon consists of two tangential sides and a circular crest region. Water flow from the upstream reservoir over the siphon crest is curvilinear three-dimension flow (Head 1971).

To simulate the flow through the siphon spillway, three-dimensional geometry was reproduced using the CFD code FLUENT. In Figure 4.1, the siphon connects the upstream reservoir with the downstream open channel, with a tailgate at the downstream end in order to keep the water level in the channel above the outlet upper face level.

Numerical modelling is less expensive and time consuming than physical modelling. In addition, numerical modelling has the advantage in accommodating different boundary conditions and flow geometry configurations. In particular, numerical modelling can be readily implemented to reproduce the flow field under a wide range of Reynolds numbers.

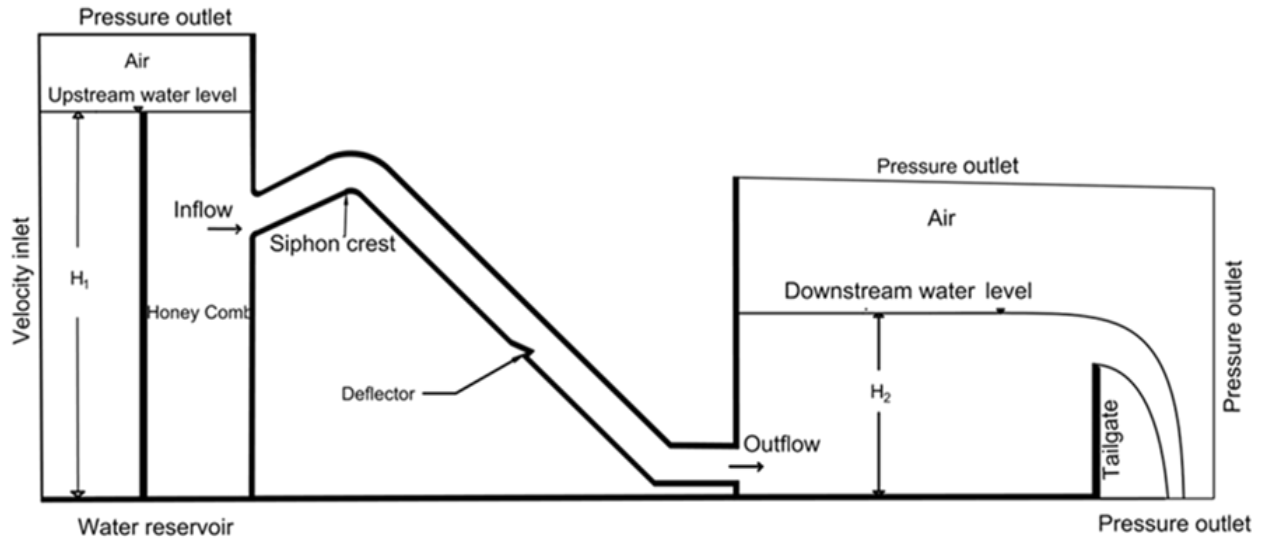


Figure 4-1. Longitudinal section of the siphon spillway showing the siphon in the middle, water reservoir to the left of the siphon, and a rectangular flume channel to the right.

#### 4.2. Reynolds-averaged continuity and momentum equations

The Reynolds-averaged Navier–Stokes (RANS) equations describe the motion of an incompressible fluid mixture. The fluid mixture consists of air as the gas phase and water as the liquid phase. The two phases are assumed to be immiscible. Turbulence consists of random fluctuations of various flow properties. Therefore, in turbulence flow all quantities are expressed as the sum of mean and fluctuating parts (Wilcox 2004). To derive RANS equations of three-dimensional turbulent flow, the velocity and pressure fields are decomposed as follows:

$$u_i = U_i + u'_i \quad \text{for } i = 1, 2, 3 \quad (4.1)$$

$$p = P + p'$$

where  $u_i$  indicates the instantaneous velocity components  $(u_1, u_2, u_3)$  in the Cartesian coordinates  $(x_1, x_2, x_3)$ ,  $(U_1, U_2, U_3)$  are the time-averaged parts, and  $(u'_1, u'_2, u'_3)$  fluctuating parts, respectively. Similarly,  $p$  is the instantaneous pressure,  $P$  is the time-averaged part, and  $p'$  is the fluctuating part. To facilitate discussions, the following symbols are used interchangeably, i.e., they are identical:  $U_1 \equiv U$ ;  $U_2 \equiv V$ ;  $U_3 \equiv W$ ;  $x_1 \equiv x$ ;  $x_2 \equiv y$ ;  $x_3 \equiv z$ .

### 4.2.1 Continuity equations

For the motion of an incompressible fluid mixture, the conservation of mass is expressed by the continuity equation in three dimensions. The continuity equation in tensor form is given as:

$$\frac{\partial U_i}{\partial x_i} = 0 \quad (4.2)$$

Equation (4.2) expands into  $\frac{\partial U_1}{\partial x_1} + \frac{\partial U_2}{\partial x_2} + \frac{\partial U_3}{\partial x_3} = 0$  or  $\frac{\partial U}{\partial x} + \frac{\partial V}{\partial y} + \frac{\partial W}{\partial z} = 0$  in component form.

### 4.2.2 The volume of fluid method

The flow has a free surface in the upstream reservoir as well as in the downstream channel. The position of the free surface changes with space and with time, and therefore it needs to be computed. The volume of fluid method is an efficient and convenient way to track the free surface position during a simulation. The density of air-water mixture,  $\rho$ , is calculated as the volume-weighted average

$$\rho = \alpha_a \rho_a + \alpha_w \rho_w \quad (4.3)$$

and the viscosity of air-water mixture,  $\nu$ , is calculated also as the volume-weighted average

$$\nu = \alpha_a \nu_a + \alpha_w \nu_w \quad (4.4)$$

where  $\alpha$  is the volume fraction, the subscripts  $a$  and  $w$  denote air and water, respectively, and  $\alpha_a + \alpha_w = 1$  for any computational cell. In a computational cell,  $\alpha_w = 1$  means that the cell is occupied completely by water, and conversely  $\alpha_a = 1$  means that the cell is occupied completely by air. A cell in the free surface region (Figure 4.1) partially occupied by water will have  $0 < \alpha_a < 1$ . The volume of fluid method computes the change of  $\alpha_a$  with time and space using a continuity equation (or equivalently the mass conservation equation)

$$\frac{\partial \alpha_a}{\partial t} + \frac{\partial}{\partial x_j} (\alpha_a U_j) = 0 \quad (4.5a)$$

where  $t$  is time. The change of  $\alpha_w$  with time and space is calculated from

$$\alpha_w = 1 - \alpha_a \quad (4.5b)$$

### 4.2.3 Momentum equations

The Reynolds averaged equations for the conservation of momentum equations are given by

$$\frac{\partial U_i}{\partial t} + U_j \frac{\partial U_i}{\partial x_j} = -\frac{1}{\rho} \frac{\partial P}{\partial x_i} + \frac{\partial}{\partial x_j} \left( \nu \frac{\partial U_i}{\partial x_j} + \tau_{ij} \right) + g_i \quad (4.6)$$

where  $i = 1, 2$  and  $3$ ;  $g_i$  is the gravitational acceleration in the  $x_i$  direction. On the left-hand side of Equation (4.6), the first term is unsteady term and the second term is the momentum advection term. On the right-hand side of the equation, the first term is the pressure gradient, the second term is the sum of viscous term diffusion and, and the specific Reynolds stress.

The specific Reynolds stress tensor,  $\tau_{ij}$ , and the mean strain-rate tensor,  $S_{ij}$ , are defined as follows:

$$\tau_{ij} = \begin{pmatrix} \tau_{11} & \tau_{12} & \tau_{13} \\ \tau_{21} & \tau_{22} & \tau_{23} \\ \tau_{31} & \tau_{32} & \tau_{33} \end{pmatrix} \quad (4.7)$$

$$S_{ij} = \frac{1}{2} \left( \frac{\partial U_i}{\partial x_j} + \frac{\partial U_j}{\partial x_i} \right) \quad (4.8)$$

Based on the Boussinesq approximation, the components of the Reynolds stress tensor vary linearly with the mean strain rate, which can be written as follows:

$$\tau_{ij} = 2\nu_T S_{ij} - \frac{2}{3} k \delta_{ij} \quad (4.9)$$

where  $\nu_T$  is the turbulent eddy viscosity,  $k$  is the specific turbulence kinetic energy, and  $\delta_{ij}$  is the Kronecker delta (equal to one for  $i = j$  and zero otherwise).

### 4.3. Turbulence closure

In RANS equations (Equation 4.6), Reynold's decomposition separates the average and fluctuating parts of instantaneous pressure and velocities in original unsteady Navier-Stokes equations (Wilcox, 2007). As a result of quantities being expressed as the sum of mean and fluctuating parts, additional terms (Reynold's stress components given in Equation 4.7) are introduced as extra unknowns. These unknown components are in addition to the six unknown variables:  $U_1, U_2, U_3, P, \alpha_a,$  and  $\alpha_w$ . There are only six governing equations: Equation (4.2); Equations (4.5a) and (4.5b); and Equation (4.6) for  $i = 1, 2$  and  $3$ . The system of equations is not closed because there are more unknown variables than the number of equations. To close the system, turbulence model equations for computation of  $\tau_{ij}$  (Equation 4.9) are required. This is the so-called turbulence closure problem. The problem boils down to how to compute the eddy viscosity that appears in Equation (4.9).

The  $k$ - $\varepsilon$  turbulence model predicts and simulates accurately the characteristics of near-wall boundary flows and flows in curved boundaries. This model uses two transport equations: One describes the spatial and temporal change of  $k$ ; other describes the spatial and temporal change of the rate of dissipation  $\varepsilon$  of  $k$ . Note that  $k$  has the dimensions  $m^2/s^2$ ,  $\varepsilon$  has the dimensions  $m^2/s^3$ , and  $\nu_T$  has the dimensions as  $\nu$  or  $m^2/s$ . Based on dimension analysis and Buckingham  $\pi$  theorem, we obtained  $L^2T^{-1} = K^n\varepsilon^m$ ,  $L^2T^{-1} = (L^2T^{-2})^n(L^2\varepsilon^{-3})^m$ ,  $2 = 2n + 2m$ ,  $-1 = -2n - 3m$ ,  $n = 2$  and  $m = -1$ ,  $L^2T^{-1} = K^2\varepsilon^{-1}$ , and the turbulent eddy viscosity can be formulated as follows (Wilcox 2007):

$$\nu_T = C_\mu k^2 / \varepsilon \quad (4.10)$$

where  $C_\mu$  is an empirical closure constant. In Equation (4.10),  $k^{1/2}$  having the dimensions  $m/s$  can be interpreted to give estimates of a turbulent velocity scale, and  $k^{3/2}/\varepsilon$  having the dimension  $m$  gives estimates of a turbulent length scale. In order to calculate values of  $\nu_T$  on the mesh,  $k$  and  $\varepsilon$  need to be obtained from solving the two transport equations.

Several authors have studied the curvilinear flow passing spillways and they tried to predict the flow characteristics using different numerical models. Wilcox (2007) described several numerical models that have been widely used in flow modelling. Tadayon and Ramamurthy (2009) provided a comparative study to analyse the characteristics of the flow over circular spillways. They studied the performances of three different turbulence models provided in the commercial code FLUENT:

1. The standard k- $\epsilon$  model was proposed (Jones and Launder, 1972),
2. The Renormalization-group (RNG) k- $\epsilon$  model (Yakhot & Orszag 1986),
3. The Realizable k- $\epsilon$  model (Shih et al. 1995).

The standard k-e turbulence closure model, the RNG k-e turbulence closure model, and the Realizable k-e turbulence closure model are two equation complete models for modeling the turbulent flows. These models can determine the turbulence velocity and length scale by solving two separate transport equations. All three models have similar forms, with transport equations for k and  $\epsilon$ . The major differences in the models lie in (Fluent User's Guide, 4.4, Ansys Inc, USA, 2009):

1. the method of calculating turbulent eddy viscosity,
2. the turbulent Prandtl numbers governing the turbulent diffusion of k and  $\epsilon$ ,
3. the generation and destruction terms in the  $\epsilon$  equation.

#### 4.3.1 The standard k- $\epsilon$ model

The standard k- $\epsilon$  model is the simplest and most popular two-equation model. It was proposed by Launder and Spalding (1972). This model expresses the turbulent viscosity in terms of turbulent kinetic energy  $k$  and dissipation rate of turbulence kinetic energy  $\epsilon$  (Equation 4.10). These two turbulent quantities are calculated from transport equations as given in Fluent User's Guide Section 4.4.1 (Ansys Inc. 2009)

$$\frac{\partial}{\partial t}(\rho k) + \frac{\partial}{\partial x_i}(\rho k u_i) = \frac{\partial}{\partial x_j} \left[ \left( \mu + \frac{\mu_t}{\sigma_k} \right) \frac{\partial k}{\partial x_j} \right] + G_k + G_b - \rho \epsilon - Y_M + S_k \quad (4.11)$$

$$\frac{\partial}{\partial t}(\rho\varepsilon) + \frac{\partial}{\partial x_i}(\rho\varepsilon u_i) = \frac{\partial}{\partial x_j} \left[ \left( \mu + \frac{\mu_t}{\sigma_\varepsilon} \right) \frac{\partial \varepsilon}{\partial x_j} \right] + C_{1\varepsilon} \frac{\varepsilon}{k} (G_k + C_{3\varepsilon} G_b) - C_{2\varepsilon} \rho \frac{\varepsilon^2}{k} + S_\varepsilon \quad (4.12)$$

where  $G_k$  is the generation of turbulence kinetic energy due to the mean velocity gradients,  $G_b$  is the generation of turbulence kinetic energy due to buoyancy,  $Y_M$  is the contribution of the fluctuating dilatation in compressible turbulence to the overall dissipation rate,  $S_k$  and  $S_\varepsilon$  are source terms. The terms  $Y_M$ ,  $S_k$  and  $S_\varepsilon$  equal zero in the case of flow through the siphon spillway.

The values of the constants in the Standard k- $\varepsilon$  model equation (4.12) are:  $C_{\varepsilon_1} = 1.44$ ;  $C_{\varepsilon_2} = 1.92$ ;  $\sigma_k = 1.0$ ;  $\sigma_\varepsilon = 1.3$ . The value of  $C_\mu$  in Equation (4.10) is constant and equals  $C_\mu = 0.09$  (Launder and Spalding, 1974).

The standard k- $\varepsilon$  model is built on the assumption that the effect of molecular viscosity is negligible and the flow is fully turbulent. The standard k- $\varepsilon$  model is therefore valid only for flows with high Reynolds number.

### 4.3.2 The RNG k- $\varepsilon$ model

To improve the accuracy of the solution for turbulence flows and curvilinear flows, Yakhot and Orszag (1986) adapted the standard k- $\varepsilon$  model and derived RNG k- $\varepsilon$  model by using statistical technique called Renormalization Group (RNG) Theory. The RNG k- $\varepsilon$  model considers an additional term in the  $\varepsilon$  equation, which leads to an improved accuracy of solution for rapidly varied flows and curvilinear flows. Besides, one more thing that makes the RNG model different from the standard k- $\varepsilon$  model is that while the standard k- $\varepsilon$  model is a high-Reynolds-number version of k- $\varepsilon$  model, the RNG k- $\varepsilon$  model is valid in both high- and low-Reynolds-number regions of the flow. Because of this feature, the RNG k- $\varepsilon$  model is suitable and more accurate for a wider range of flows than the standard k- $\varepsilon$  model. In RNG k- $\varepsilon$  model, the turbulence kinetic energy and the dissipation are given in Fluent User's Guide Section 4.4.2 (Ansys Inc. 2009) as:

$$\frac{\partial}{\partial t}(\rho k) + \frac{\partial}{\partial x_i}(\rho k u_i) = \frac{\partial}{\partial x_j} \left( \alpha_k \mu_{eff} \frac{\partial k}{\partial x_j} \right) + G_k + G_b - \rho \varepsilon - Y_M + S_k \quad (4.13)$$

$$\frac{\partial}{\partial t}(\rho\varepsilon) + \frac{\partial}{\partial x_i}(\rho\varepsilon u_i) = \frac{\partial}{\partial x_j} \left( \alpha_\varepsilon \mu_{eff} \frac{\partial \varepsilon}{\partial x_j} \right) + C_{1\varepsilon} \frac{\varepsilon}{k} (G_k + C_{3\varepsilon} G_b) - C_{2\varepsilon} \rho \frac{\varepsilon^2}{k} + S_\varepsilon \quad (4.14)$$

where  $\mu_{eff}$  is the effective viscosity and the quantities  $\alpha_k$  and  $\alpha_\varepsilon$  are the inverse effective Prandtl numbers for  $k$  and  $\varepsilon$ , respectively. The terms  $Y_M$ ,  $S_k$  and  $S_\varepsilon$  equal zero in the case of flow through the siphon spillway. The empirical closure constants are:  $C_{1\varepsilon} = 1.42$ ,  $C_{2\varepsilon} = 1.68$ ,  $\alpha_k = \alpha_\varepsilon = 1.393$ , and  $C_\mu = 0.0845$  (Yakhot and Smith 1992).

$$d \left( \frac{\rho^2 k}{\sqrt{\varepsilon \mu}} \right) = 1.72 \frac{\hat{v}}{\sqrt{\hat{v}^3 - 1 + C_v}} d\hat{v} \quad (4.15)$$

where  $C_v = 100$  and effective turbulent transport ( $\hat{v}$ ) varies with the effective Reynolds number:

$$\hat{v} = \frac{\mu_{eff}}{\mu} \quad (4.16)$$

### 4.3.3 Realizable k- $\varepsilon$ model

Shih et al. (1995) developed and applied substantial improvements on the standard k- $\varepsilon$  model to be more appropriate for variety types of flows including boundary layer flows and separated flows. This k- $\varepsilon$  model consists of a new model dissipation rate equation ( $\varepsilon$ ) and a new realizable eddy viscosity formulation. The realizability constraints were achieved by the turbulent eddy viscosity ( $C_\mu$ ). In the Realizable k- $\varepsilon$  model,  $C_\mu$  is a function of the turbulent fields, mean strain and rotation rates and it is no longer a constant. Generally, the Realizable k- $\varepsilon$  model is an upgraded version of the standard k- $\varepsilon$  model that more accurately predicts flow characteristics including streamline curvature in curvilinear flow, vortices, and rotation (Shih et al. 1995).

The transport equations for turbulence kinetic energy  $k$  and the dissipation rate of  $k$  in the realizable k- $\varepsilon$  model are [Fluent User's Guide, 4.4.3, (Ansys Inc. 2009)]:

$$\frac{\partial}{\partial t}(\rho k) + \frac{\partial}{\partial x_i}(\rho k u_i) = \frac{\partial}{\partial x_j} \left[ \left( \mu + \frac{\mu_t}{\sigma_k} \right) \frac{\partial k}{\partial x_j} \right] + G_k + G_b - \rho \varepsilon - Y_M + S_k \quad (4.17)$$

$$\frac{\partial}{\partial t}(\rho\varepsilon) + \frac{\partial}{\partial x_i}(\rho\varepsilon u_i) = \frac{\partial}{\partial x_j} \left[ \left( \mu + \frac{\mu_t}{\sigma_\varepsilon} \right) \frac{\partial \varepsilon}{\partial x_j} \right] + \rho C_1 S_\varepsilon - \rho C_2 \frac{\varepsilon^2}{k + \sqrt{v_\varepsilon}} + C_{1\varepsilon} \frac{\varepsilon}{k} C_{3\varepsilon} G_b + S_\varepsilon \quad (4.18)$$

where

$$C_1 = \max \left[ 0.43, \frac{\eta}{\eta + 5} \right], \quad \eta = S \frac{k}{\varepsilon}, \quad S = \sqrt{2S_{ij}S_{ij}}$$

In equation (4. 17), the  $G_k$  is the generation of turbulence kinetic energy related to the gradients of the mean velocity and  $G_b$  is the generation of turbulence kinetic energy. While  $Y_M$  represents the contribution of the fluctuating of the turbulence to the overall dissipation rate.  $C_1$ ,  $C_2$ ,  $C_{1\varepsilon}$  and  $C_{3\varepsilon}$  are constants.  $S_k$  and  $S_\varepsilon$  are the source terms. The terms  $Y_M$ ,  $S_k$  and  $S_\varepsilon$  equal zero in the case of flow through the siphon spillway.

#### 4.4. Description of model parameters

##### 4.4.1 Geometry

The purpose of this section is to give an overview of CFD model simulations of siphon flow. A three-dimensional (3-D) model is required to accurately represent secondary flows in the crest region of the siphon spillway. The model domain consists of an upstream rectangular water tank section, the siphon section, and a downstream rectangular open channel section. The three sections are marked as L1, L2 and L3 in Figure 4.2. The CFD model geometry matched the physical model.

For laboratory experiments, the siphon conduit was constructed using 12-mm thick Plexiglas sheets. The width of the conduit was  $b = 25.1$  cm. The upstream water tank has a sidewall height of 113 cm, length of 80 cm, and a width of 40 cm. The downstream channel section is a height of 60 cm, length of 10m, and weight of 30cm. A tailgate was placed at the end of the downstream channel section to control the water level in the downstream channel section. The flow was subcritical and fully turbulent. The siphon outflow opening was completely submerged for all model runs.

#### 4.4.2 Free surface tracking

The free-surface position was obtained using the volume of fluid (VOF) method, which is suitable for application to two phases air-water flows. The VOF method rests on conceptualisations involving a fractional volume of fluid (Hirt and Nicholls 1981). This method calculates the shape and location of a constant-pressure free surface boundary, according to a filling process which identifies which cell in the mesh volume is filled with water and which is emptied. The water volume fraction  $\alpha_w$  is equal to one if the cell is completely filled with water and zero if the cell is completely emptied. Knowing the fraction of water in each cell allows us to locate free surface and to further calculate free surface slopes and curvatures. The free surface can be easily located through the partially filled cells or between the full and empty cells.

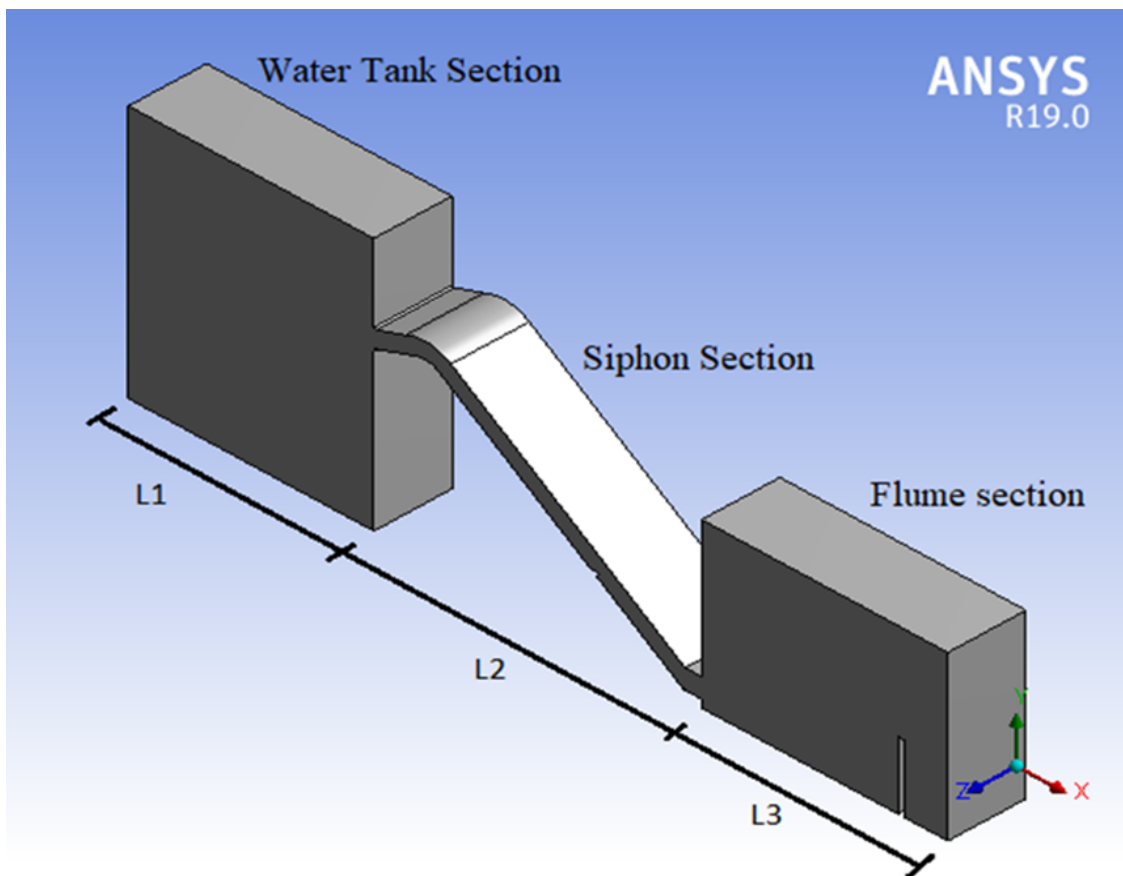


Figure 4-2. Three sections of the model domain, where the length of the reservoir (water tank) section is  $L_1 = 80$  cm, the length of the siphon is  $L_2 = 77.54$ cm, and the length of the downstream flume section is  $L_3 = 80$  cm.

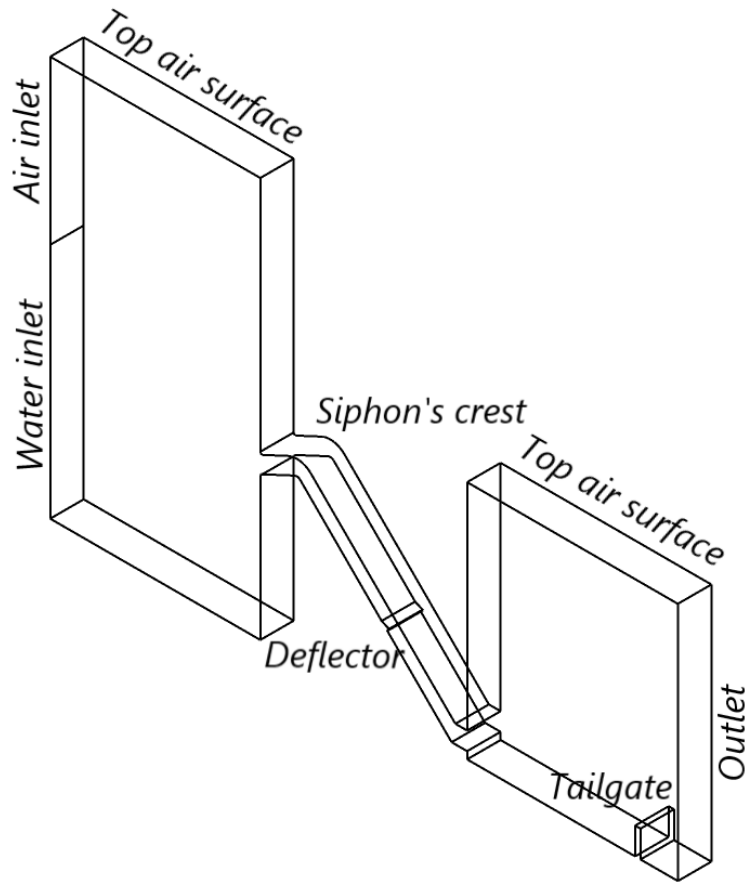


Figure 4-3. Three-dimensional geometry of the siphon and connecting sections.

#### 4.4.3 Grid generation

The geometry of the siphon spillway model domain was subdivided into a large number of small control volumes. The number and the size of cells in the geometry significantly affect the computing time. Increasing the number of cells leads to an increase in the calculations per iteration. In addition, a smaller cell size requires a smaller time step ( $\Delta t < \Delta x/U_i$  where  $\Delta x$  is the smallest cell size and  $U_i$  is the local velocity) and this further increases the computing time. The mesh quality has influence on the accuracy of the solution. This is a very important point in computational fluid dynamics. Given the significant impact of mesh on accuracy, convergence and computing costs, it is important to test different mesh configurations in flow simulations. The

FLUENT software package was used to generate the mesh in this study. Structured mesh has been used for most regions of the model domain in order to increase the speed of computations. Figure 4.4 depicts the schematic representation of the three-dimensional model mesh. The mesh sizes varied from 2 to 5 mm and a total of about 559051 computational cells were used to cover the model domain. The mesh allowed fine resolutions in the crest region that requires small computational cells to provide an adequate resolution of the model results (Figure 4.4b).

Furthermore, regions next to solid boundaries were meshed with a power law function that generated the finer mesh. However, less fine for the upstream head tank and the downstream open channel regions were used to reduce computing time.

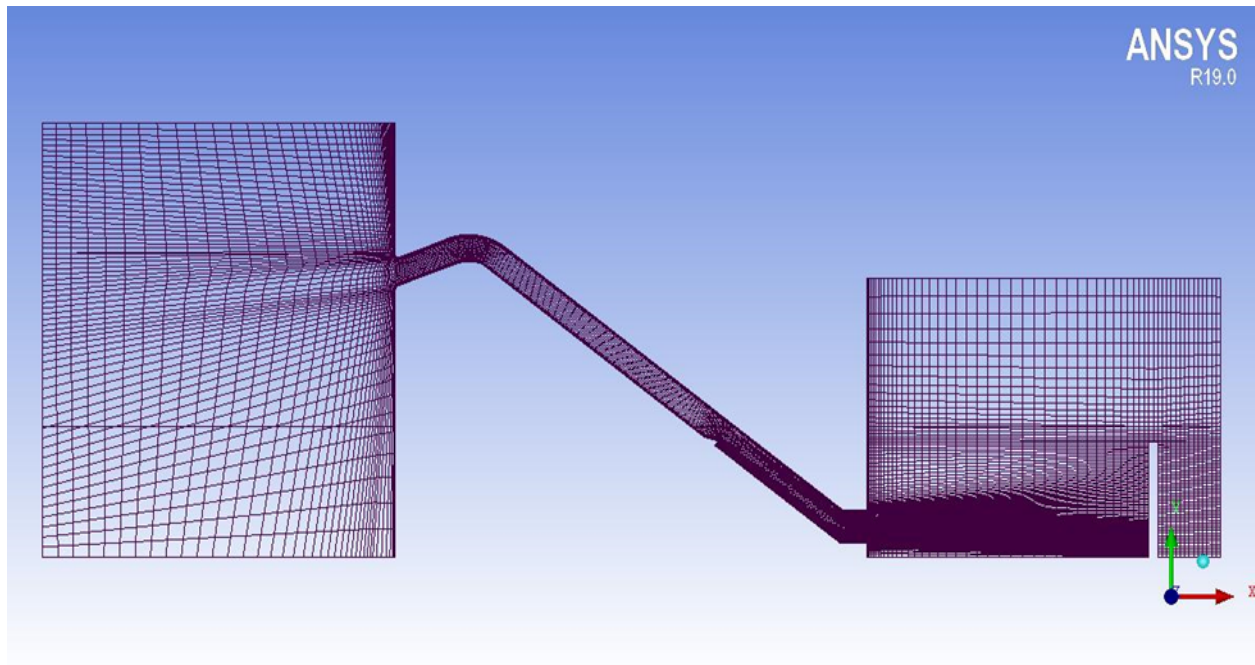


Figure 4-4. Sectional view of finite volume mesh in the centre plane  $z = 0.0625$  m

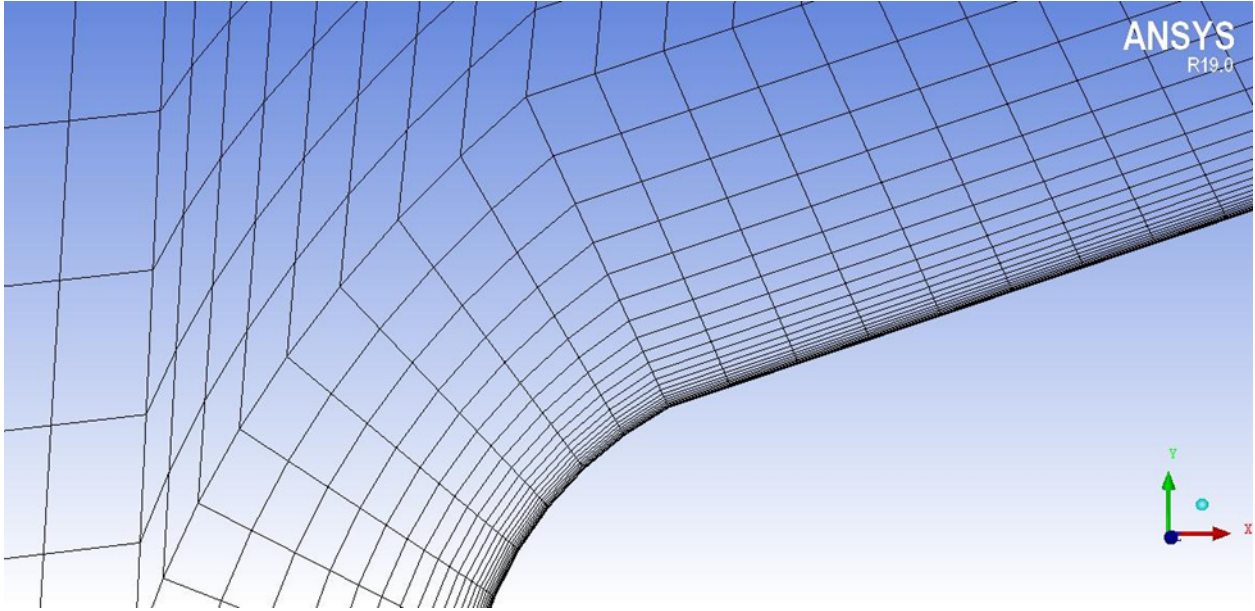


Figure 4-5. Sectional view of finite volume mesh, showing inflation near walls.

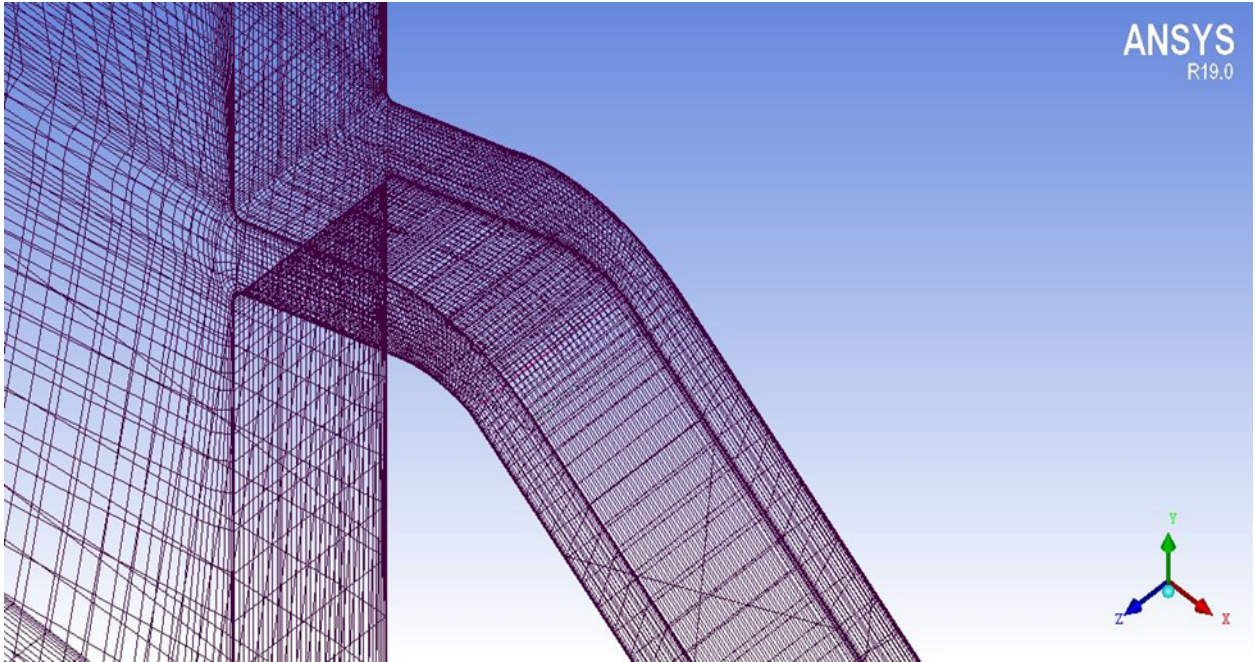


Figure 4-6. 3-D view of finite volume mesh.

## 4.5. Simulation setup

### 4.4.1 Boundary conditions

In flow simulations, it is important to ensure that the boundary conditions accurately represent the real prototype and its physical conditions. In addition, a set of boundary conditions are required to solve the equations (Launder and Spalding, 1972). The CFD model domain had a shorter the downstream flume, compared to the physical model, in order to save computing time and decrease the computer storage. The model domain (Figure 4.3) had the following six boundaries: 1) an inlet at its upstream end; 2) an outlet at its downstream end; 3) an outlet at its bottom downstream of the tailgate; 4) an air surface at the top of the upstream tank; 5) an air surface at the top of the downstream flume section; 6) solid walls. Conditions imposed at these boundaries were as follows:

- 1) The inlet consisted of a lower portion and an upper portion, divided at the water level. At the lower portion, a depth-averaged water velocity  $U$  was specified. The upper portion was treated as a pressure inlet with  $P = 0$ . The water level or equivalently the water depth was specified; the water level was specified as  $H_1 = 96.4$  cm.
- 2) The outlet at the downstream end was divided into a lower and an upper portion by the water level, like the inlet. Both portions were treated as a pressure outlet with  $P = 0$ . The water level was specified as  $H_2 = 61.19$  cm.
- 3) The outlet at the bottom was a pressure out with  $P = 0$ .
- 4) The air surface on the upstream side was treated as a pressure inlet with  $P = 0$ .
- 5) The air surface on the downstream side was treated as a pressure outlet with  $P = 0$ .
- 6) At solid walls the velocity components were zero.

Note that the purpose of these simulations was to predict the flow over the siphon with different water levels. It is appropriate to treat all the air boundaries as a pressure boundary with the gauge pressure equal to zero (atmospheric pressure). At the inlet, the water velocities were calculated from the discharges in available laboratory experiments.

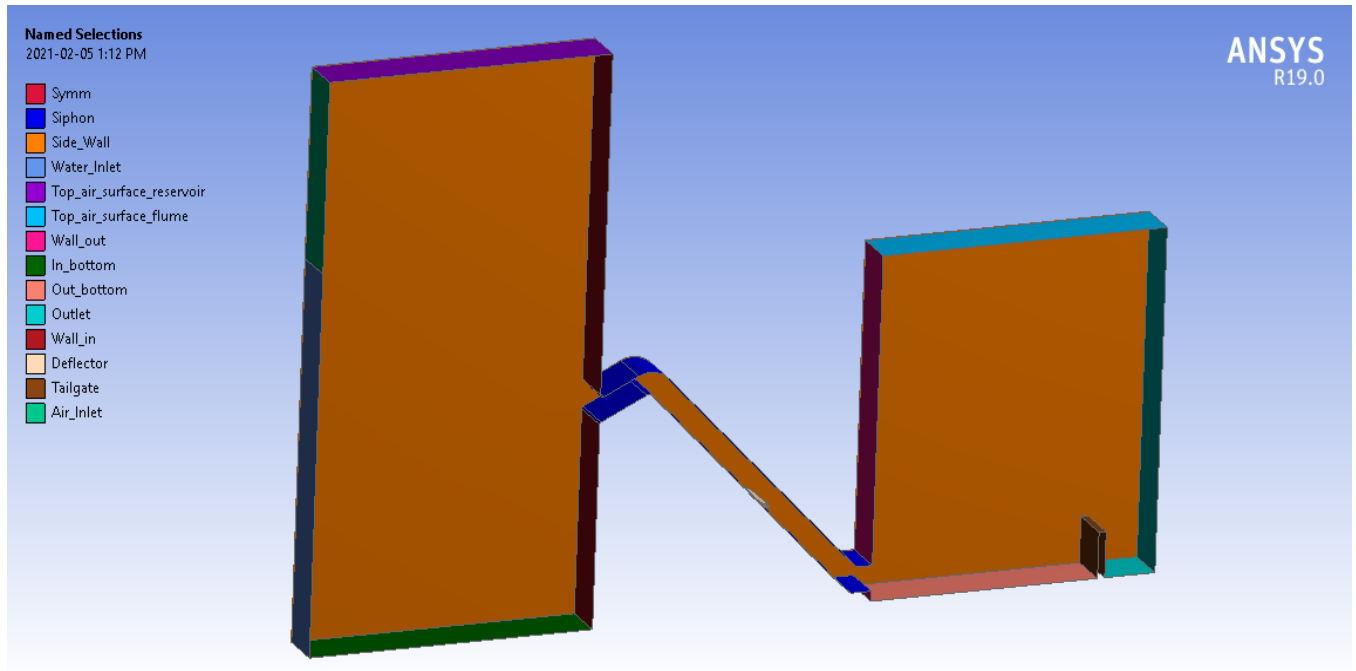


Figure 4-7. Geometry of the siphon spillway model domain, and three types of boundaries: 1) inlet; 2) outlet; 3) solid walls.

#### 4.5.2 Discretization

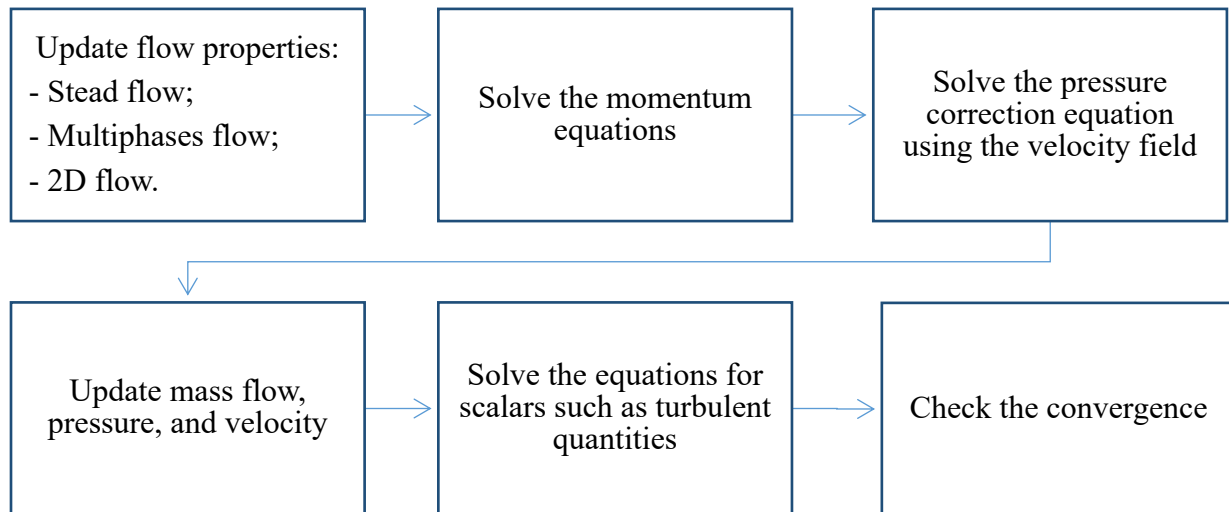
All the simulations were carried out with the use of the ANSYS Fluent 19.2 CFD code. The 3-D RANS equations were solved using the finite volume method for unsteady, incompressible flow. In this study, for pressure and velocity coupling in the calculations using time steps, coupled scheme was used. First order scheme was used for time approximation. For the momentum equations we used the second order upwind scheme. The body force weighted interpolation was utilized for pressure. The compressive scheme was used for VOF method.

#### 4.5.3 Initialization

At model time  $t = 0$ , simulations (Table 4.1) commenced from a state of rest with zero velocities ( $U_1 = U_2 = U_3 = 0$ ) everywhere in the model domain and standard atmospheric pressure or zero relative pressure ( $P = 0$ ) at boundaries exposed to the atmosphere. Also, the initial flow started from velocity inlet boundary at the water tank inlet to allow stable conditions before the flow entered the siphon section.

#### 4.5.4 Solution procedure

All the simulations were carried out with the use of the ANSYS Fluent CFD code based on the finite volume method (FVM). This method discretized governing differential equations and converted them into a system of algebraic equations. Accordingly, the momentum equations were approximated with the use of the second order upwind scheme and first order scheme was used for time approximation. In general, the pressure-based coupled algorithm was used to solve the equations for the velocity and pressure fields. In pressure-based flow solver, the continuity and momentum equations are coupled to derive a pressure correction equation. The momentum equations and the pressure correction equation are typically solved consecutively. The segregated algorithm of the solution is as follows:



For each run, it was necessary to initialize the model variables. The pressure was atmospheric pressure condition and the solution domain was partly filled with water. To allow stable condition of the computations, flows started from the model inlet boundary which is far enough from the spillway crest.

#### 4.5.5 Solution accuracy

To achieve accurate results, several steps were taken. First, a suitable discretization method (the finite volume method) was used. Also, the flow is computed as a transient flow and the model

equations are solved using iteration methods. The accuracy of the numerical solutions of flow variables to the RANS momentum and continuity equations as well as to the turbulence closure equations can be checked by monitoring the differences of solutions from successive iterations. At a given time step, zero differences mean that the solutions after a certain number of iterations have satisfied exactly the model equations mentioned above. However, it is not really possible achieve zero differences, and there is no need to do so. The difference between successive solution estimates is known as convergence errors. This study set the convergence criterion to  $10^{-6}$  for different flow variables. The smaller the convergence criterion, the more the iterations, which it will take per time step to achieve numerical convergence. With this small value ( $10^{-6}$ ) of the convergence error, the solution is converging in very slow rate. The solution no longer changes with additional iterations. To achieve a fast convergence, one should divide the domain with a suitable mesh according to the gradients of the variables in different regions. Also, the grid sensitivity or grid independence were checked. The grid independence was checked by using a coarse grid with a cell size of 4 mm and finer grid whose cells dimensions were half as those of the final grid cell size (or 2 mm).

Table 4-1 The grid resolutions and initial conditions for five model runs. the purpose of these runs was to confirm the independence of numerical results on mesh configuration and to evaluate the suitability of turbulence closure models.

Run	Mesh size	Time step size	Turbulence closure	Initial water level (m) at t = 0	
ID	Dx (mm)	t (s)		Upstream tank	Downstream flume
RN2G	2	0.001	RNG k-e	0.964	0.6119
RN3G	3	0.001	RNG k-e	0.964	0.6119
RN4G	4	0.001	RNG k-e	0.964	0.6119
RN4	4	0.001	RNG k-e	0.964	0.6119
SK4	4	0.001	Standard k-e	0.964	0.6119
RL4	4	0.001	Realizable k-e	0.964	0.6119

## 4.6. Results

### 4.6.1 Independence of model results on mesh configurations

Three runs: RN2G, RN3G and RN4G, were carried out to confirm the independence of numerical model results on mesh resolutions. The resolutions for RN2G, RN3G and RN4G were 2, 3 and 4 mm, respectively (Table 4.1). These three runs used the same turbulence closure model (the RNG  $k-\varepsilon$  model) and served as mesh sensitivity test. All the three meshes used inflation to allow refinement for near-wall regions (Figure 4.4). In Figure 4.8, there are small differences in the vertical profile of the longitudinal velocity component between RN2G, RN3G and RN4G. The results for the finer grid (2 mm) run were essentially the same as those for the grid size (4 mm) run. The results of the mesh sensitivity analysis show that the grid size 4 mm produced accurate results and incurred the shortest computing time. Therefore, a grid size of 4 mm was chosen as the mesh size for all other remaining runs.

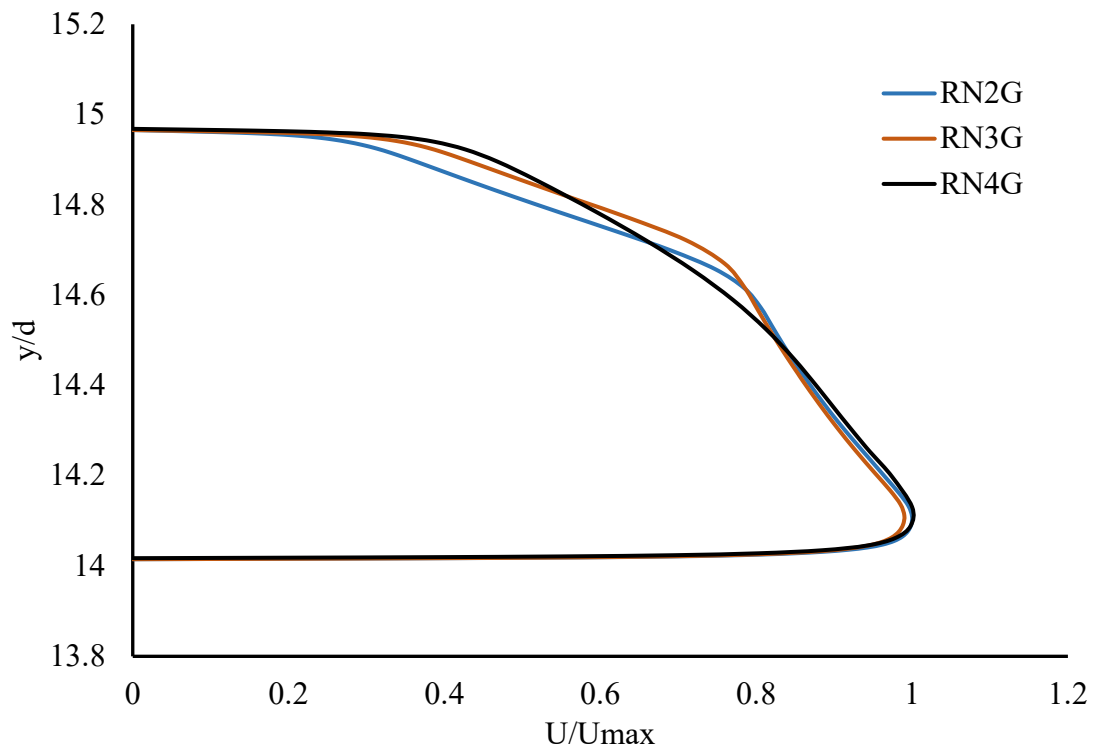


Figure 4-8 Vertical profiles of the longitudinal velocity component at the siphon crest section, showing values of  $U_1$  at different elevations above the crest for runs RN2G, RN3G and RN4G.

$U_{\max}$  is the maximum value of  $u$  at the section,  $d$  is the throat depth from the crest to the crown at the crest section, and  $d = 5.715$  cm.

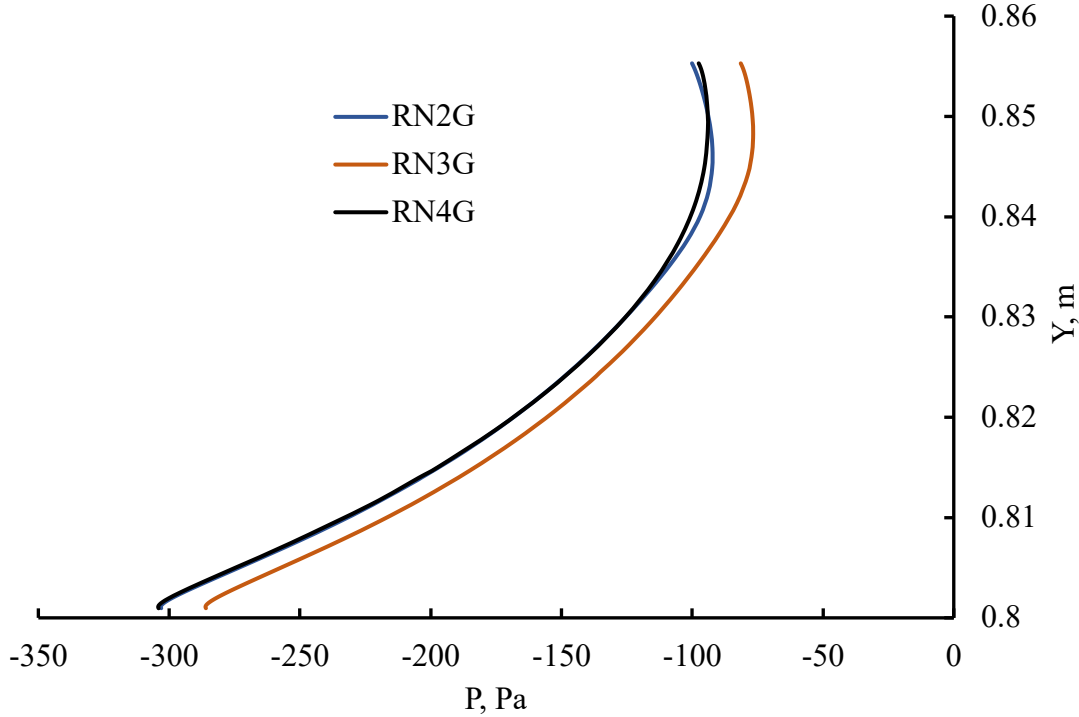


Figure 4-9. Vertical profiles of pressure  $P$  at the siphon crest section, showing values of  $P$  at different elevations above the crest for Runs RN2G, RN3G and RN4G. The numerical values of  $P$  are provided in a data sheet in Appendix A (Table A1).

Grid independence of numerical model results was also evaluated using pressure as another indicator. Figure 4-9 shows the variation of the pressure over the siphon crest for the three runs RN2G, RN3G and RN4G, with different grid sizes (2, 3 and 4 mm). The percentages of the difference in gauge pressure values between the three runs were determined. Table A2 in Appendix A gives a data sheet of the pressures plotted in Figure data. At a given location  $(x, y, z)$ , the relative error in percentage,  $\delta p$ , is defined as:

$$\delta p = \frac{P_4 - P_2}{P_2} \times 100 \quad (4.20)$$

where  $P_4$  and  $P_2$  are pressure values for Runs RN4G and RN2G, respectively.

The examples of data comparisons in Figures 4.8 and 4.9 demonstrate that the numerical solutions are consistent from the use of increasingly finer meshes. The average difference between the results of the three runs is very small (-0.064). This assured that the 4 mm grid size that was chosen allowed accurate results with little information of flow details missing.

#### 4.6.2 Evaluation of the suitability of models for turbulence closure

Three different turbulence closure models (RNG k- $\epsilon$  model, Standard k- $\epsilon$  model, and Realizable k- $\epsilon$  model) were tested in the study. The simulation results based on these models for the water flow through the siphon under submerged flow conditions are compared.

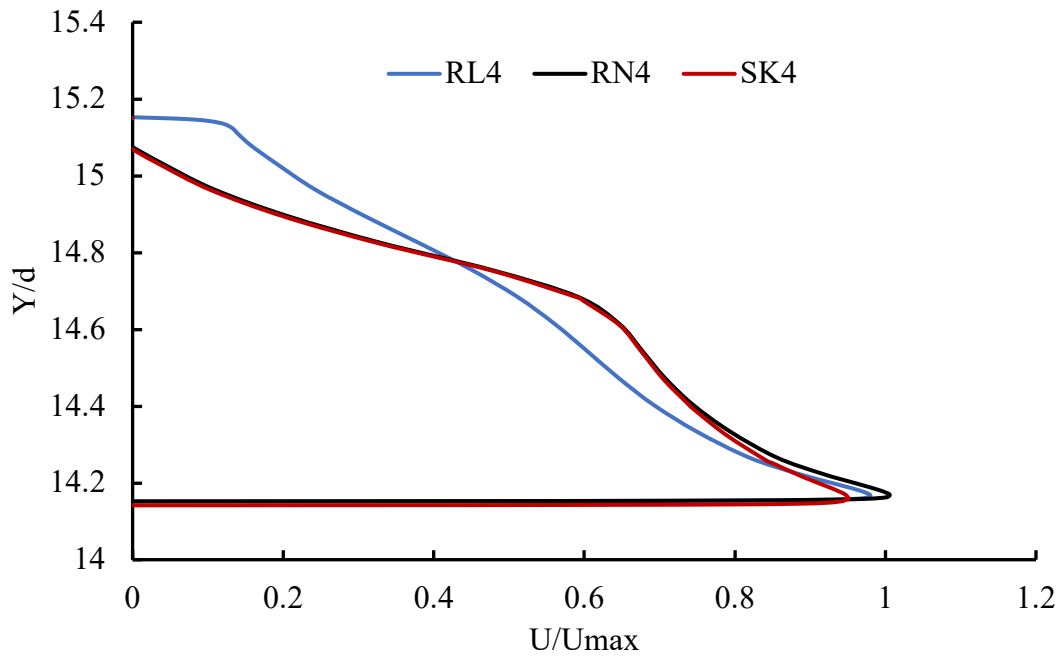


Figure 4-10. Vertical profiles of the longitudinal velocity component at the siphon crest section, showing values of  $U_1$  at different elevations above the crest for Runs SK4, RL4 and RN4 (Table 4.3).  $U_{max}$  is the maximum value of  $U$  at the section,  $d$  is the distance from the crest to the crown at the crest section. The numerical values of  $U$  are provided in a data sheet in Appendix A (Table A2).

In Figure 4.10, a comparison in velocity profile between the three turbulence models showed that the Standard k- $\epsilon$  model predicted the largest values of the longitudinal velocity component from the crest to the crown, and the most rapid changes in the velocity in the vicinity of the crest

and crown. These rapid changes can be non-physical and may have resulted from the inadequacy of the model for the near-wall regions. The Realizable  $k-\epsilon$  model produced the smallest values of the velocity, and the profile was smooth near the crest and the crown. The RNG  $k-\epsilon$  model predicted values of the velocity in between, and the profile was smooth near the crest and the crown. The middle portion of the profile closely resembled the solution from Dressler (1978) theory for inviscid flow past over a circular weir. For this reason, the RNG  $k-\epsilon$  model is considered to be more suitable for modelling siphon flow.

In Figure 4.11, pressure profiles from Runs RL4, RN4 and SK4, using the three turbulence models (Realizable  $k-\epsilon$  model, RNG  $k-\epsilon$  model, and the standard  $k-\epsilon$  model), are compared. The three profiles all showed negative pressure values close to the crest, as expected. The pressures dropped with distance downward from the crown. The realizable  $k-\epsilon$  model predicted the least drops in pressure at all depth. The Standard  $k-\epsilon$  predicted the largest drops. These predicted drops corresponded to the predictions of the velocity shown in Figure 4-10. The RNG  $k-\epsilon$  model is arguably the best choice of the three for simulations of flow over the siphon crest.

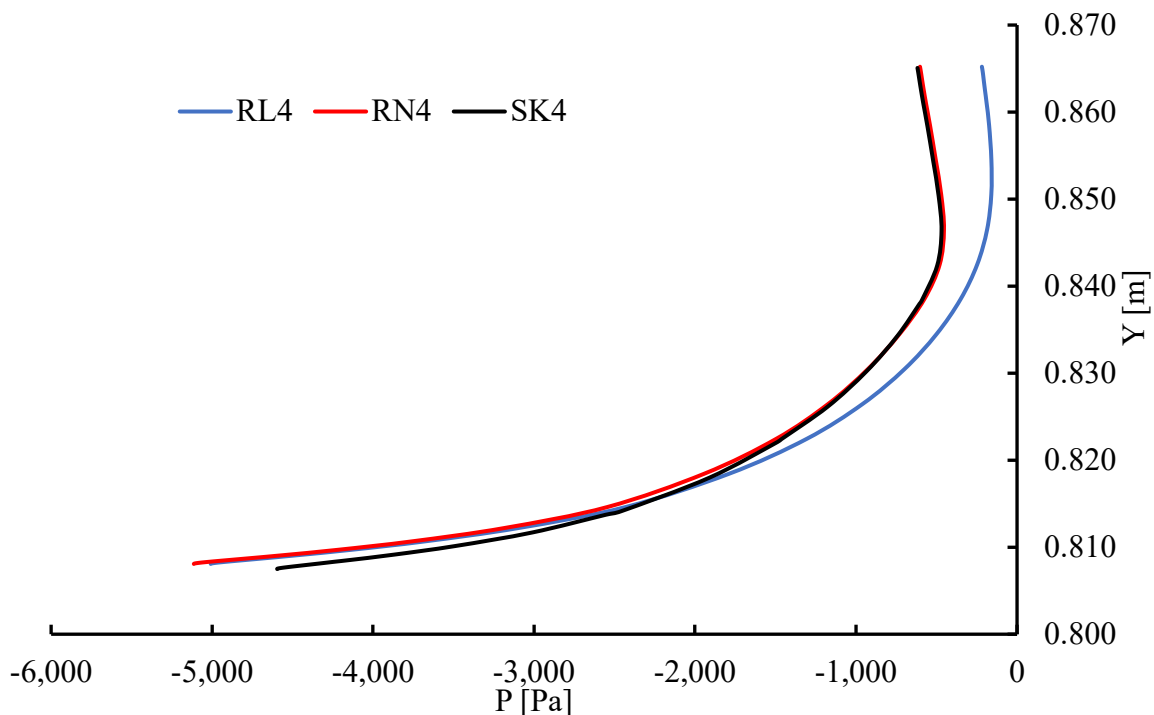


Figure 4-11. Vertical profiles of pressure  $P$  at the crest section, showing values of  $P$  at different elevations above the crest for Runs SK4, RL4 and RN4. The numerical values of  $U$  are provided in a data sheet in Appendix A (Table A3).

### 4.6.3 Velocity distribution

Velocity vectors of the flow through the siphon in the center plane are illustrated in Figure 4.12. In the upstream reservoir, flow vectors had weak magnitudes. The flow was subcritical. For most part of the reservoir, the flow was two-dimensional. As the flow approached the siphon, vectors converged and pointed smoothly toward the entrance of the siphon. At the entrance, the velocity vectors were contracted toward the flow path. The model time is  $t = 20.8$  s for the results presented hereafter. At the crest, velocity vectors were forced to flow in the extrados direction under the influence of centrifugal forces. The flow had high velocities above the crest and low velocities near the crown. The flow displayed converging streamlines upon approaching the crest section. Further downstream at the deflector, the flow was forced to tilt towards the upper surface of the lower leg of the siphon. The flow tilting by the deflector would prevent air from entering the siphon conduit even if the downstream water level were high enough to cause submerged exit conditions.

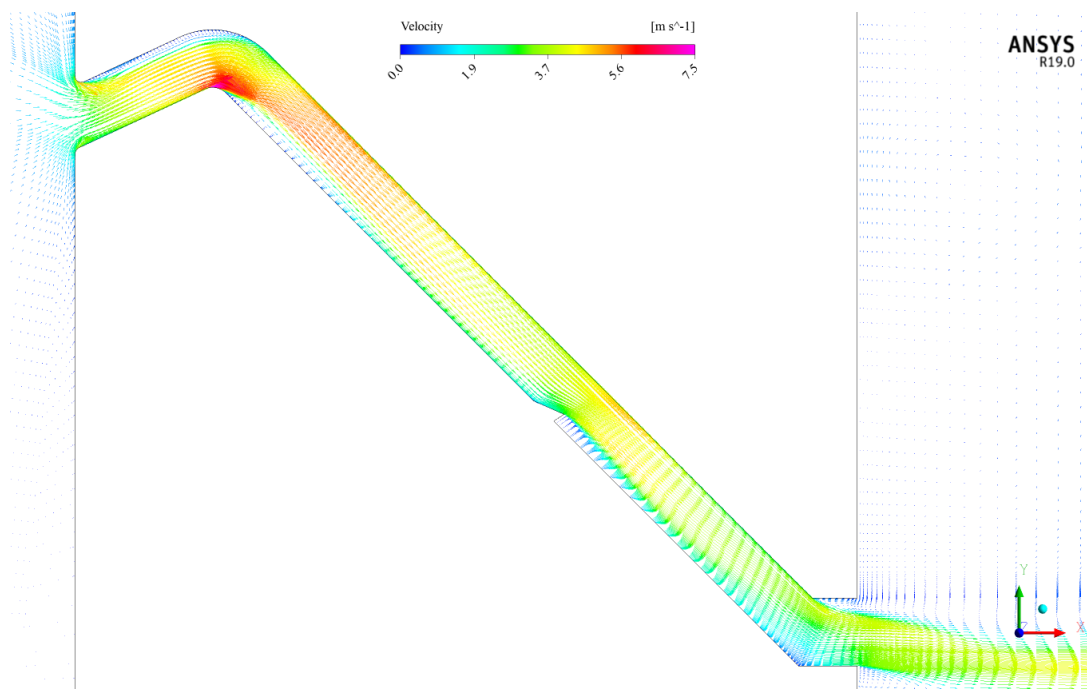


Figure 4-12. Distribution of velocity vectors in the centre plane  $z = 0.125$  m for Run RN4. This plane is assumed to be a plane of symmetry.

The velocity vectors clearly showed major flow separation in two zones along the model siphon. The first separation zone was along the upper surface of the upper leg between the siphon entrance and crown. There was an elongated eddy with a streamwise length of approximately times the siphon throat depth (or  $4d$ ). The second separation zone was along the lower surface of the lower leg just downstream of the siphon crest. There existed an elongated eddy with a length of  $3d$  (Figure 4-12).

In the exit portion of the siphon conduit, the flow along the upper surface reversed direction. Just outside the exit in the downward step, the flow rotated clockwise. The flow separation zones along the upper surface and in the downward step corner had a length of 2.5 cm and 7 cm, respectively (Figure 4-13). These findings showed how the geometry of the exit can strongly affect the efficiency of siphon flow.

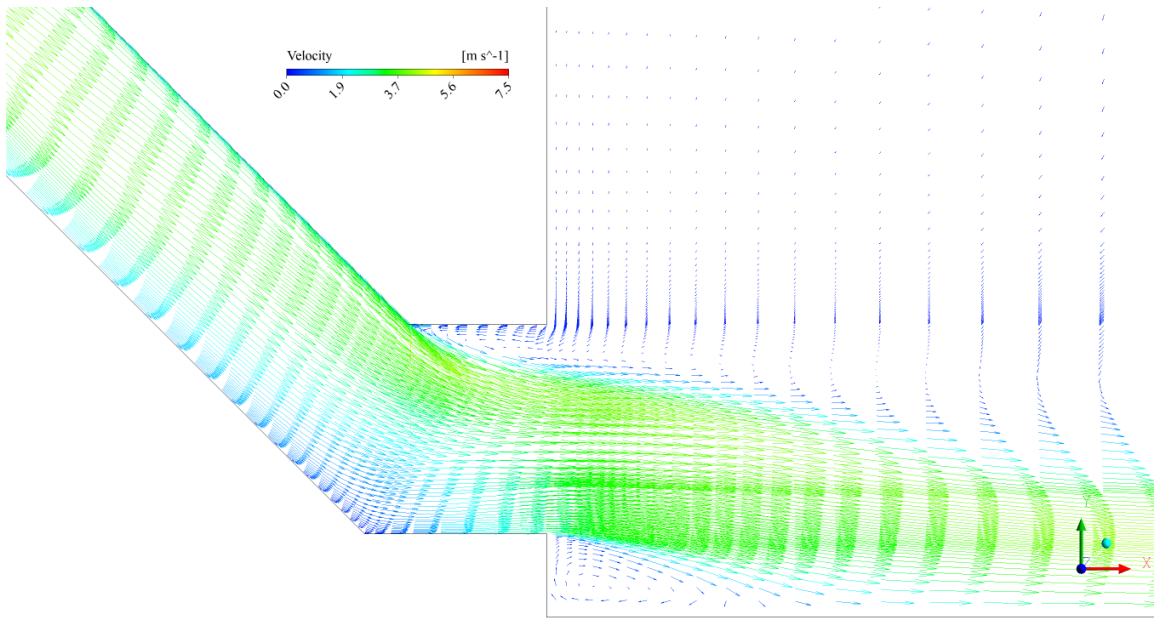


Figure 4-13. Velocity vectors at the conduit exit in the center plane  $z = 0.125$  m for Run RN4.

To show spatially varying flow structures in the crest region, values of the longitudinal velocity component  $U$  were extracted from the results for Run RN4 for nice vertical lines shown in Figure 4.14. Three of the lines are located at a short distance upstream of the crest, three at the crest, and the remaining three at a short distance downstream of the crest. In the lateral direction (the  $z$  direction), three of the lines are in the centre plane, and the remaining six are closes to the sidewall. The nine vertical profiles of  $U$  are plotted in Figures 4.14, 4.15 and 4.16.

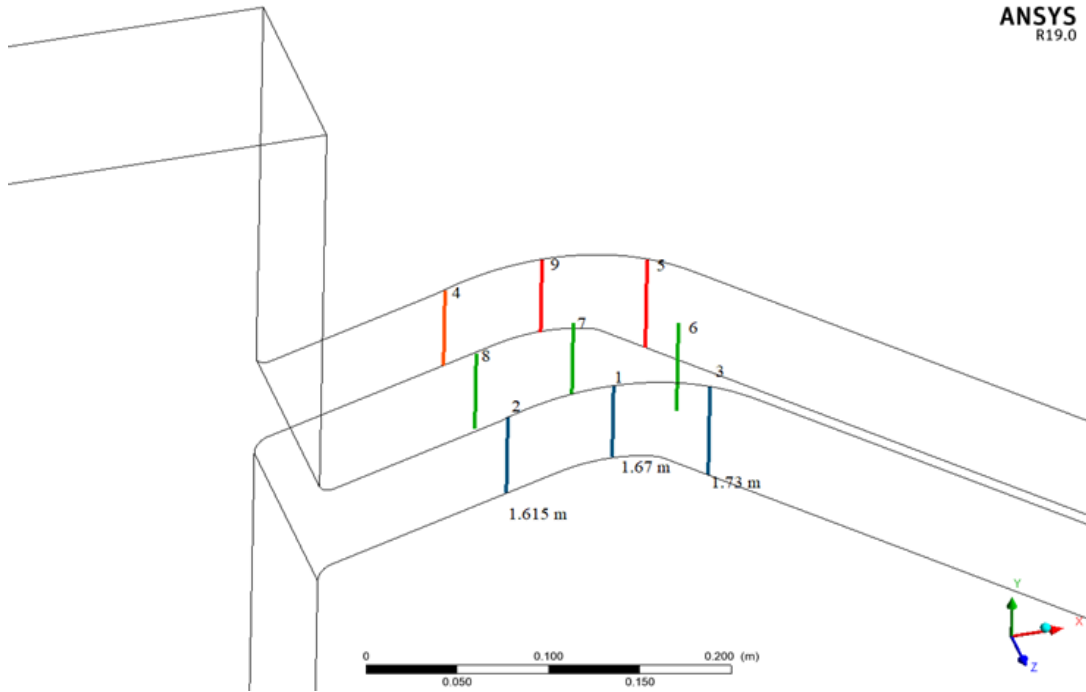
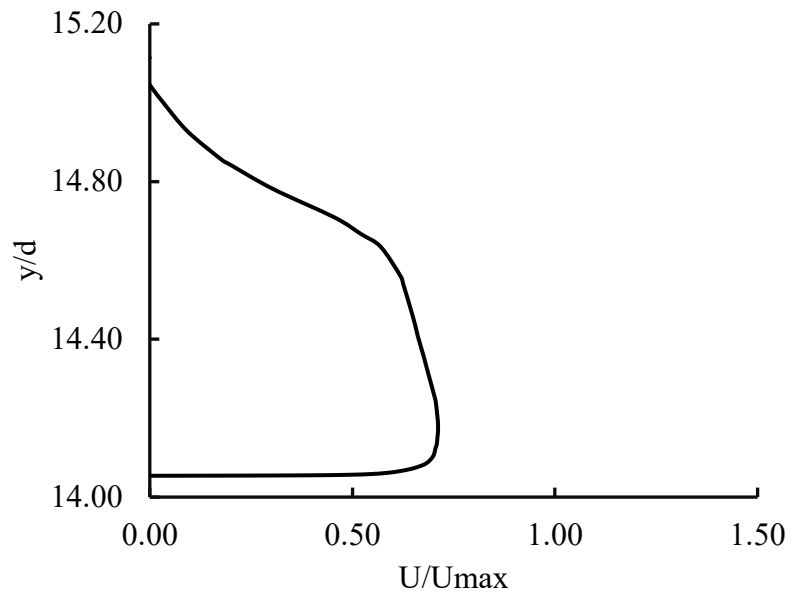
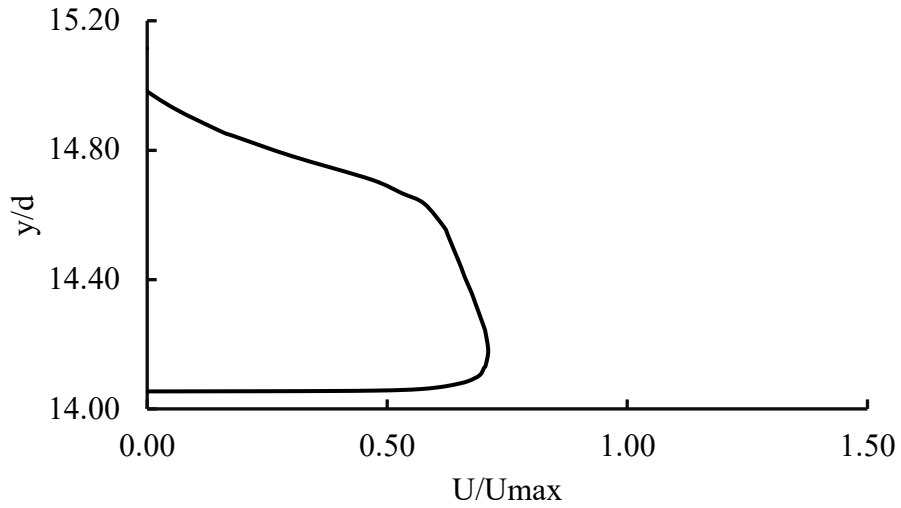


Figure 4-14. The locations of nine selected vertical lines along which distributions of the longitudinal velocity component are to be plotted.

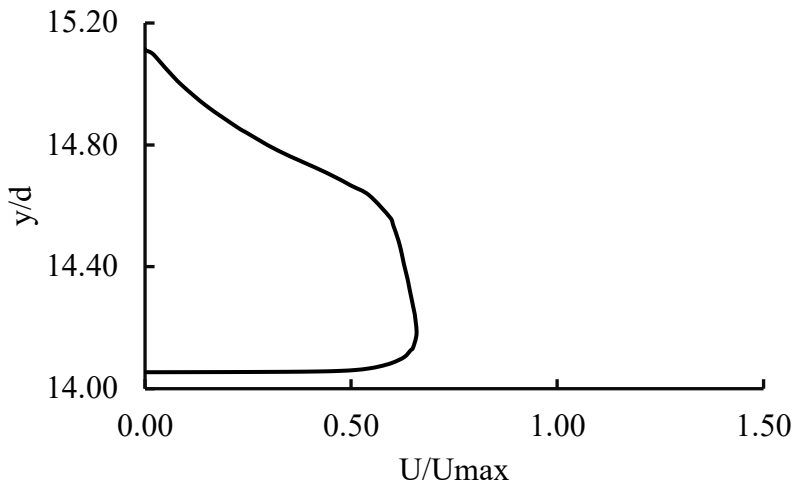


(Figure 4.15 continued)

(a)

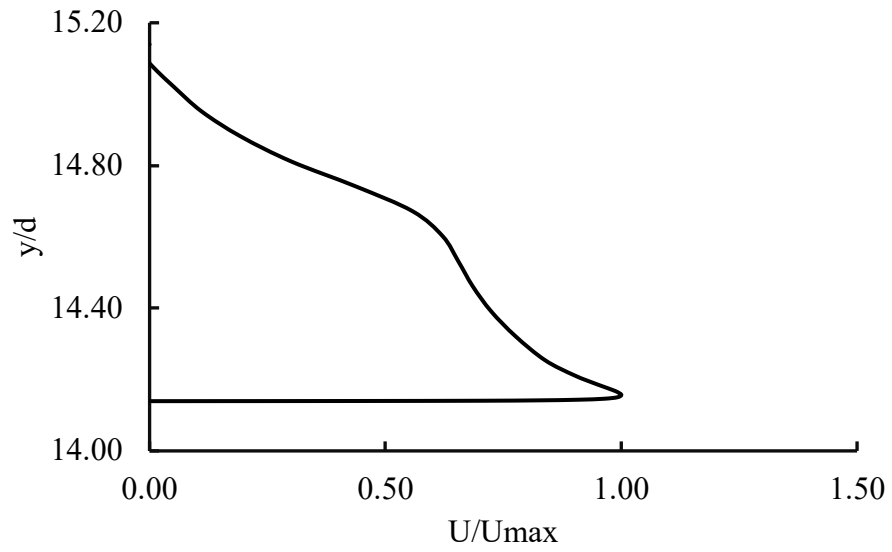


(b)

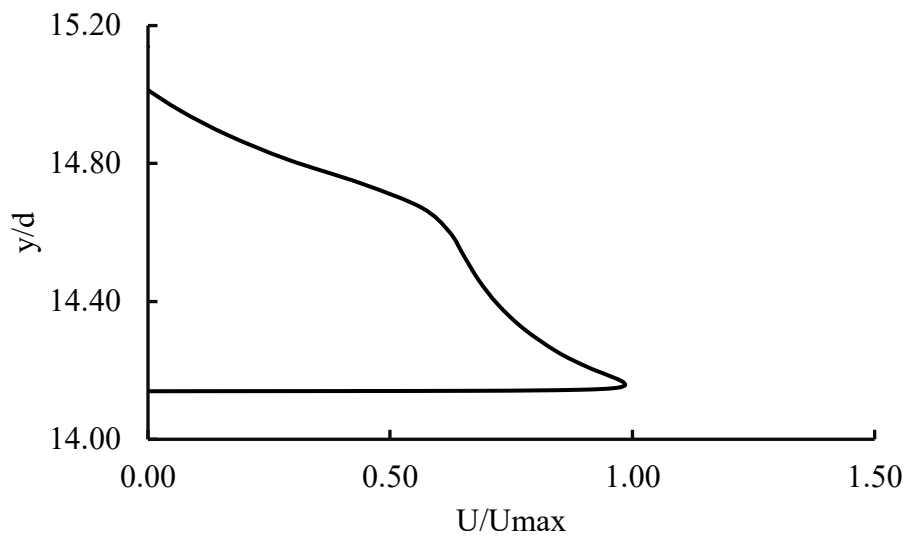


(c)

Figure 4-15 Vertical profiles of the longitudinal velocity component in the crest region, showing values of  $u$  for run RN4 (Table A4) at different elevations above the lower surface of the siphon conduit. The streamwise and lateral coordinates are: (a)  $(x, z) = (1.615, 0.125)$  m, which is the plane of symmetry; (b)  $(x, z) = (1.615, 0.0625)$  m, which is at the middle between the plane of symmetry and the sidewall; (c)  $(x, z) = (1.615, 0.005)$  m, which is near the sidewall. The three locations are labelled as vertical lines 2, 8 and 4 in Figure 4.13.

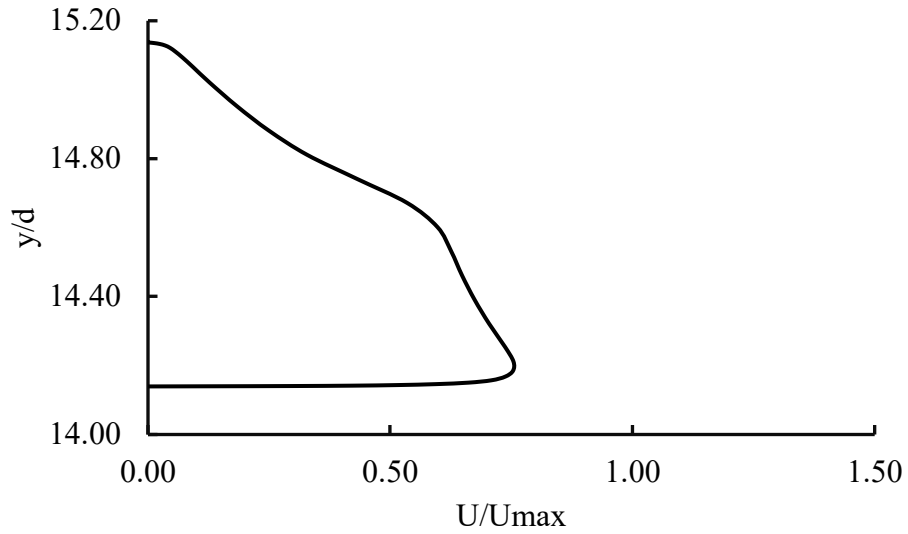


(a)



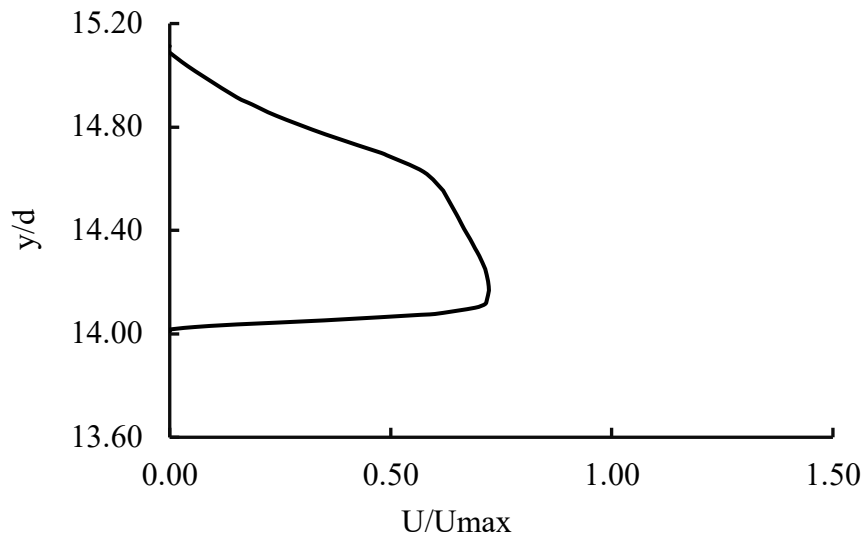
(b)

(Figure 4.16 continued)



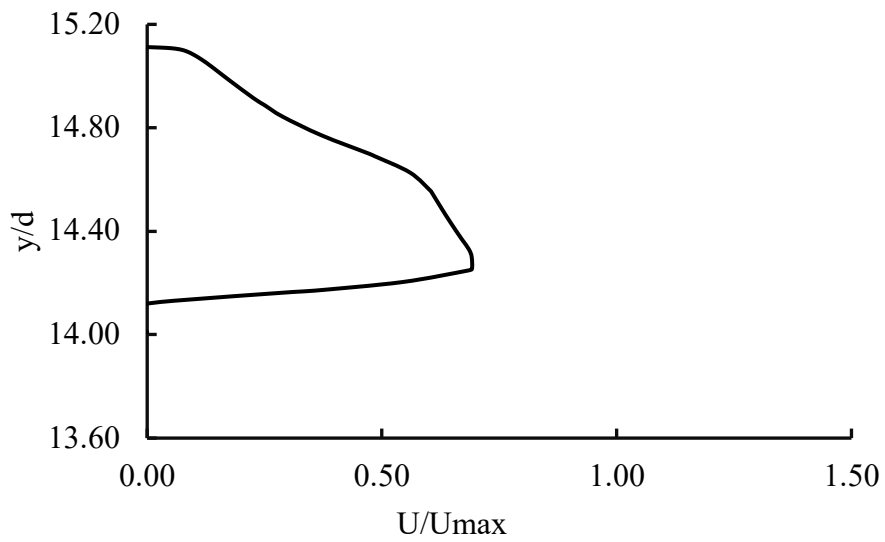
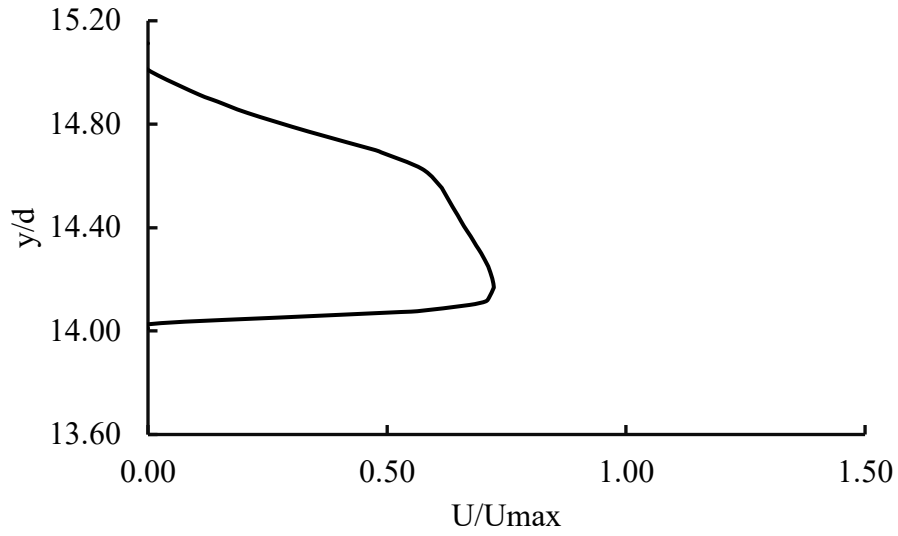
(c)

Figure 4-16. Vertical profiles of the longitudinal velocity component in the crest region, showing values of  $U$  for simulation RN4 (Table A5) at different elevations above the lower surface of the siphon conduit. The streamwise and lateral coordinates are: (a)  $(x, z) = (1.67, 0.125)$  m; (b)  $(x, z) = (1.67, 0.0625)$  m; (c)  $(x, z) = (1.67, 0.005)$  m. The three locations are labelled as vertical lines 1, 7 and 9 in Figure 4.13.



(a)

(Figure 4.17 continued)



(c)

Figure 4-17 Vertical profiles of the longitudinal velocity component in the crest region, showing values of  $U$  for simulation RN4 (Table A6) at different elevations above the lower surface of the siphon conduit. The streamwise and lateral coordinates are: (a)  $(x, z) = (1.73, 0.125)$  m; (b)  $(x, z) = (1.73, 0.0625)$  m; (c)  $(x, z) = (1.73, 0.005)$  m. The three locations are labelled as vertical lines 3, 6 and 5 in Figure 4.13.

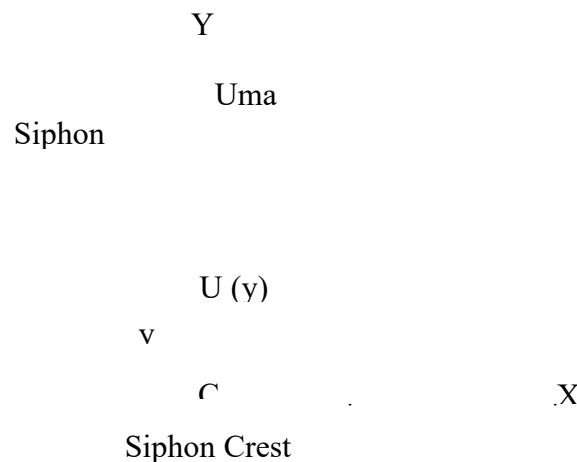
Dressler (1978) considered the flow of an ideal fluid past a cylinder based on the potential flow theory and obtained an analytical expression of  $U$  at the crest section as a function of vertical distance from the crest. Ramamurthy and Vo (1993) applied the theory to the flow over a circular weir and derived the following profile.

$$\frac{U}{U_{max}} = \frac{1}{1 + (y - y_c)/R_i} \quad (4. 21)$$

where  $U_{max}$  is the maximum value of velocity  $U$ ,  $y_c$  is the  $y$  coordinate of the crest, and  $R_i$  is the radius of the crest arc (Figure 3.5). The velocity  $U$  reaches the maximum at the crest ( $y = y_c$ ).

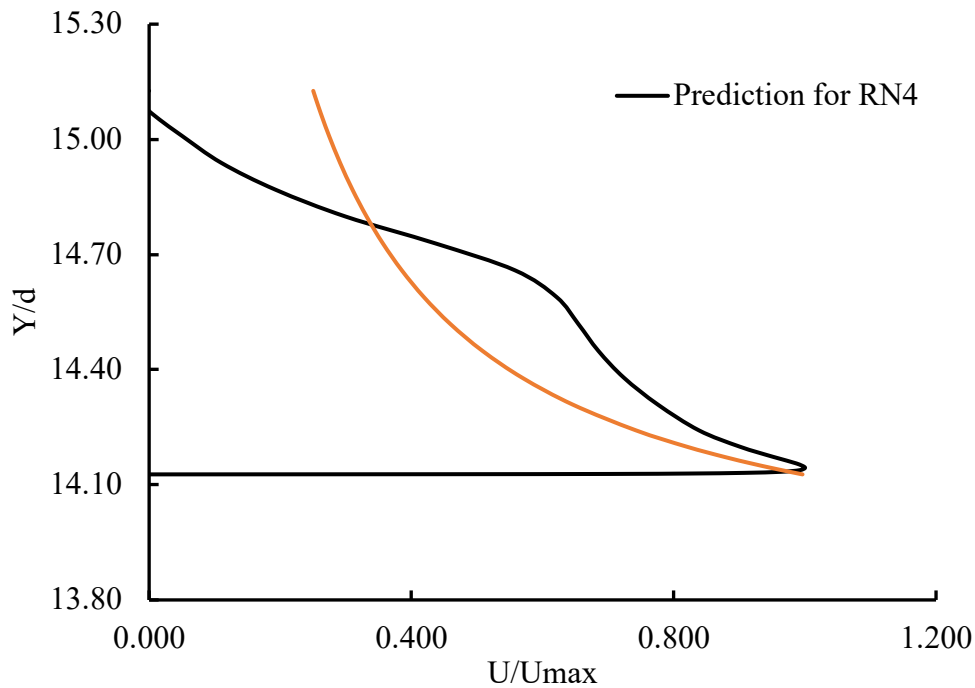
The profile is shown in Figure 4.18a

In Figure 4.18, the velocity profiles at the crest (calculation points in Fig.4.13). The vertical axis is the ratio of the water depth above the crest ( $y$ ) to the siphon diameter ( $d$ ), and the horizontal axis is the velocity ( $U$ ) at the depth ( $y$ ) to the maximum velocity ( $U_{max}$ ). Above the crest, the velocity increases rapidly to reach the maximum value at the edge of the thin boundary layer of the depth  $\delta$  where  $\delta \ll d$ . Subsequently, the velocity decreases gradually until become a small value approaching zero at 99% of the total water depth approximately.



(a)

(Figure 4.18 continued)



(b)

Figure 4-18. Vertical profiles of the longitudinal velocity  $U$  at the crest: (a) potential flow solution from Dressler (1978); (b) numerical solution from Run RN4 (Table A8), in comparison to the potential flow solution.

The comparison in Figure 4.18b shows significant differences between the potential flow solution and the numerical solution in the boundary layer next to the crest as well as in the boundary layer next to the crown, as expected. In the boundary layers, the velocities decreased as it approached the solid walls. In the middle region bounded by the outer edges of the boundary layers, the two solutions showed similar profile shapes; the velocities were the maximum at the lower edge of the region and decreased steadily with distance upward. The assumptions made in potential flow are that the flow is a frictionless and irrotational flow. For this reason, the potential flow does not represent the turbulence and secondary flow in regions close to the solid boundaries such as the crest and the crown surfaces. However, the potential flow represents the flow in the middle region much better and close to the real flow conditions.

#### 4.6.4 The pressure distribution over the siphon crest

Figure 4.18 shows the variation of the pressure at the centreline of the siphon crest. In Figure 3.18, the horizontal axis indicates the pressure head,  $P/\gamma$ , and the vertical axis is the elevation normalised by the siphon throat depth  $y/d$ . The pressure near the crest surface is a negative pressure with a value of -16.57 mmHg approximately. The minimum pressure value where the velocity is the maximum is seen near the crest where it can decrease to reach the water vapour pressure where the cavitation can possibly occur at the prototype scale.

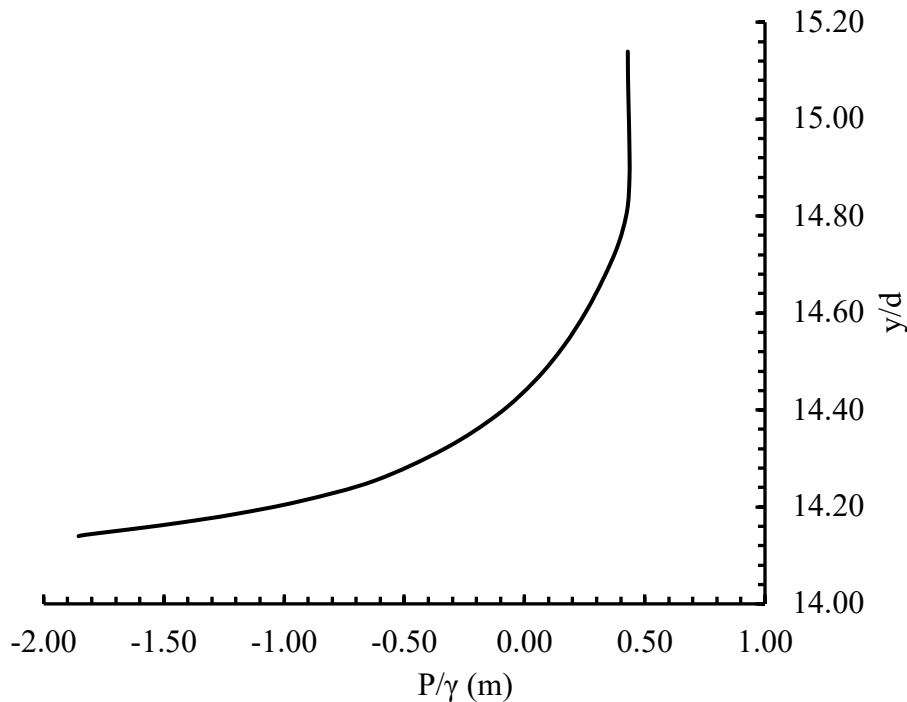
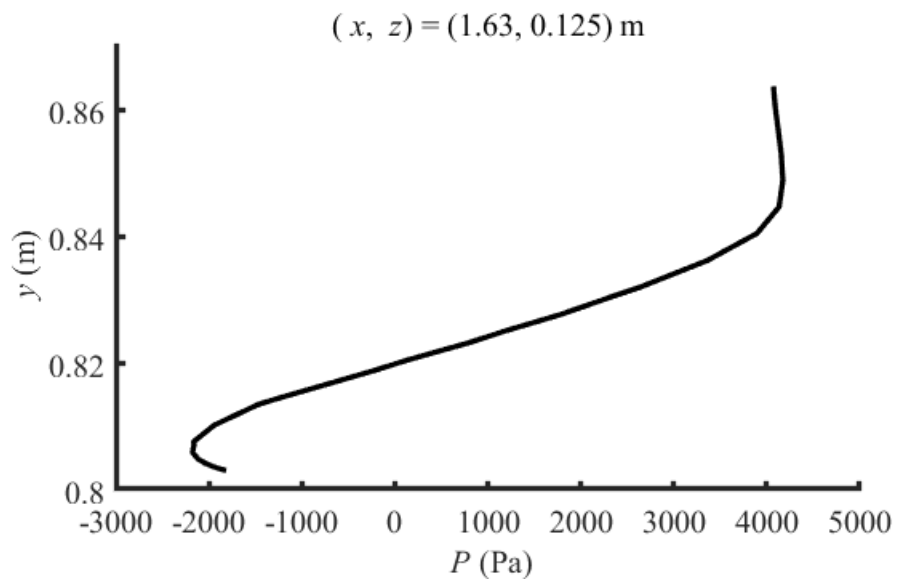
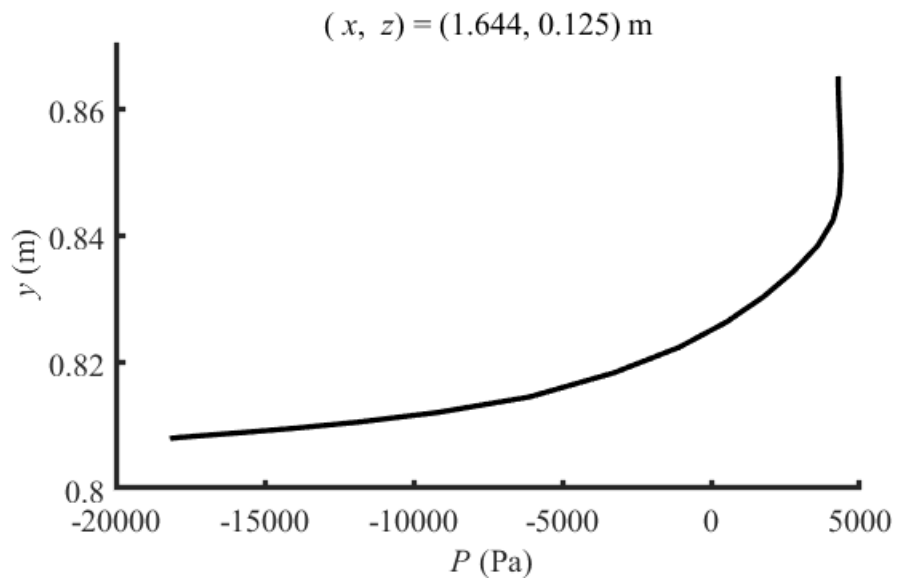


Figure 4-19. Vertical distributions of pressure from the siphon crest to the crown in the centre-line at  $x = 1.644$  m and  $z = 0.125$  m, for RN4 (Table A7).

As in the velocity distribution, the pressure distributions at various locations in the crest region obtained are plotted in Figure 4.19. The results showed that, because the flow was a curvilinear flow in the region of the siphon crest, the pressure was non-hydrostatic. This means that the actual pressure deviates from the hydrostatic distribution. With the velocity data as input, it is possible to calculate the pressure deviation using the correction method given in Chow (1959, p. 31). In other words, pressure data can be obtained from the numerical results of the velocity distribution.

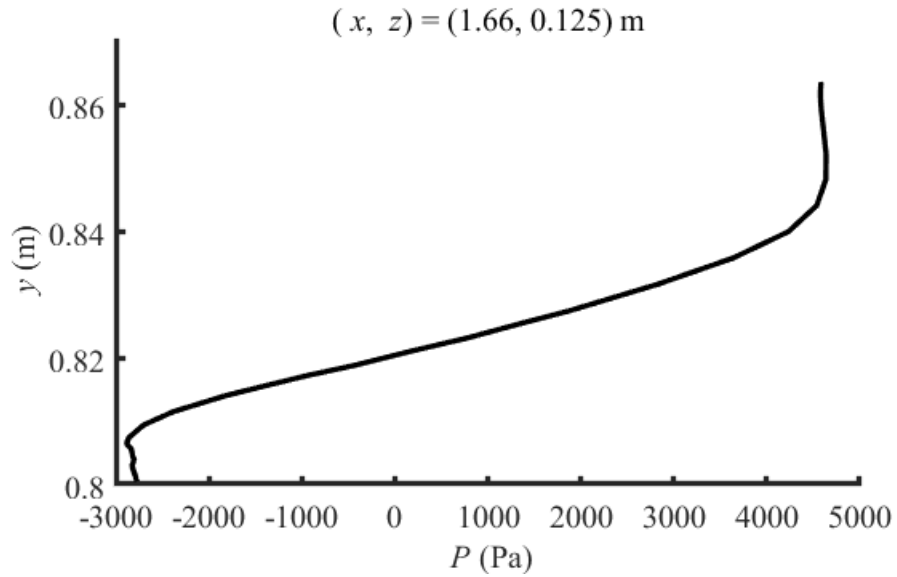


(a)



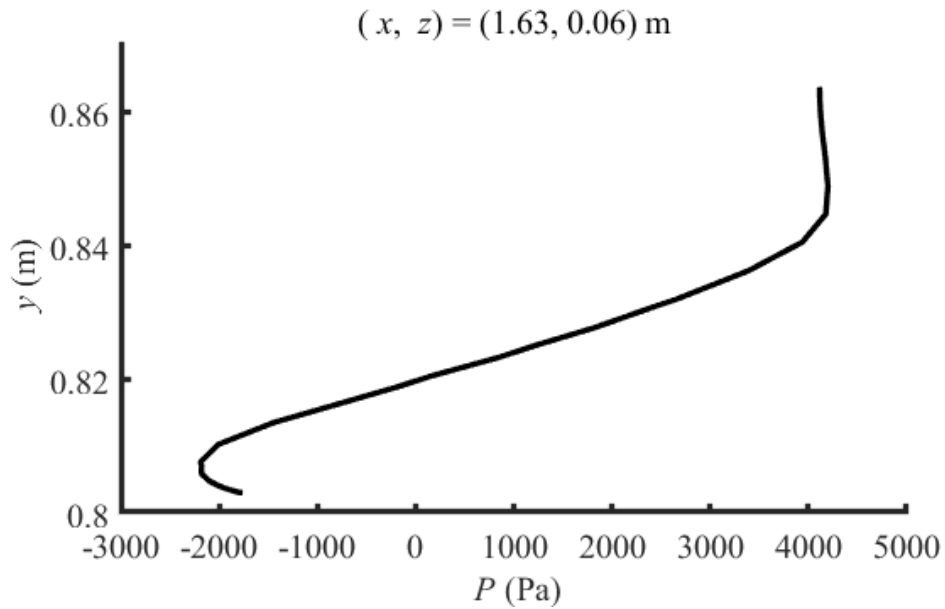
(b)

(Figure 4.20 continued)



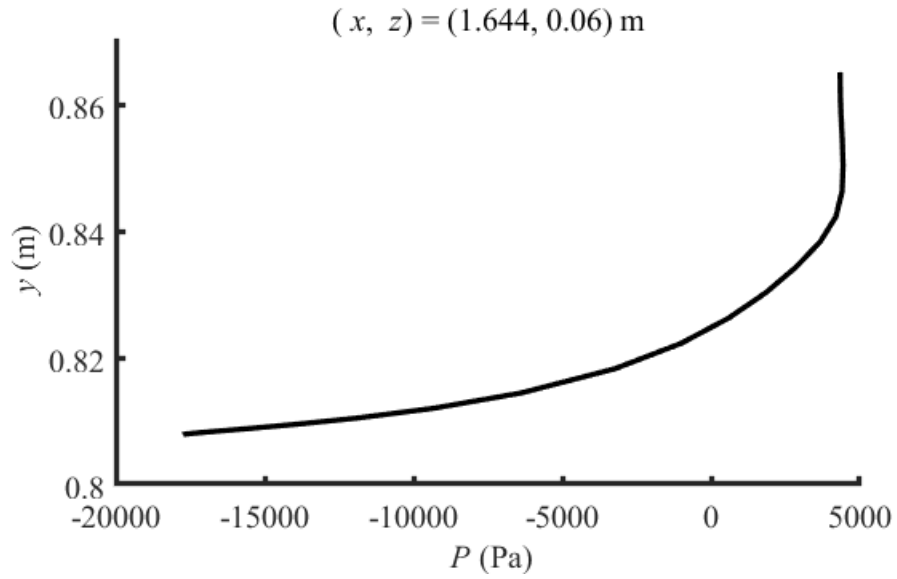
(c)

Figure 4-20. Vertical distributions of pressure for simulation RN4 in the centre-plane  $z = 0.125 \text{ m}$ . The longitudinal coordinate is: (a)  $x = 1.63 \text{ m}$ ; (b)  $x = 1.64 \text{ m}$ ; (c)  $x = 1.66 \text{ m}$ . The siphon crest and crown are located at  $x = 1.644 \text{ m}$ .

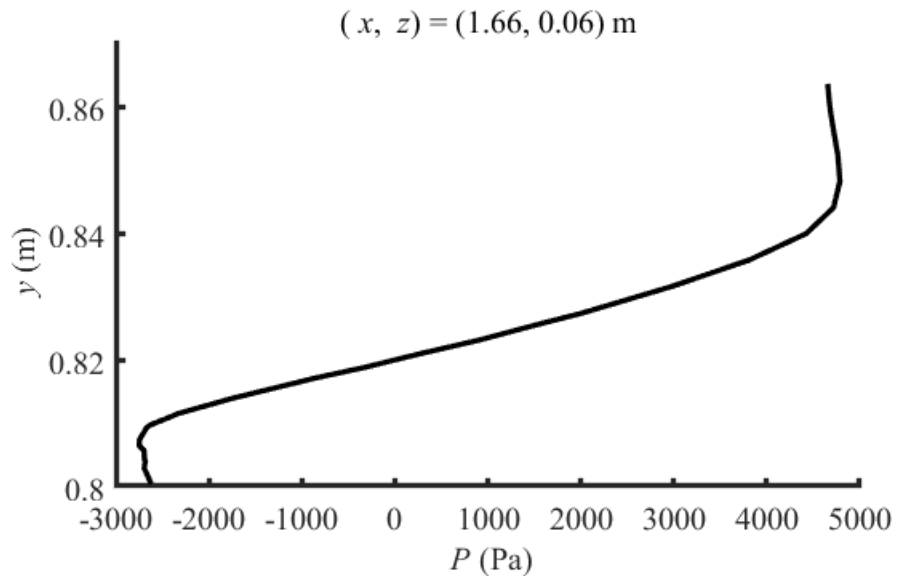


(a)

(Figure 4.21 continued)



(b)



(c)

Figure 4-21. Vertical distributions of pressure for simulation RN4 in the centreline plane  $z = 0.06$  m. The longitudinal coordinate is: (a)  $x = 1.63$  m; (b)  $x = 1.644$  m; (c)  $x = 1.66$  m. The siphon crest and crown are located at  $x = 1.644$  m.

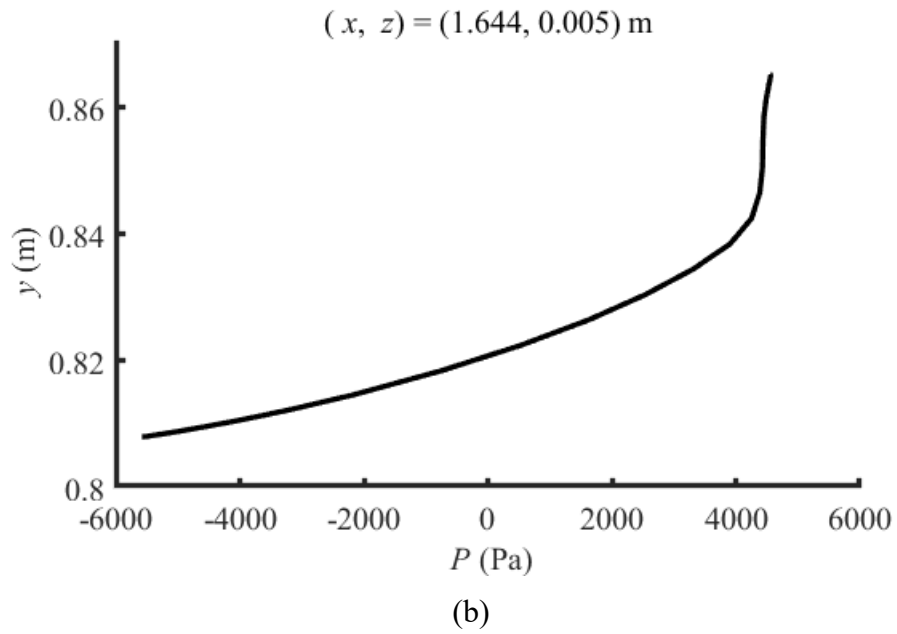
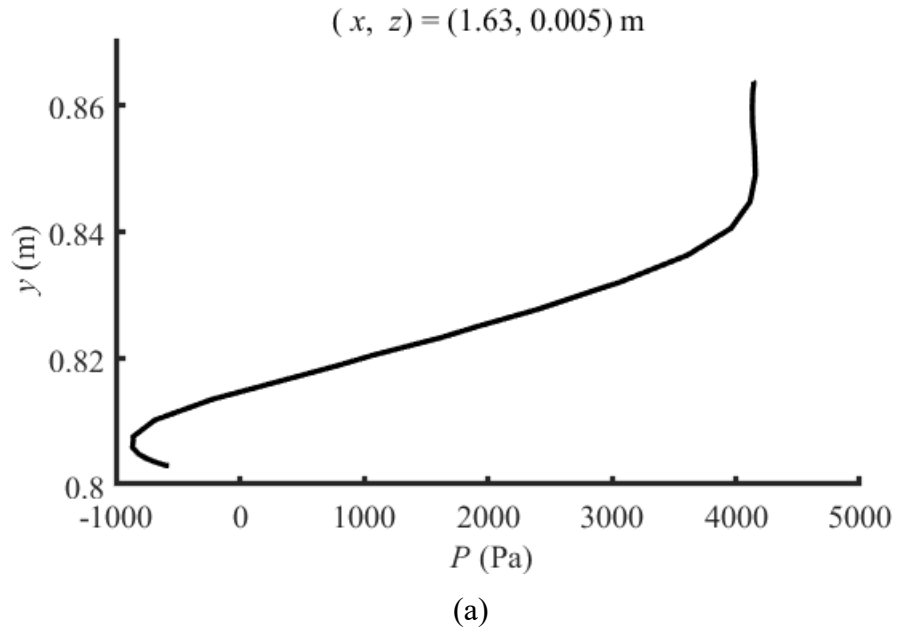


(Figure 4.22 continued)

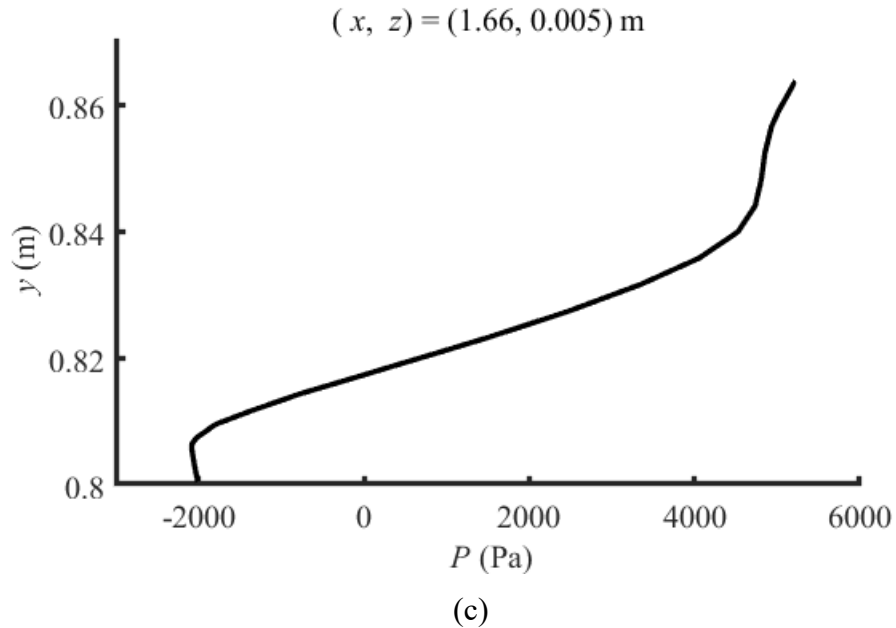


Figure 4-22. Vertical distributions of pressure for simulation RN4 in the centreline plane  $z = 0.005 \text{ m}$ . The longitudinal coordinate is: (a)  $x = 1.63 \text{ m}$ ; (b)  $x = 1.644 \text{ m}$ ; (c)  $x = 1.66 \text{ m}$ . The siphon crest and crown are located at  $x = 1.644 \text{ m}$ .

#### 4.6.5 Comparison of discharge coefficient $C_d$

The hydraulic conditions and siphon geometry for the model runs presented in this Chapter match those of the laboratory experiments presented in Chapter Three. This facilitates data comparisons.

The proper design of siphon spillways requires reliable estimates of the relationship between discharge and the difference in water level between the upstream and downstream sides. Such relationship involves a discharge coefficient  $C_d$ . This is a key parameter for the design of functional siphon spillways. The purpose of this section is to investigate the discharge coefficients under the conditions of submerged water flow at the exit of the siphon conduit.

Figure 4.22 compares the predicted results of  $C_d$  from this chapter with those from Tadayon and Ramamurthy (2013) as well as with the experimental results from the previous chapter. The vertical axis shows the discharge coefficient, and the horizontal axis shows the ratio of the upstream and downstream water levels difference  $\Delta H$  to the siphon throat depth  $d$ . The results were nondimensionalized to allow a comparison in their simplest form. The data comparisons indicate that the predictions from this chapter are reasonable. At a higher driving head  $DH$ , the

viscous effect becomes weaker as the Reynolds number is larger, and the numerical predictions become very close to experimental results.

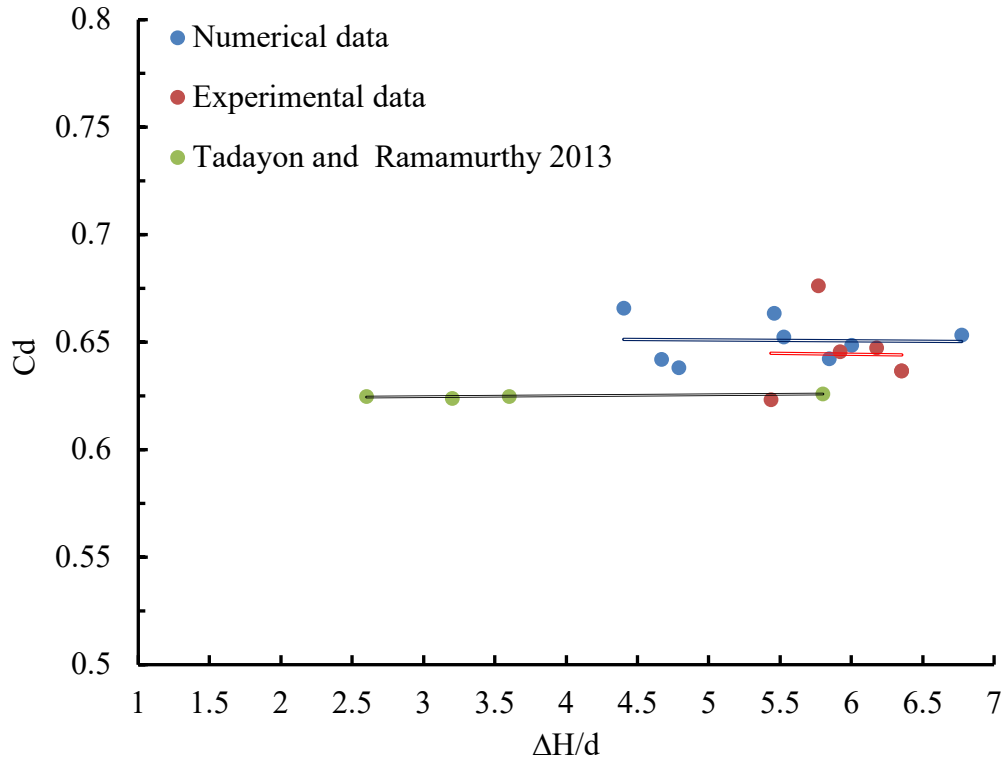


Figure 4-23. Variation of the discharge coefficient with normalized head

The discharge coefficient in the case of submerged exit is about 0.63 to 0.68. While the discharge coefficient of free flow condition (Tadayon and Ramamurthy, 2013) is between 0.62 and 0.63, and therefore, the trend in both cases are nearly same. The upstream reservoir water level, the downstream water level and the inlet velocity (see Section 4.5.1) for simulations of siphon spillway flow under six submerged conditions are presented in Table 4-2. These conditions match those of the six laboratory experiments covered in Chapter Three. The discharge coefficient obtained from the laboratory and CFD results can be applied directly to prototype siphon because  $C_d$  value is not sensitive to scale.

Table 4-2 Hydraulic conditions for numerical simulations and laboratory experiments of siphon flow.

Inlet flow rate	Upstream reservoir water level	Downstream reservoir water level	Submergence level	Dimensionless head	Discharge coefficient
q (m <sup>3</sup> /s)	H1 (m)	H2 (m)	H2/d	$\Delta H/d$	Cd
0.024	0.7428	0.3808	3.02	6.351	0.637
0.025	0.7352	0.4065	3.47	5.767	0.676
0.024	0.6966	0.3345	2.21	6.353	0.637
0.022	0.7475	0.4377	4.02	5.435	0.623
0.024	0.7906	0.4532	4.29	5.919	0.646
0.024	0.7556	0.4035	3.42	6.177	0.648

#### 4.7. Conclusions

The problem of siphon spillway discharge under free flow conditions has been investigated in the literature, but a knowledge gap exists about the problem under submerged exit conditions. In this chapter, numerical simulations of turbulent flow through the siphon spillway under submerged exit conditions have been conducted. The simulations produce numerical data of the flow velocity and pressure fields, which are complementary to observations from much more expensive and time-consuming laboratory experiments. In fact, it is technically challenging to make such observations for two reasons: 1) There are difficulties with accessing the siphon conduit; 2) there are undesirable disturbances to the flow to be measured if the devices for measurements are intrusive.

This chapter presents finite volume solutions to the two-phase Reynolds averaged momentum and continuity equations. The use of the volume of fluid method successfully captures the water levels in the upstream as well as the downstream reservoir. The numerical results are shown to be independent of the finite volume mesh configuration. The finite volume mesh properly resolves the near-wall boundary layers through spatial resolution refinement. For turbulence closure, the RNG k- $\epsilon$  model is shown to give a better performance than the Standard k- $\epsilon$  model and the realizable k- $\epsilon$  model. The RNG k- $\epsilon$  model has shown advantages in two aspects: 1) a realistic

prediction of the boundary layers off the upper and lower surfaces of the siphon conduit; 2) a consistent profile of the horizontal velocity at the siphon crest section outside the boundary layers, when compared with the well-established potential flow theory.

In the crest region, the flow velocity distributions are highly three dimensional, with rapid variations not only along the siphon conduit but also across it. The pressure field also exhibits complicated spatial variations. The gauge pressures are negative where the flow velocities are high. In the case of turbulent flow through the scaled model siphon, the predicted negative pressures in the crest region are not low enough to create the problem of cavitation. However, the prediction of negative pressures implies a potential problem of cavitation at the prototype scale.

The discharge coefficient  $C_d$  is a key parameter in the design of siphons, whose values under submerged exit conditions are not available from the existing literature. Numerical values of the discharge coefficient have been determined from the numerical results presented in this chapter. The  $C_d$  values are in a good agreement with the observed values of  $C_d$  from the laboratory experiments discussed in the previous chapter. It has been concluded that the discharge coefficient under submerged exit conditions is only slightly larger than that under free flow conditions.

The numerical simulations in this chapter cover the conditions of dimensionless driving head ( $DH/d$ ) up to 6.4 and dimensionless submergence level ( $H_2/d$ ) close to 4. The simulations deal with one specific siphon. With proper calibrations, the computational methods discussed in this chapter can be used to predict turbulent flows through siphon spillways of different dimensions and/or geometric configurations under other hydraulic conditions. The methods have the potential to produce velocity profiles, the maximum velocity, and pressure distributions in siphon conduits, particularly in the crest regions.

## Chapter Five

### 5. Distributions of mean flow velocity and turbulence

#### 5.1. Introduction

The previous chapter presents the computational results of siphon flow, with the focus on the crest region. The crest region is the most critical from the perspective of siphon design because of the risks of cavitation, and is the only region in most cases, about which studies of siphon flow in free discharge conditions are concerned. The distributions of the longitudinal flow velocity and pressure in the crest region are of primary importance. For this reason, details of turbulence characteristics along the entire siphon conduit path from its entrance and exit (Figures 3.5, 4.1 and 4.12) and secondary flows in planes perpendicular to the path are rarely discussed.

The turbulence and secondary flow characteristics play an important role in siphon discharge efficiency in submerged exit conditions. This chapter provides detailed discussions of the characteristics based on the computational results for Run RN4 (Table 4.1). Turbulence kinetic energy (TKE) is one of the main turbulence characteristics. Its distribution along the siphon conduit and magnitude are the main cause of low efficiency of a siphon spillway. The mechanisms that explain the distribution of TKE and turbulence intensity are discussed in detail. The discussions include the production of turbulence.

#### 5.2. Energy cascade

Energy cascade is an important concept in the theory of turbulence production. In almost all hydraulic engineering applications, the flow is a turbulent flow. So is the flow through a siphon spillway. Turbulent motions exist on both a macro- and micro-scale. At the macro-scale, the energy is supplied, and at the micro-scale, the energy is dissipated by viscosity. The interaction among the various scale eddies means that energy is sequentially transferred according to the “turbulent energy cascade,” from larger eddies to smaller ones. The large eddies are unstable, and eventually break down into small and smaller ones. So, the kinetic energy is transferred down-scale until the eddies are sufficiently small in length scale, to a point where fluid viscosity effectively dissipates kinetic energy (Figure 5.1). Kolmogorov’s theory explains how this sequential down-scale transfer of energy is achieved. This theory describes how much energy is contained and dissipated by eddies of a given size.

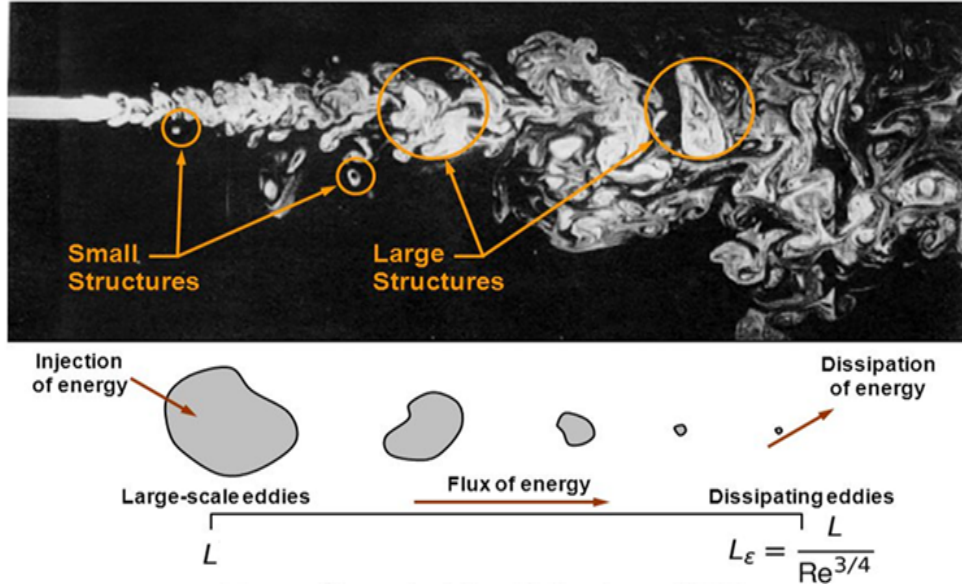


Figure 5-1. Eddy energy transfer. (Richardson, 1922)

The length scale  $I_o$  of the larger eddies is estimated as:

$$I_o \propto \frac{k^{3/2}}{\varepsilon} \quad (5.1)$$

where  $\varepsilon$  ( $\text{m}^2/\text{s}^3$ ) is the dissipation rate of the turbulence kinetic energy  $k$ . The definition of  $k$  is:

$$k = \frac{1}{2} (\overline{u_1'^2} + \overline{u_2'^2} + \overline{u_3'^2}) \quad (5.2)$$

where the overbar denotes time average of the fluctuating velocities (Equation 4.1) squared. The results of  $k$  presented in this chapter are the numerical solutions to Equation (4.13). The Reynolds number associated with large eddies is referred to as the turbulence Reynolds number:

$$Re_L = \frac{k^{1/2} I_o}{\nu} \quad (5.3)$$

This energy cascade continues to transfer energy down-scale until the Reynolds number ( $Re$ ) becomes small enough that the eddy motion stabilises and molecular viscosity effectively dissipates kinetic energy, which gets transformed into heat. The dissipation of kinetic energy occurs in the final steps of the cascade.

The length, velocity and time scales of the smallest eddies are known as the Kolmogorov scales (see e.g., Pope, 2002), given by:

Length scale:  $\eta = (\nu^3/\varepsilon)^{1/4} \quad (5.4)$

Velocity scale:  $u_\eta = (\varepsilon\nu)^{1/4}$  (5.5)

Time scale:  $t_\eta = (\nu/\varepsilon)^{1/2}$  (5.6)

These scales are interrelated as

$$(u_\eta/\eta) = 1/t_\eta \quad (5.7)$$

They give the Kolmogorov Reynolds number:

$$Re_\eta = \eta u_\eta/\nu = 1 \quad (5.8)$$

At these scales, the turbulence kinetic energy is dissipated. In turbulent flow, there are two basic processes: 1) There is an exchange of energy between the mean flow and turbulence and is subject to the dynamics of large eddies; 2) turbulent energy is subject viscous dissipation, and this mainly occurs at levels comparable to the Kolmogorov microscope (Tennekes and Lumley, 1972, p. 68).

### 5.3. Energy spectrum

The Kolmogorov Reynolds number for the small eddies is 1. This value supports the theory that the cascade transfers energy down-scale until the Reynolds number is small enough for kinetic energy to be dissipated (Pope, 2000). The turbulence in eddies is commonly characterised by the Taylor-scale Reynolds number:

$$R_\lambda = \frac{\lambda u'}{\nu} \quad (5.9)$$

This Reynolds number is based on the eddies' length scale ( $\eta$ ) and the corresponding velocity scale. In Figure 5.2, the empirical measurement of a one-dimensional spectra (one velocity component only) is shown. The value at the end of each reference denotes the value of  $R_\lambda$  (Equation 5.9) for which the measurements were made.

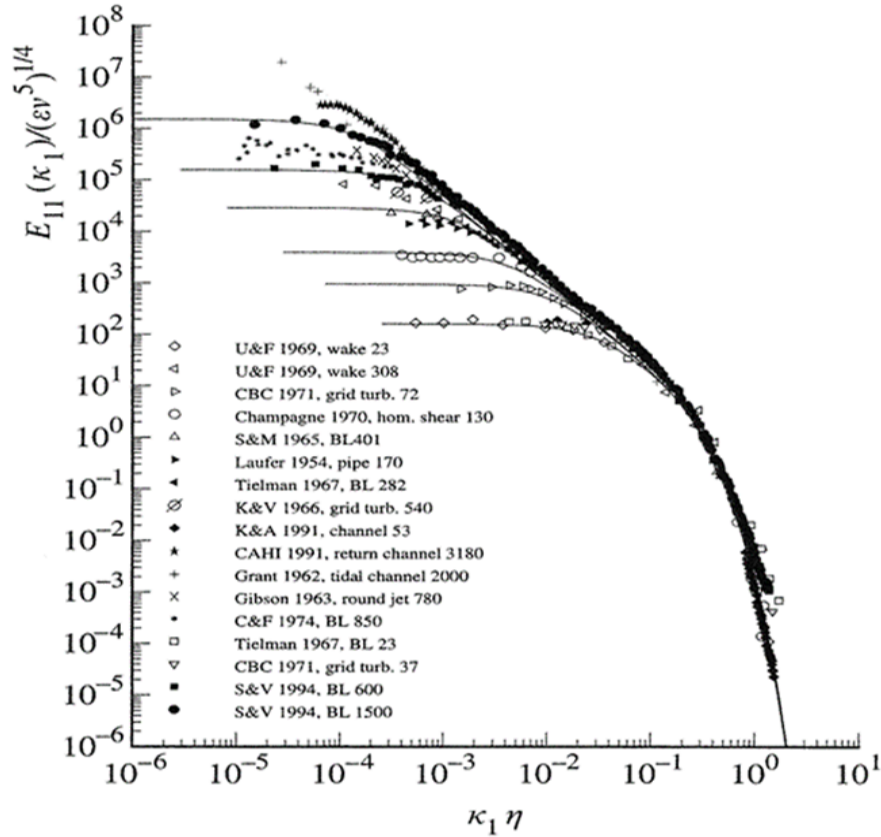


Figure 5-2. Empirical results for spectra (Pope, 2000), where  $\kappa_1$  is the wavenumber (*in m<sup>-1</sup>*), and  $E_{11}$  is the energy spectrum (*in kg m<sup>2</sup> s<sup>-2</sup>*).

#### 5.4. Turbulence intensity and turbulence kinetic energy

As stated in Section 2.1, the Kolmogorov scales give a measure of the length, velocity and time scales for the smallest eddies in turbulent flow. Turbulence intensity,  $I$ , is another important variable for describing turbulent flow. It is defined as

$$I = \frac{\sqrt{u_1'^2}}{U} \quad (5.10)$$

The numerator is the root mean square of the turbulent velocity fluctuations, and  $U$  is the mean velocity. Turbulence intensity gives an idea how intense the turbulent fluctuations are, and it can be written in terms of the specific normal Reynolds stress components ( $\overline{u_1'^2}$ ,  $\overline{u_2'^2}$  and  $\overline{u_3'^2}$ ). Their physical meaning is the kinetic energy per unit mass of the fluctuating velocity field in the three coordinate directions (Wilcox, 2006, p. 44).

### 5.5. Flow separation

The phenomenon of flow separation and subsequent reattachment are caused by a sudden change in flow direction. Flow separation are expected at the siphon entrance, over the siphon crest, and around the deflector. The flow is three dimensional. The separation zones result in a noticeable head loss. In Figure 5.3, the streamlines show the general flow features for flow separation from a solid wall. At the point of separation labeled as 'S', the wall shear stress is

$$\tau_w = \mu \left( \frac{\partial u}{\partial y} \right)_w = 0 \quad (5.13)$$

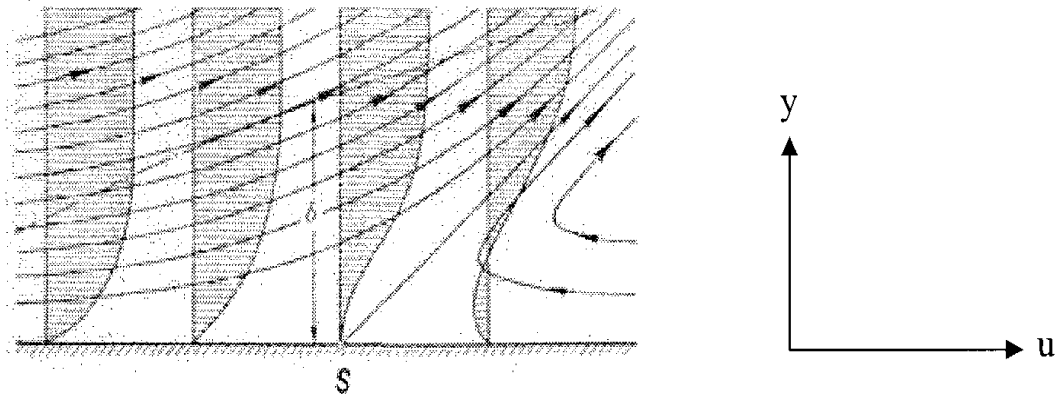
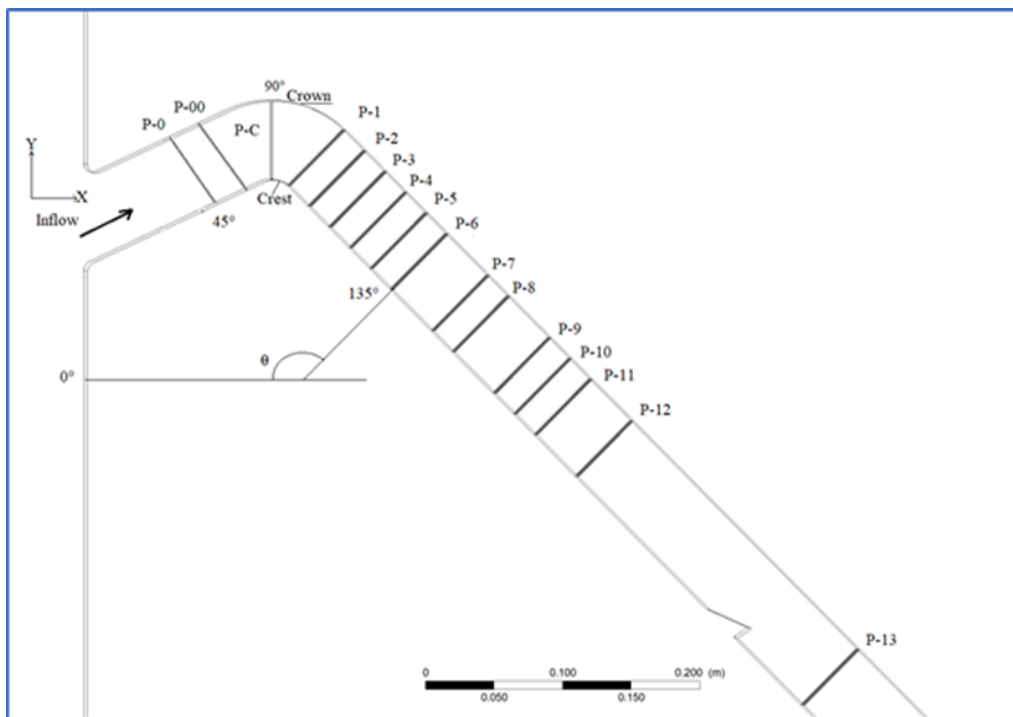


Figure 5-3. Boundary-layer flow showing the point of separation *S* (Schlichting, 2000).

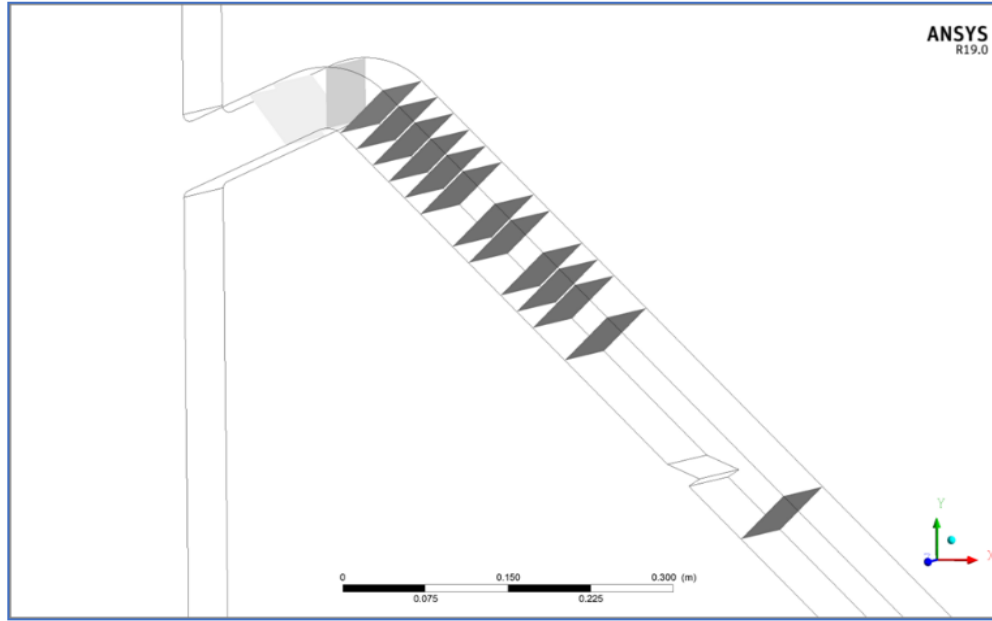
## 5.6. Distributions of the mean flow velocity

Run RN4 produced (Table 4.1) computational results of siphon flow at equilibrium at model time  $t = 20.8$  s. A description of the computational modelling theory, along with numerical setup, is given in Chapter 4. In the following, the computed flow field in the siphon conduit, including the primary flow velocity, secondary flow velocity and turbulence kinetic energy, are discussed. To facilitate discussions, two cross sections (P-0 and P-00) in the upper leg (Figure 3.5a), 13 cross sections (P-1 to P-13) in the lower leg (Figure 3.5a), and the crest section (P-C) are selected (Figure 5.4). Cross section P-C intersects the lower surface of the siphon conduit at  $x = 1.64$  m, and the lower leg cross-sections are: P-1 intersects at  $x = 1.67$  m, P-2 at  $x = 1.70$  m, P-3 at  $x = 1.73$  m, P-5 at  $x = 1.79$  m, P-7 at  $x = 1.85$  m, P-12 at  $x = 2.02$  m, and P-13 at  $x = 2.20$  m (as a reference, the siphon exit is at  $x = 2.28$  m). The upper leg cross-sections are: P-00 intersects at  $x = 1.60$  m, and P-0 at  $x = 1.57$  m.



(a)

(Figure 5.4 continued)



(b)

Figure 5-4 Selected cross sections: (a) view in the  $xy$  plane; (b) 3-D view.

It is important to distinguish between the primary velocity and secondary velocity of the mean flow (Equation 4.1). The mean-flow velocity vector is expressed as

$$\vec{V} = U\hat{x} + V\hat{y} + W\hat{z} \quad (5.14)$$

where  $\hat{x}$ ,  $\hat{y}$  and  $\hat{z}$  are unit vectors in  $x$ -,  $y$ - and  $z$ -direction, respectively (the equivalent tensor form is  $\vec{V} = U_1\hat{x}_1 + U_2\hat{x}_2 + U_3\hat{x}_3$ ). The magnitude of the velocity vector is calculated as

$$|\vec{V}| = \sqrt{U^2 + V^2 + W^2} \quad (5.15)$$

In Figure 4.12, an example of the velocity vector distribution in the plane of symmetry (at  $z = 0.125$  m) is shown. At any cross section (like those shown in Figure 5.4) that is locally perpendicular to the siphon conduit path, the projection of  $\vec{V}$ , with the  $W$  component excluded, in the direction normal to the cross section is the primary flow velocity at that cross section. The primary flow velocity is a vector itself, pointing either out of the cross section or into it. The projection of  $\vec{V}$  in the direction tangent to the cross section is the secondary flow velocity at that cross section. The secondary flow velocity is also a vector itself, whose starting and ending points are in the cross section. If a cross section forms an angle  $q$  with the  $x$  axis (Figure 5.4a), the secondary flow velocity vector of  $\vec{V}_s$  is calculated as

$$\vec{V}_s = [U\cos(180^\circ - \theta) + V\cos(\theta - 90^\circ)]\hat{t} + W\hat{z} \quad (5.16)$$

where  $\hat{t}$  is a unit vector, whose starting and ending points are in the cross section and its direction is at a  $90^\circ$  angle with  $z$  direction.

The magnitude of the primary flow velocity vector of  $\vec{V}_p$  is calculated as

$$\vec{V}_p = [U\sin(180^\circ - \theta) - V\sin(\theta - 90^\circ)]\hat{n} \quad (5.17)$$

where  $\hat{n}$  is a unit vector, which is normal to the cross section and points towards downstream.

### 5.6.1 Longitudinal distribution of flow velocity

In Figure 5.5, the magnitude of the 3-D flow velocity (Equation 5.15) is plotted as contours in the plane of symmetry. The maximum magnitude was predicted to occur near the crest. The maximum magnitude (5.2 m/s) depended on the head driving the siphon flow. As expected, the velocity magnitude varied along the length of the siphon conduit. At any given cross section perpendicular to the length, the magnitudes were small near the upper and lower surfaces of the conduit. In the near-surface regions, the flow reversed direction or a boundary layer developed or both. The change in magnitude was rapid in the crest region.

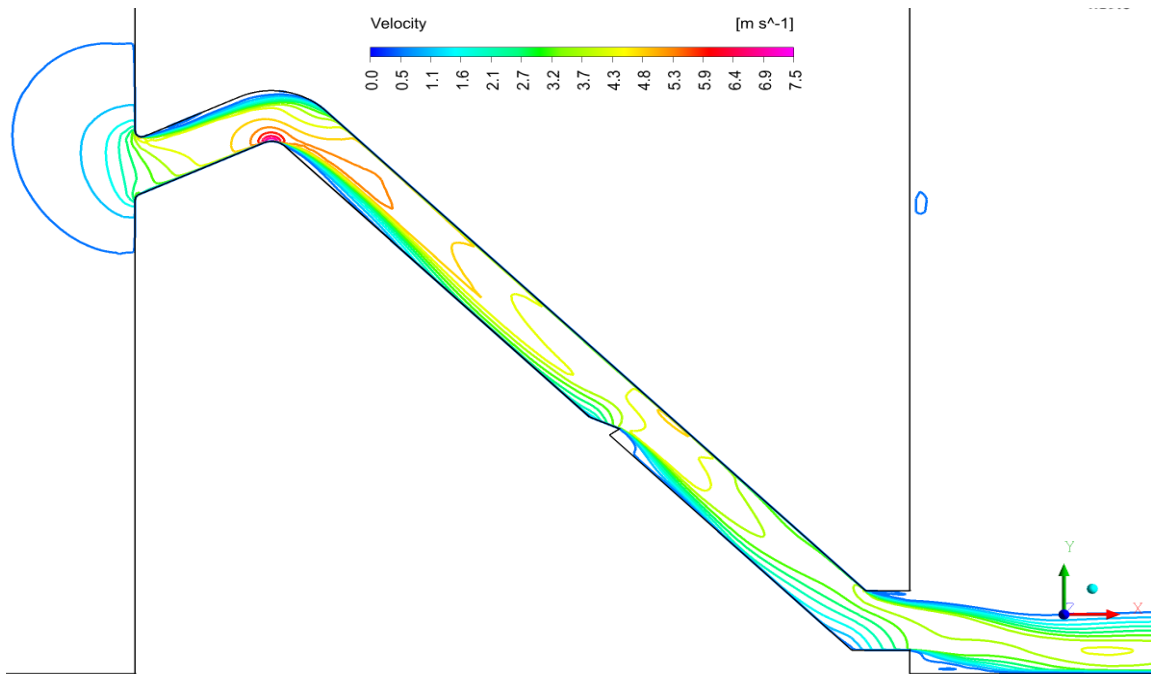


Figure 5-5. A longitudinal section at  $z = 0.125$  m (the plane of symmetry), showing contours of the magnitude of mean flow velocity,  $\sqrt{U^2 + V^2 + W^2}$  (in m/s), for Run RN4 (Table 4.1). The largest magnitude occurred near the crest.

Right above the siphon entrance, the vertical front-wall of the upstream reservoir formed an obtuse angle of  $115^\circ$  with the upper surface of the siphon's upper leg (Figure 3.5; Figure 5.6). In the reservoir, streamlines converged when approaching the siphon entrance. Those streamlines that hugged the front-wall downward could not make the full  $115^\circ$  turn into the upper leg (Figure 5.6); they could not follow the large curvature [equal to  $(f/2)^{-1} = 157.5 \text{ m}^{-1}$ ] of the circular lip, even though the entrance was well-rounded at the lip (Figure 3.5). The result was flow separation along the upper surface of the upper leg (Figure 5.6). The fluid circulation in the separation zone was at the expenses of the driving head (Figure 3.5) and thus reduced the discharge efficiency.

The flow streamlines further contracted in the upper leg as the flow passed around the crest. After the flow passed the crest, the flow curvature was no more able to follow the downstream turn of the conduit. As a result, the flow separated from the lower surface of the lower leg downstream of the crest. The fluid rotated in the zone, and an eddy formed (Figure 5.6). Further downstream along the conduit, strong fluid rotation and eddy motions appeared behind the deflector. The highest velocity magnitude was  $U_{max} = 7.44 \text{ m/s}$  near the crest (at a driving head larger than that in Figure 5.5). The lowest velocity magnitude always appeared in the flow separation zones. The eddies shown in Figures 5.5 and 5.6 had length, time and velocity scales much larger than those given in Equations (5.4) to (5.6).

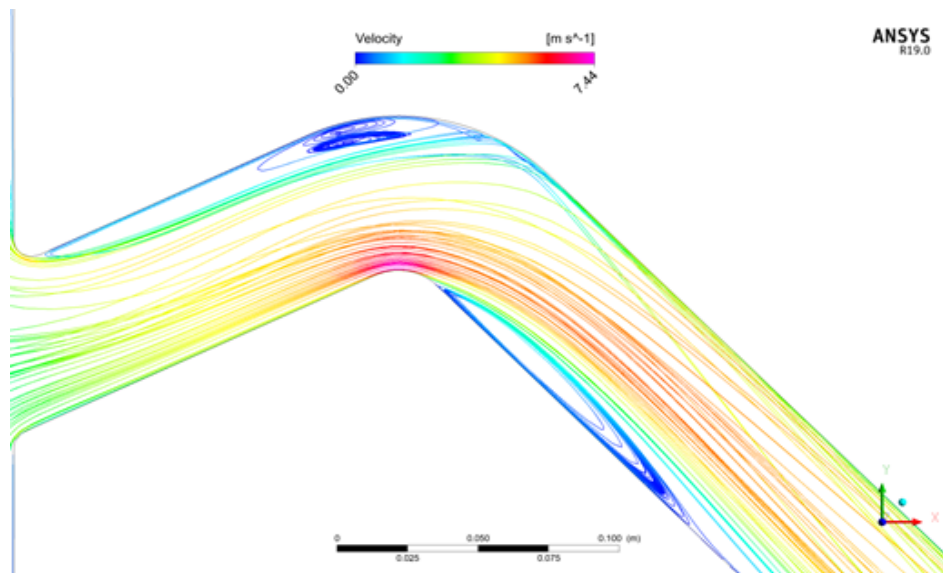


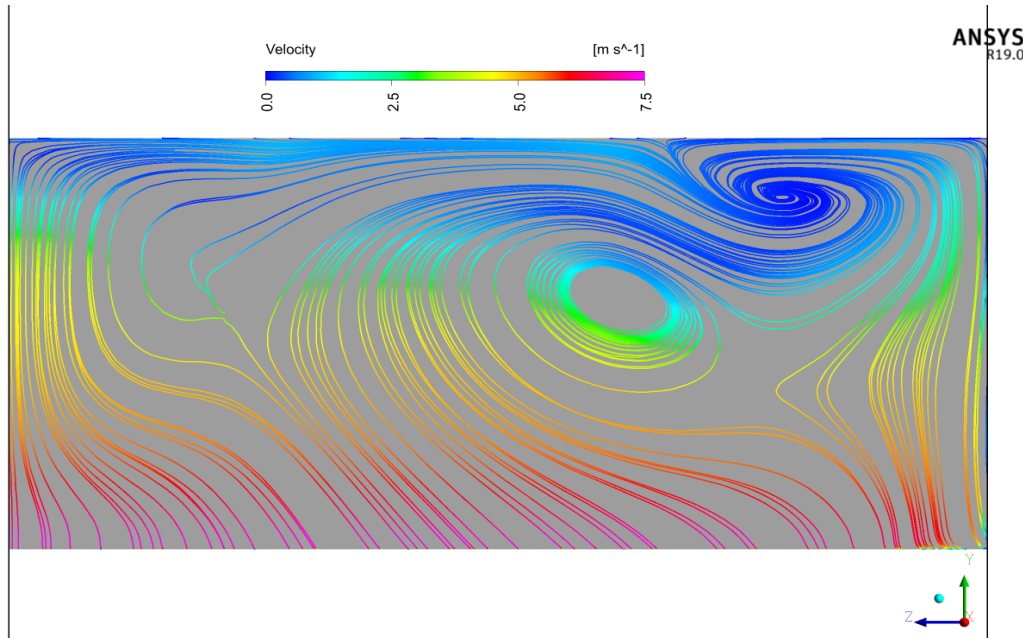
Figure 5-6. A longitudinal section at  $z = 0.0625 \text{ m}$  (the middle between the plane of symmetry at  $z = 0.125 \text{ m}$  and the sidewall  $z = 0$ ), showing contours of the magnitude of mean flow velocity,

$\sqrt{U^2 + V^2 + W^2}$  (in m/s), for Run RN4 (Table 4.1). The largest magnitude occurred near the crest.

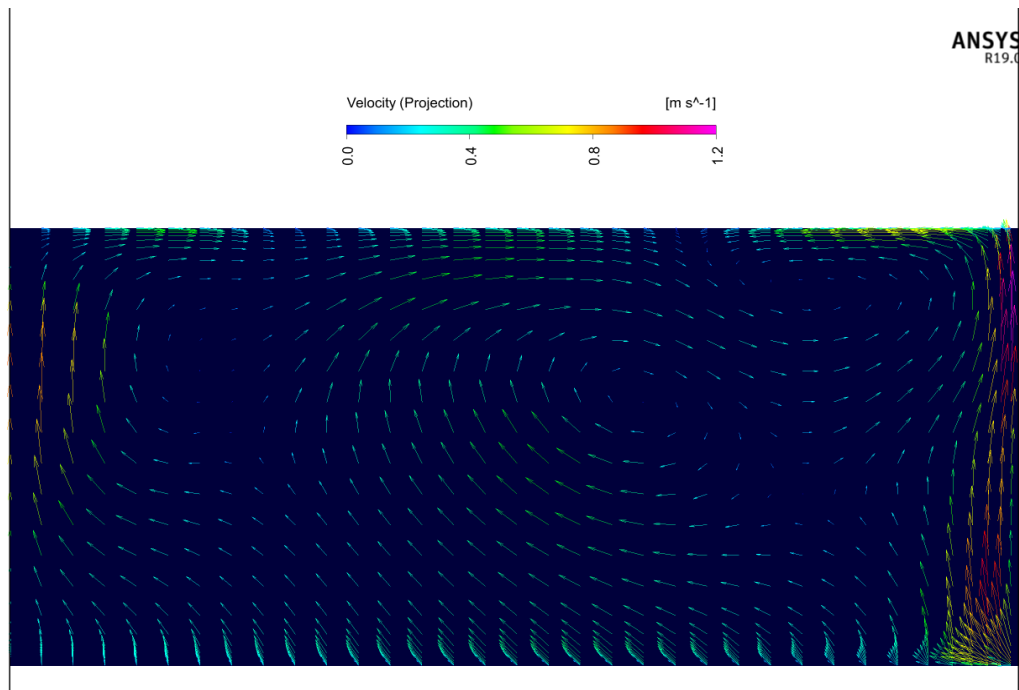
### **5.6.2 Cross-sectional distribution of flow velocity**

Driven by available energy head (Equations 3.7 and 3.8), the primary flow velocity (Equation 5.17) carried discharge through the siphon conduit (Figures 4.12, 4.13 and 5.5). However, due to turbulence, secondary flows (Equation 5.16) perpendicular to the primary flow direction existed in cross sections (Figure 5.4). In Figures 5.7 to 5.14, examples of cross-sectional distributions of the primary and secondary flows are shown.

At crest section P-C (Figure 5.7a), the 3-D flow velocities had larger magnitudes (Equation 5.15) in the lower part of the cross section than the upper part. Within the lower part, the magnitudes varied from point to point, and the variations were more profound in the lateral direction (or along the  $z$  axis) and in the direction perpendicular to the  $z$  axis. Within the upper part, the magnitudes showed two low velocity zones with local minima. The locations of the local minima were the centres of secondary flow eddies (Figure 5.7b). The secondary flow had the largest strength near the sidewall (the right edge of panel b) and near the plane of symmetry (the left edge of panel b). The largest strength was about 1.2 m/s, compared to the largest strength of the 3-D flow velocity of 7.47 m/s, giving a 16% ratio. The secondary flow circulations did not contribute to flow discharge through the siphon spillway.



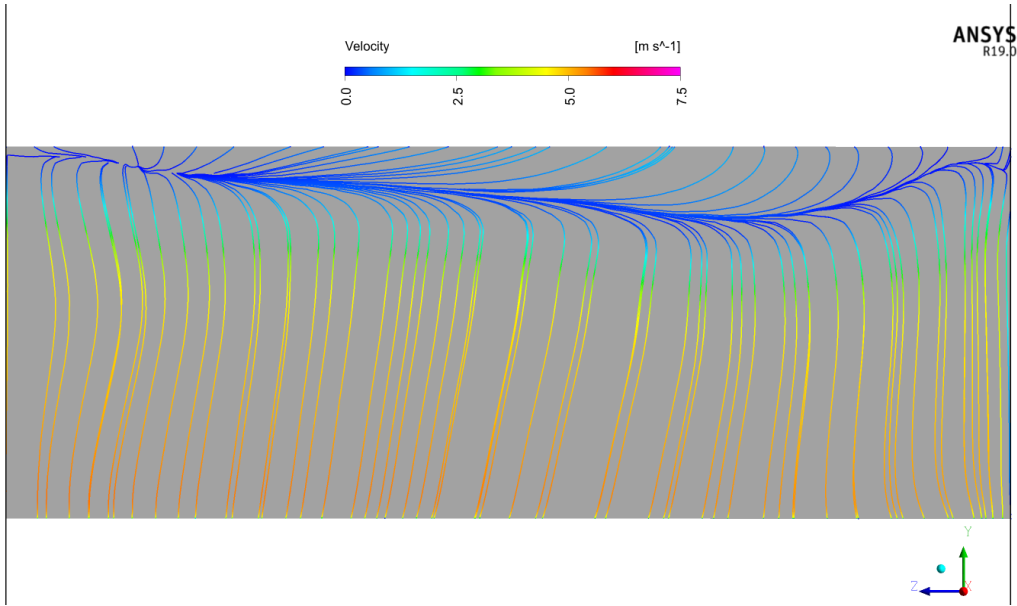
(a)



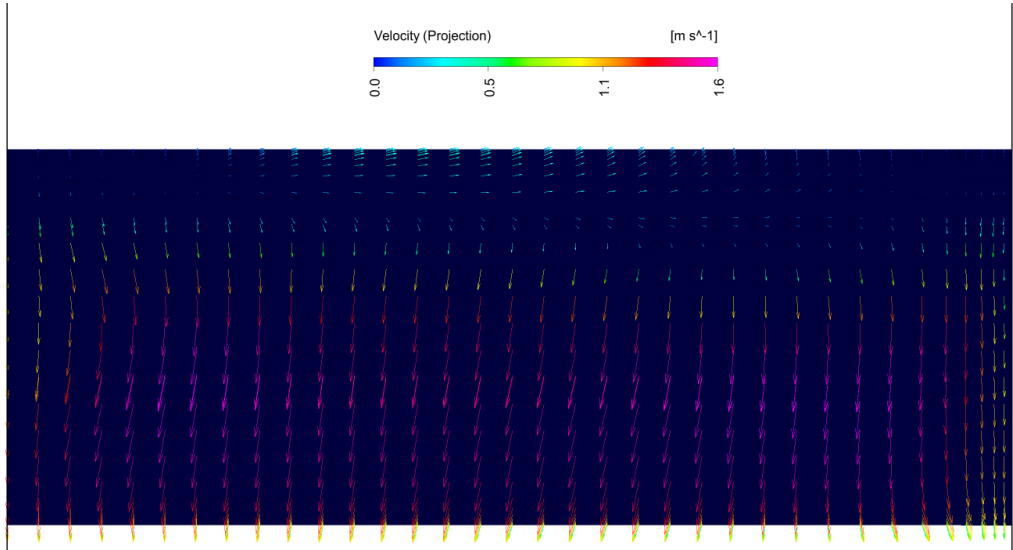
(b)

Figure 5-7. Flow velocity distributions at cross-section P-C (Figure 5.4): (a) contours of the 3-D flow velocity's magnitude (Equation 5.15); (b) vectors of the 2-D secondary flow velocity (Equation 5.16). The left edges of the panels are the plane of symmetry, and the right edge is the sidewall.

At cross-section P-00 (Figure 5.4) upstream of the crest, the 3-D flow velocities (Equation 5.15) had more or clear uniform magnitudes (Figure 5.8a) at the cross section, except in the near-top zone above a zero-velocity line. This zone was a flow separation zone (Figure 5.6), resulting from on the effect of the curved surface at the siphon entrance. The velocity magnitudes increased gradually to reach maximum values close to the crest surface. The secondary flow (Figure 5.8b) had little structure.



(a)



(b)

Figure 5-8. Flow velocity distributions at cross-section P-00 (Figure 5.4). Other remarks are the same as in Figure 5.7.

At cross-section P-1 (Figure 5.4) downstream of the crest, the 3-D flow velocity showed a complicated distribution of magnitudes (Figure 5.9a). The general feature was relatively strong magnitudes in the upper part of the cross section and weak magnitudes in the near-bottom zone.

In the upper part, there were three local minima of magnitudes (Figure 5.9a) at the centres of secondary flow eddies (Figure 5.9b). The weak magnitudes in the lower part were due to flow separation under the impact of the centrifugal force associated with the crest curvature.

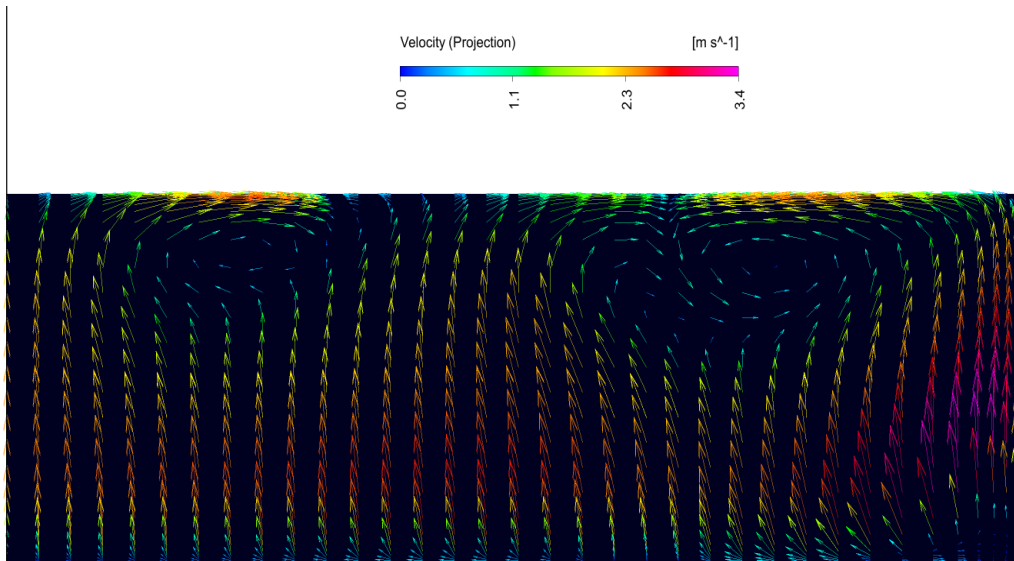
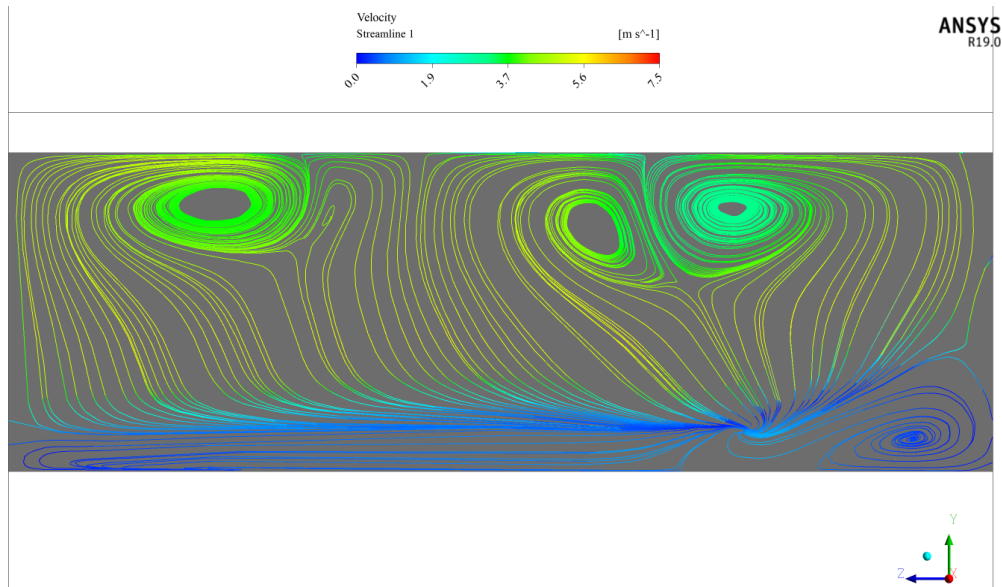
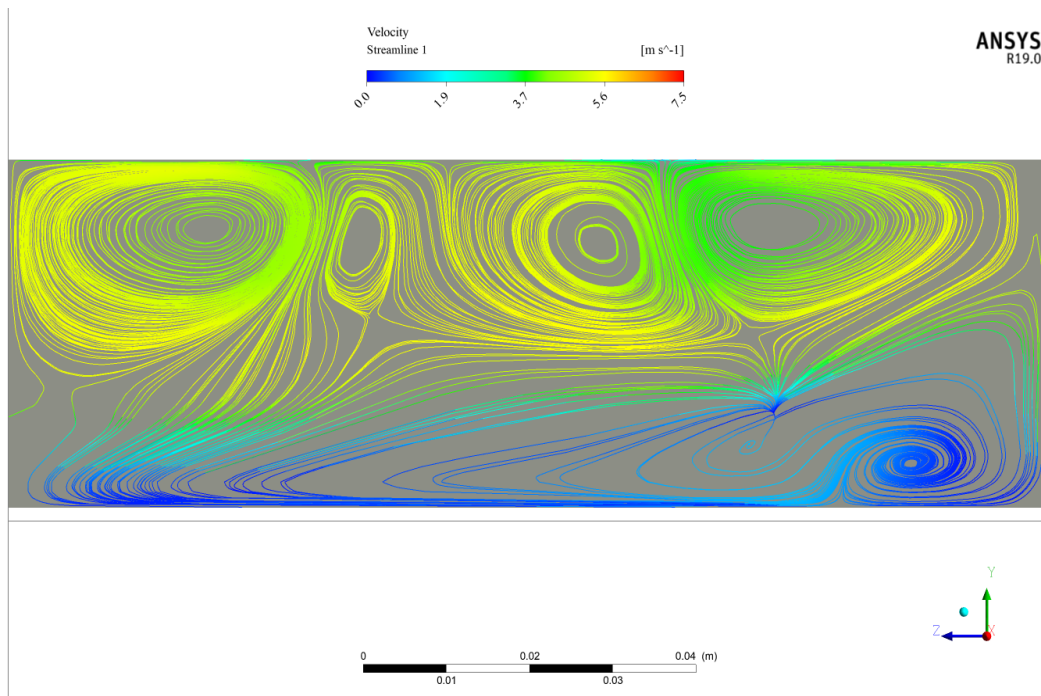


Figure 5-9. Flow velocity distributions at cross-section P-1 (Figure 5.4). Other remarks are the same as in Figure 5.7.

At cross-sections P-2 and P-7 (Figure 5.4) further downstream, the 3-D flow velocity (Equation 5.15) had very complicated structures, with rapidly varied magnitudes (Figures 5.10a, 5.11a). The secondary flows showed multiple zones of complicated eddy motions (Figures 5.10b, 5.11b). The complicated structures were due to the interactions of flow separation, wall boundary layer, vortex formation. The 3-D flow velocities were stronger in their upper parts of the cross sections. As for the secondary flows, the vortices varied in core strength and core size. From cross section P-2 to P-7, the secondary flows weakened. The largest strength dropped from 1.7 m/s to 1.2 m/s, and shifted in position from near the top surface to the lower surface of the siphon conduit.

In Figure 5.11b, vortices were generated in the lower left corner by recirculation of fluids directing away from the siphon sidewall. At cross section P-12, the flows recovered to gain uniformity (Figure 5.12), without much secondary circulations.



(Figure 5.10 continued)

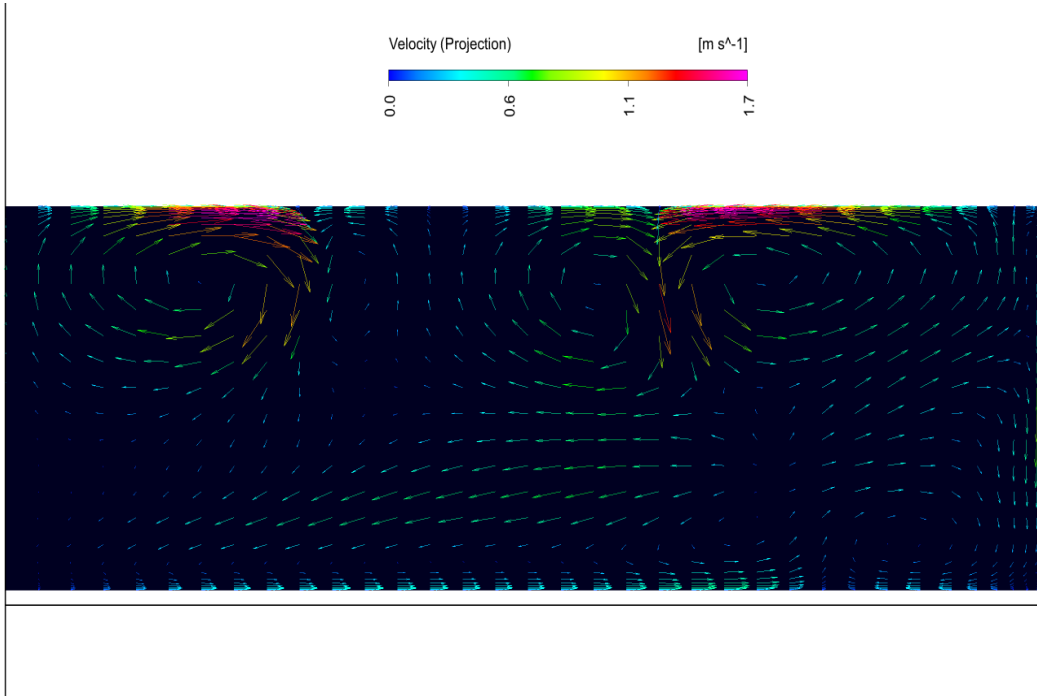
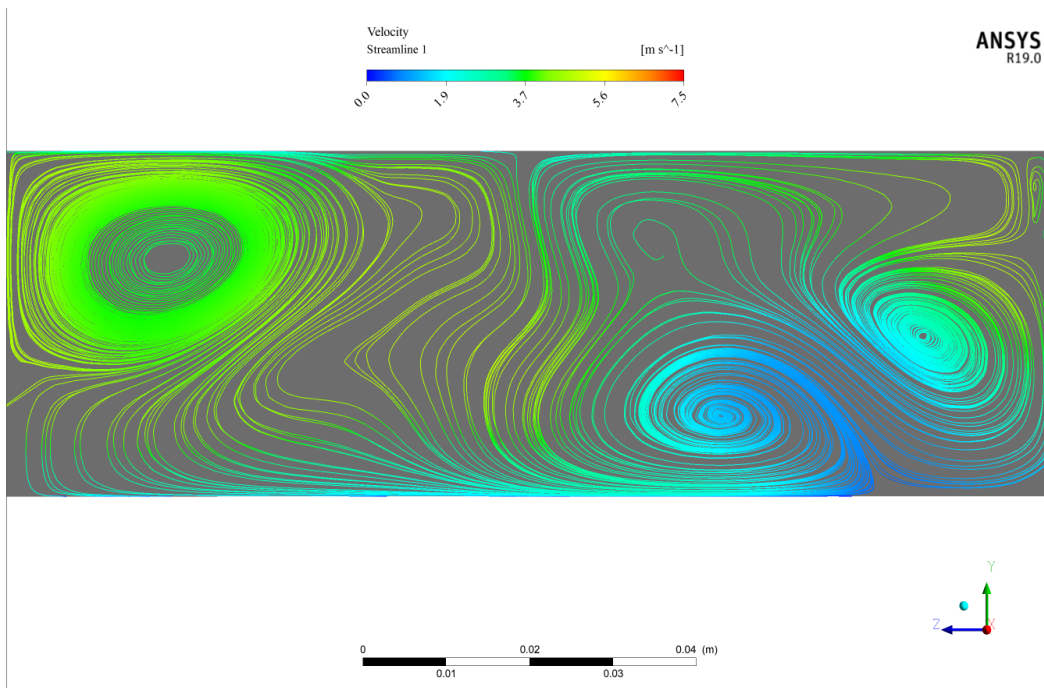
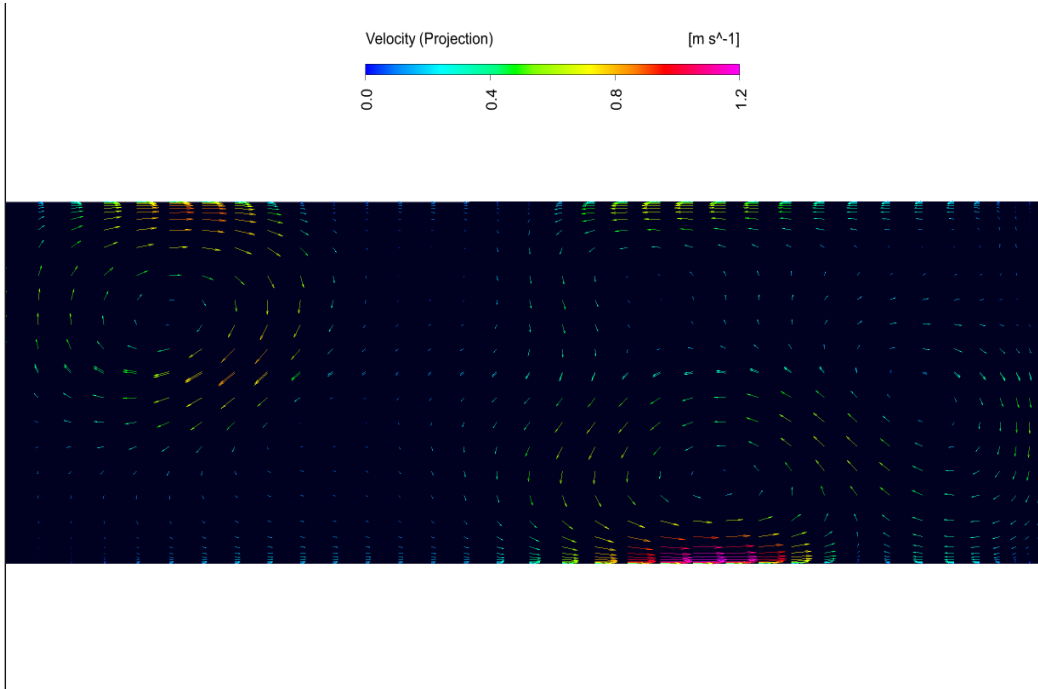


Figure 5-10. Flow velocity distributions at cross-section P-2 (Figure 5.4). Other remarks are the same as in Figure 5.7.



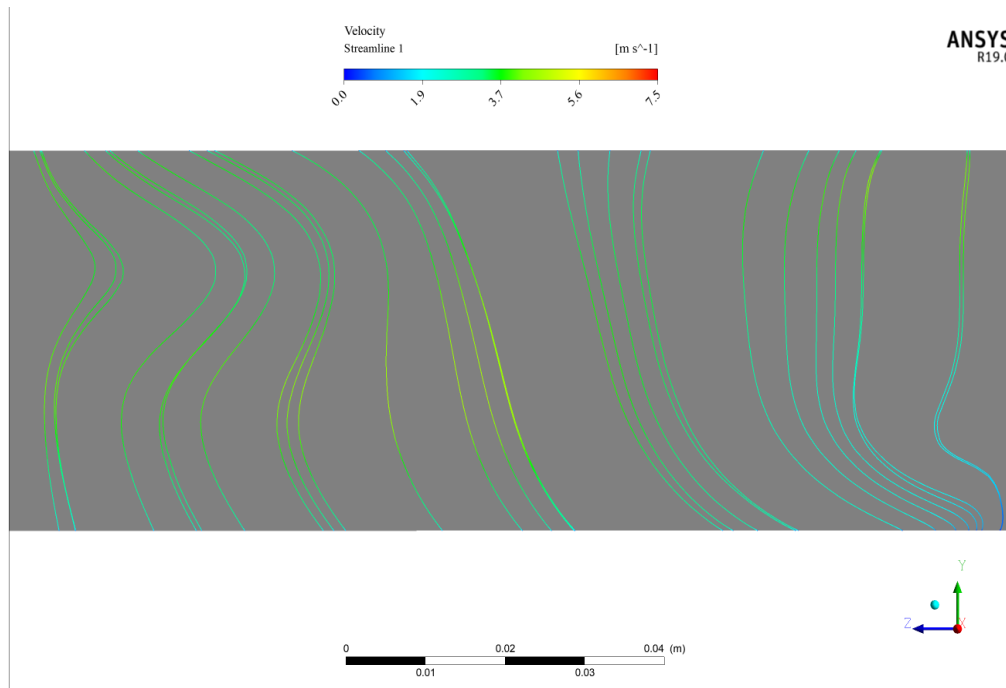
(Figure 5.11 continued)

(a)



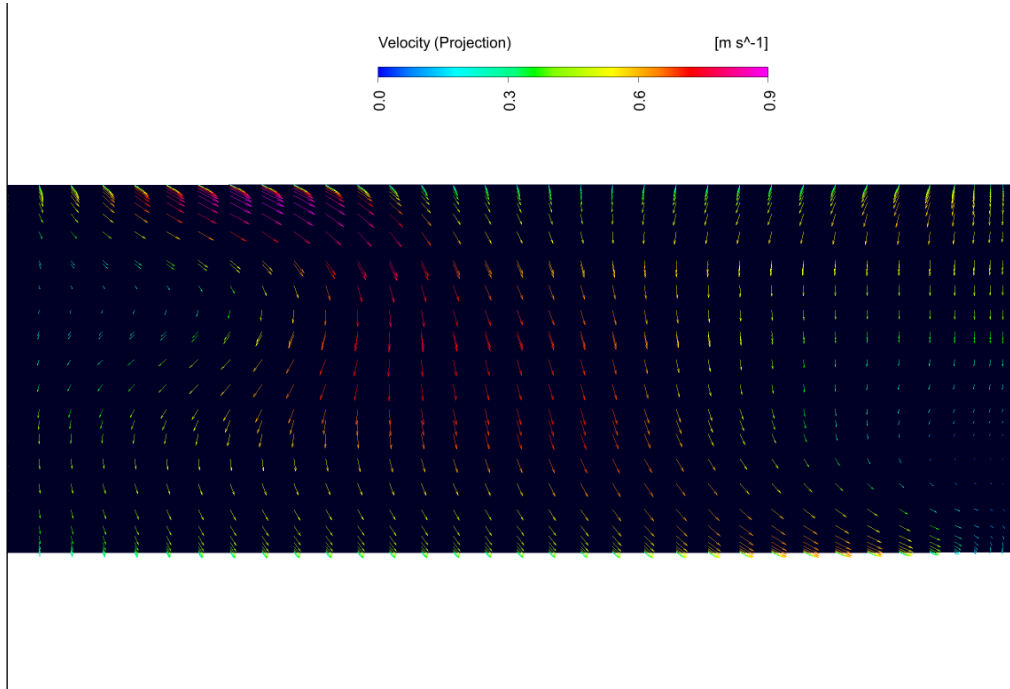
(b)

Figure 5-11. Flow velocity distributions at cross-section P-7 (Figure 5.4). Other remarks are the same as in Figure 5.7.



(Figure 5.12 continued)

(a)



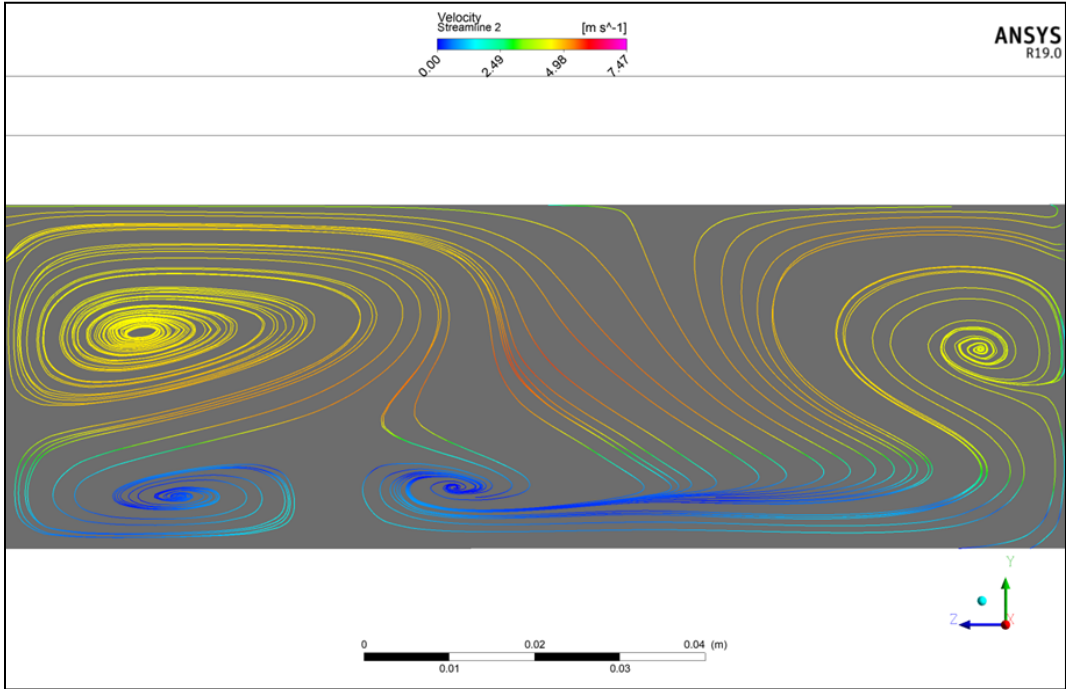
(b)

Figure 5-12. Flow velocity distributions at cross-section P-12 (Figure 5.4). Other remarks are the same as in Figure 5.7.

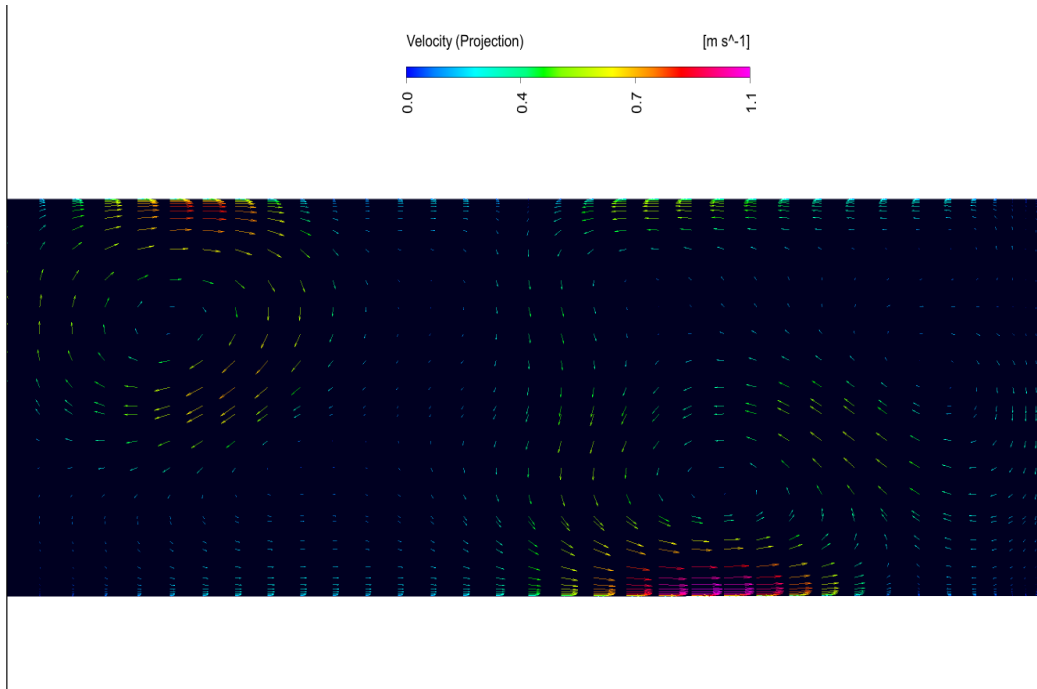
From Figures 5-7 to 5-12, it can be noticed that the distributions of the primary flow changed toward downstream from cross-section P-1, to P-2, and to P-7 due to flow separation, and secondary flows began to form at the crest, reached the maximum very quickly (at cross section P-2), weakened gradually toward downstream until secondary circulations of fluids diminished.

At cross-section P-13 downstream of the deflector (Figure 5.13), new vortices appeared in the secondary flow distribution and flow separation took place. The non-uniform flow distributions were directly due to the constriction of flow area by the deflector. It forced the flow to separate from the lower surface of the siphon conduit. The horizontal velocity component  $U$  increased, and so did the lateral and vertical velocity components near the upper surface of the siphon conduit.

At the siphon exit, the 3-D flow velocity had more or less uniform magnitudes at the cross section (Figure 5.14a) except in the near-top zone where flow reversal took (Figure 4.13), however, the secondary flows had significant magnitudes because of the downward step. The eddies in Figures 5.7b to 5.14b had length, time and velocity scales much larger than those given in Equations (5.4) to (5.6).

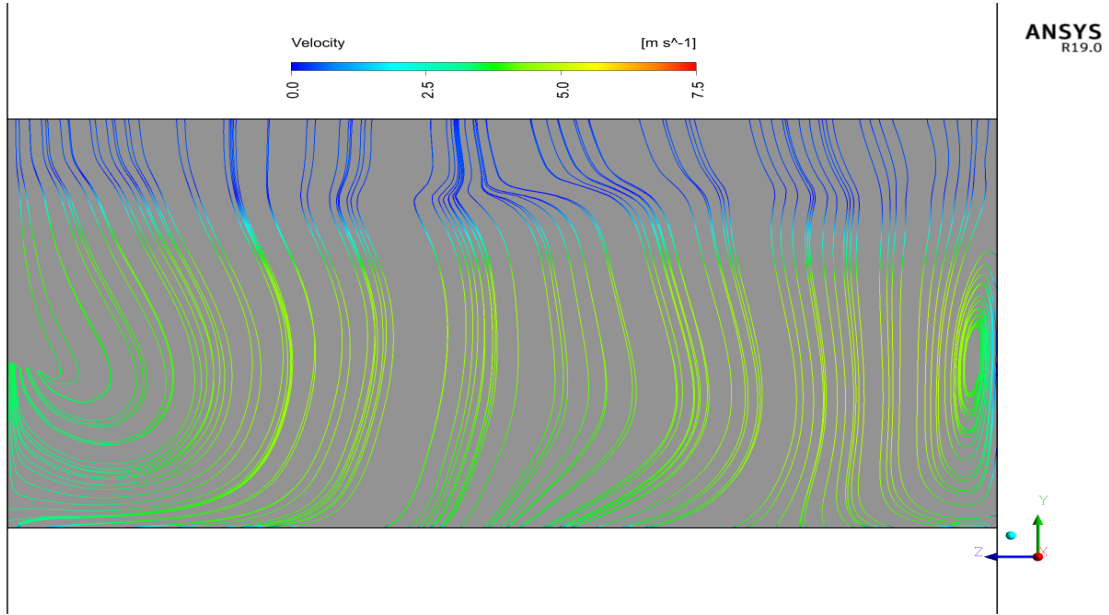


(a)

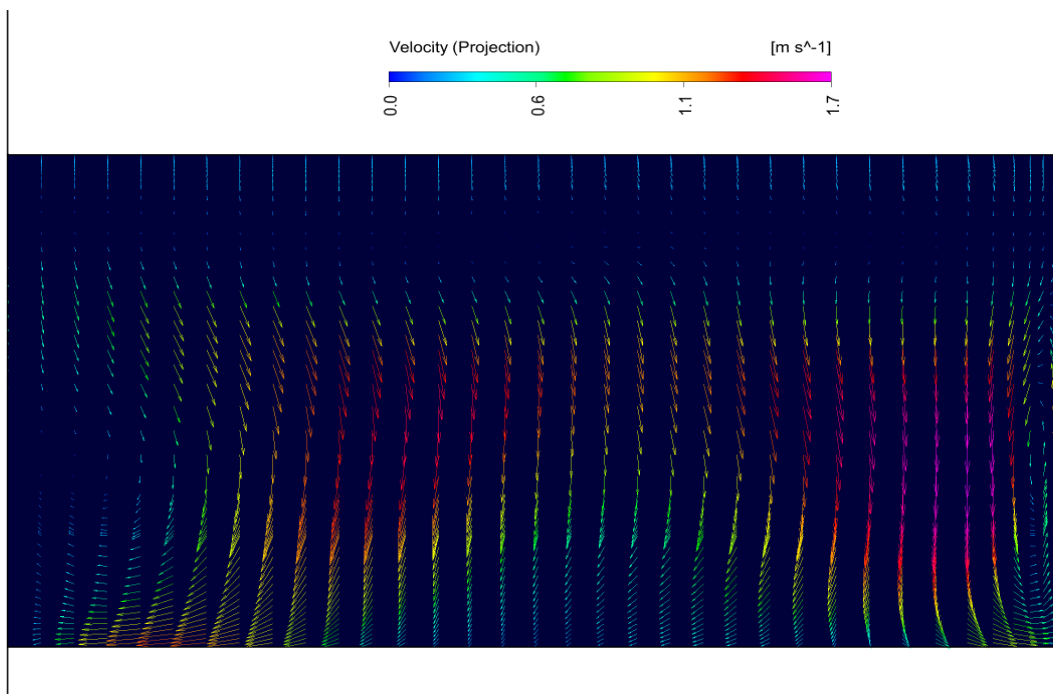


(b)

Figure 5-13. Flow velocity distributions at cross-section P-13 (Figure 5.4). Other remarks are the same as in Figure 5.7.



(a)



(b)

Figure 5-14. Flow velocity distributions at the siphon exit cross-section  $x = 2.28$  m. Other remarks are the same as in Figure 5.7.

## 5.7. Distribution of turbulence kinetic energy

### 5.7.1 Longitudinal distribution of turbulence kinetic energy

Longitudinal distributions of specific turbulence kinetic energy,  $k$ , (Equation 5.2) are plotted for a near-sidewall vertical plane at  $z = 0.02$  m (Figure 5.15), the plane of symmetry at  $z = 0.125$  m (Figure 5.16), and a vertical plane in between at  $z = 0.074$  m (Figure 5.17). In the near-sidewall plane, the most noticeable feature was an elongated zone of large  $k$  values downstream of the crest.

This zone was a flow separation zone (Figure 5.6). Another feature was a stretch of relatively large  $k$  values along the upper surface of the siphon conduit, starting from the entrance lip and extending beyond the crown. In the near-sidewall plane, the highest value of  $k$  is  $1.4 \text{ m}^2/\text{s}^2$ , giving a square root of  $1.18 \text{ m/s}$ , which can be used for comparison to the primary and secondary flow velocities.

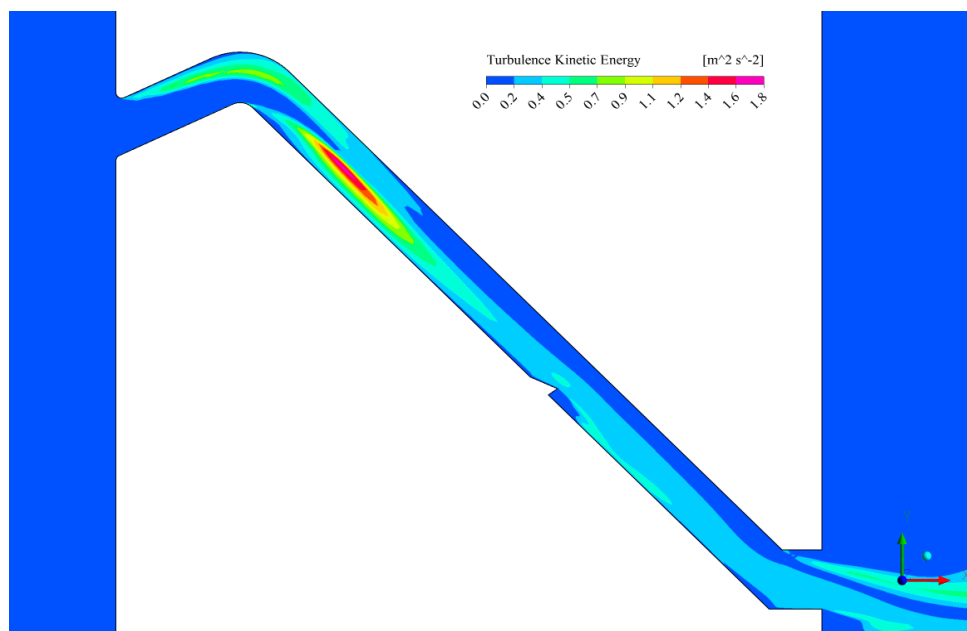


Figure 5-15. Vertical section at  $z = 0.02$  m, showing longitudinal distribution of  $k$ . The model time was  $t = 22.8$  s; the upstream and downstream reservoirs' water levels (Figure 4.1) were  $H_1 = 2.20$  m, and  $H_2 = 0.432$  m, respectively.

In the plane of symmetry, there were three elongated zones of high  $k$  values: one just downstream of the crest, one downstream of the deflector, both along the lower surface of the siphon conduit, and one near the crown (Figure 5.16). At the crest section,  $k$  had a maximum value of  $0.7 \text{ m}^2/\text{s}^2$ .

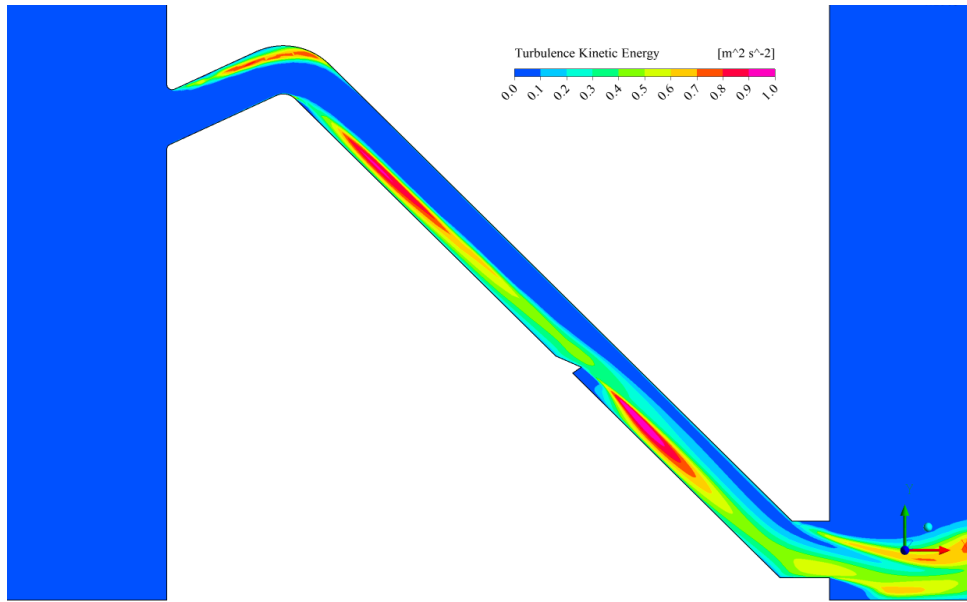


Figure 5-16. Vertical section at  $z = 0.125$  m, showing longitudinal distribution of  $k$ . The model time was  $t = 22.8$  s; the upstream and downstream reservoirs' water levels (Figure 4.1) were  $H_1 = 2.20$  m, and  $H_2 = 0.432$  m, respectively.

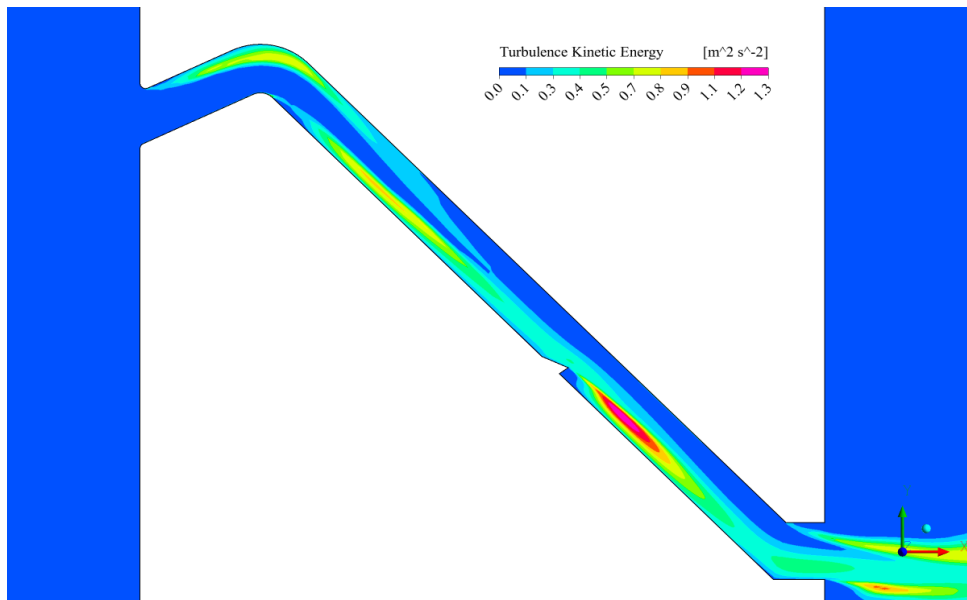


Figure 5-17. Vertical section at  $z = 0.074$  m, showing longitudinal distribution of  $k$ . time was  $t = 22.8$  s; the upstream and downstream reservoirs' water levels (Figure 4.1) were  $H_1 = 2.20$  m, and  $H_2 = 0.432$  m, respectively.

In the vertical plane at  $z = 0.074$  m from the sidewall, the distribution of  $k$  showed similar features as the distribution at the plane of symmetry, but the strengths of  $k$  in the crown zone as well as downstream of the crest were lower.

A comparison among the three planes leads to a number of observations. First, high levels of turbulence were closely related to conditions of flow separation triggered by the entrance lip curvature, crest curvature, and the deflector, although the levels of turbulence showed some differences in the lateral direction ( $z$  direction). Second, the crest's large curvature (equal to  $R_i^{-1} = 52.5 \text{ m}^{-1}$ ) caused a zone of high  $k$  values along the lower surface of the siphon conduit. Third, the curvature influence remained dominant even in the vicinity of the sidewall, where the levels of  $k$  did not drop much. Fourth, the influence of the sidewall reduced the strength of  $k$  in the near-crown region as well as downstream of the deflector.

The mechanisms for the generation of  $k$  and its distributions remained nearly the same at different model times when the upstream and downstream reservoirs reached different water levels. In the zone immediately downstream of the crest, turbulence kinetic energy was produced by intensified velocity shear near the lower surface. As water flowed over the deflector, the longitudinal flow path expanded and created transverse shear. For this reason, turbulence kinetic energy was produced. Examples of  $k$  distributions at two different model times are shown in Figures 5.18 and 5.19.

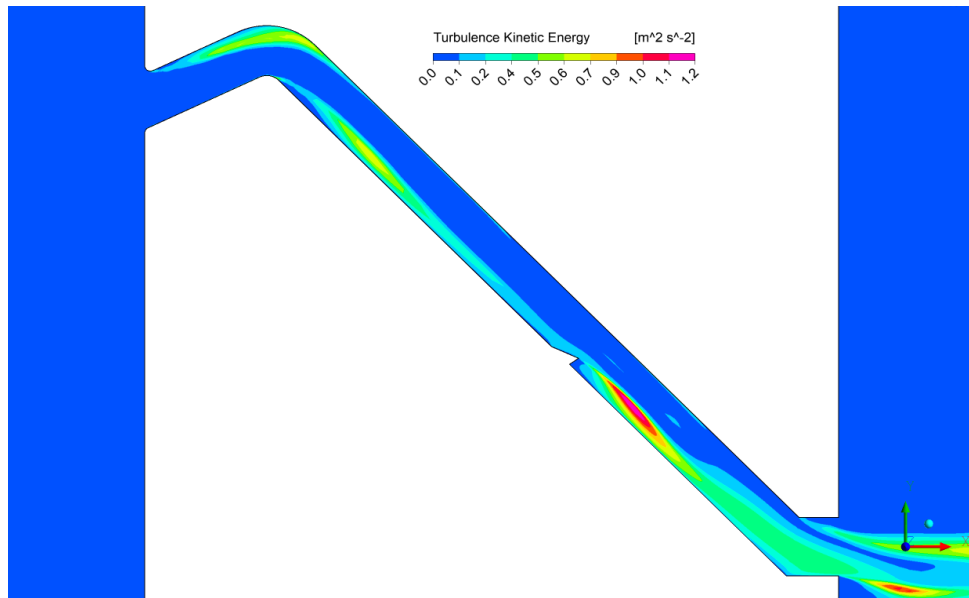


Figure 5-18. Vertical section at  $z = 0.125 \text{ m}$ , showing longitudinal distribution of  $k$ . The model time was  $t = 13 \text{ s}$ . The upstream and downstream reservoirs' water levels (Figure 4.1) were  $H_1 = 2.16 \text{ m}$ , and  $H_2 = 0.314 \text{ m}$ , respectively.

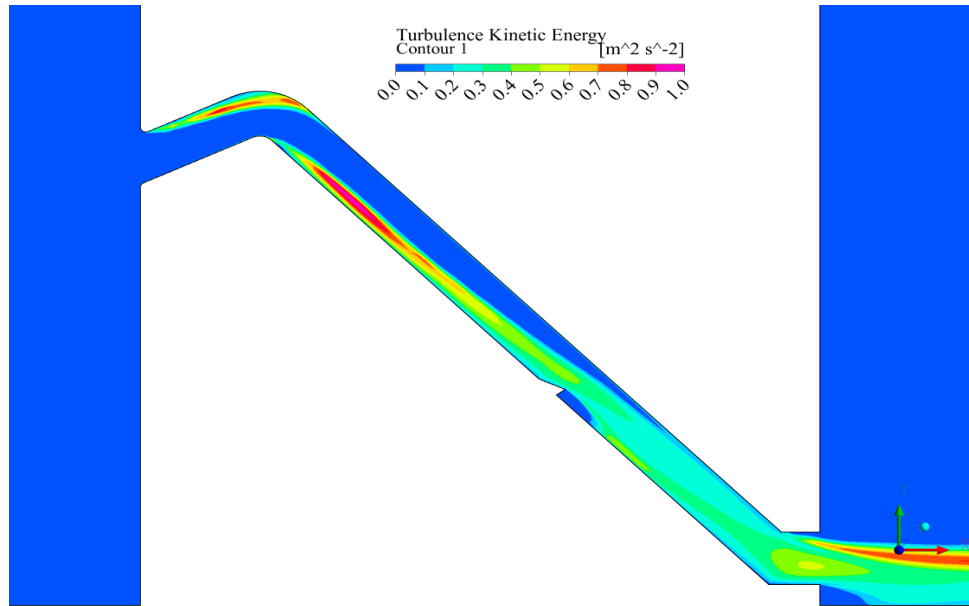


Figure 5-19. Vertical section at  $z = 0.125$  m, showing longitudinal distribution of  $k$ . The model time was  $t = 19$  s. The upstream and downstream reservoirs' water levels (Figure 4.1) were  $H_1 = 2.20$  m, and  $H_2 = 0.416$  m, respectively.

### 5.7.2 Cross-sectional distribution of turbulence kinetic energy

In Figures 5.20 to 5.24, the distributions of turbulent kinetic energy,  $k$ , in five different sections (as defined in Figure 5.4) of the siphon conduit are shown. The results are for run RN4 at a discharge of  $0.024 \text{ m}^3/\text{s}$ . In the upper leg of the siphon conduit, cross-sectional distribution of  $k$  (Equation 5.2) showed that turbulence was confined in the upper part of the conduit (Figures 5.20, 5.21) over the entire width from  $z = 0.0125$  m to the sidewall.

The flow contracted at the siphon entrance and the curved edges at the entrance affected the distribution of  $k$  in the upper leg. Fluids rotated in the upper part of the conduit (Figure 5-17). In the upstream cross-section (Figure 5-20) below the crown,  $k$  reached a maximum value of  $0.8 \text{ m}^2/\text{s}^2$ . The region between the main core of large  $k$  values and the lower siphon surface exhibited virtually negligible turbulence. This was because of the influence of the siphon entrance geometry. The distribution of  $k$  indicated that flow was more turbulence near the upper surface.

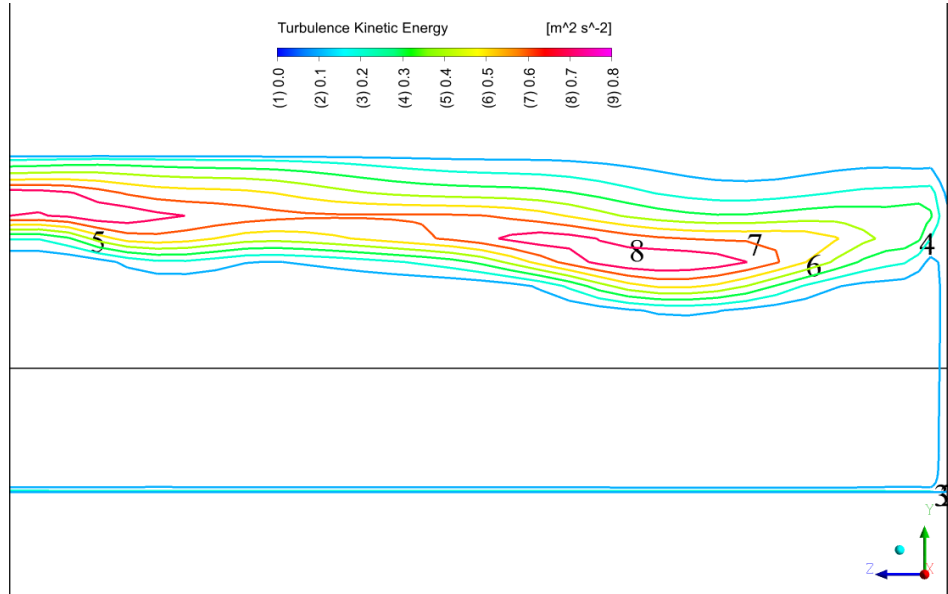


Figure 5-20. Distribution of  $k$  at cross-section P-00 (Figure 5.4). The left edges of the panel is the plane of symmetry, and the right edge is the sidewall.

At crest section P-C (Figure 5.21), the distribution of  $k$  was similar that at cross section P-00. The main core of high  $k$  values occurred under the crown and the peak value of  $k$  was located in two regions: one near the sidewall and the other close to the plane of symmetry.

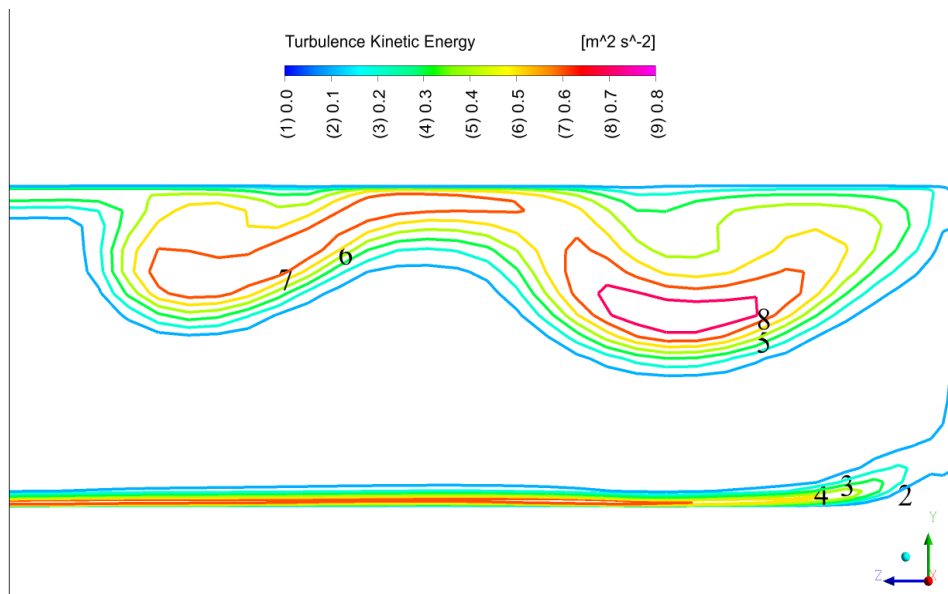


Figure 5-21. Distribution of  $k$  at cross-section P-C (Figure 5.4). Other remarks are the same as in Figure 5.20.

In Figure 5-22, the turbulence kinetic energy in cross section P-5 intersecting the lower surface of the siphon conduit at  $x = 1.79$  m is plotted. A large core of high  $k$  values formed near the lower surface of the siphon, specifically in the corner between the lower surface and the sidewall. The maximum  $k$  in this section was  $0.6 \text{ m}^2/\text{s}^2$  while the middle area experienced lowest values of  $k$ . At the same time, two cores of relatively high  $k$  values began to form upstream of the crown, extended up to this cross section until they vanished completely in further downstream cross sections along the siphon spillway. The distribution of  $k$  showed that turbulence was anisotropic throughout the flow depth.

Cross-section P-11 (Figure 5-23) intersects the lower surface of the siphon conduit at  $x = 1.98$  m. The cross section is sufficiently away from the crest. The turbulence kinetic energy was low, compared to those at the cross sections mentioned above. The two cores of high  $k$  values that appeared in the upper part of the previous upstream cross sections did not extend to this location. As for the lower part, the core of high  $k$  values was closer to the sidewall, and it grew and became larger, with turbulence kinetic energy reaching  $0.7 \text{ m}^2/\text{s}^2$  at the centre of the core.

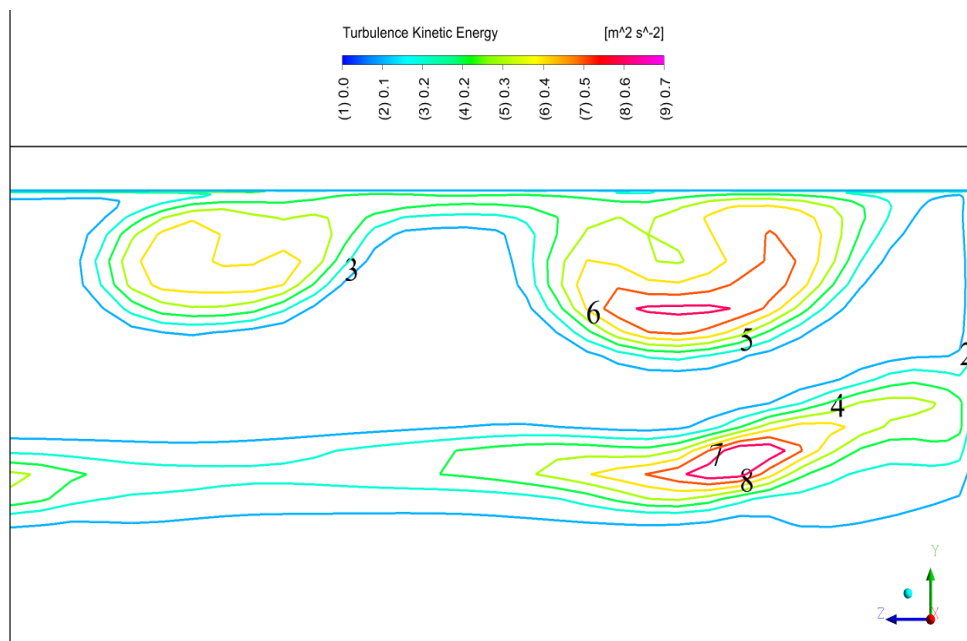


Figure 5-22. Distribution of  $k$  at cross-section P-5 (Figure 5.4). Other remarks are the same as in Figure 5.20.

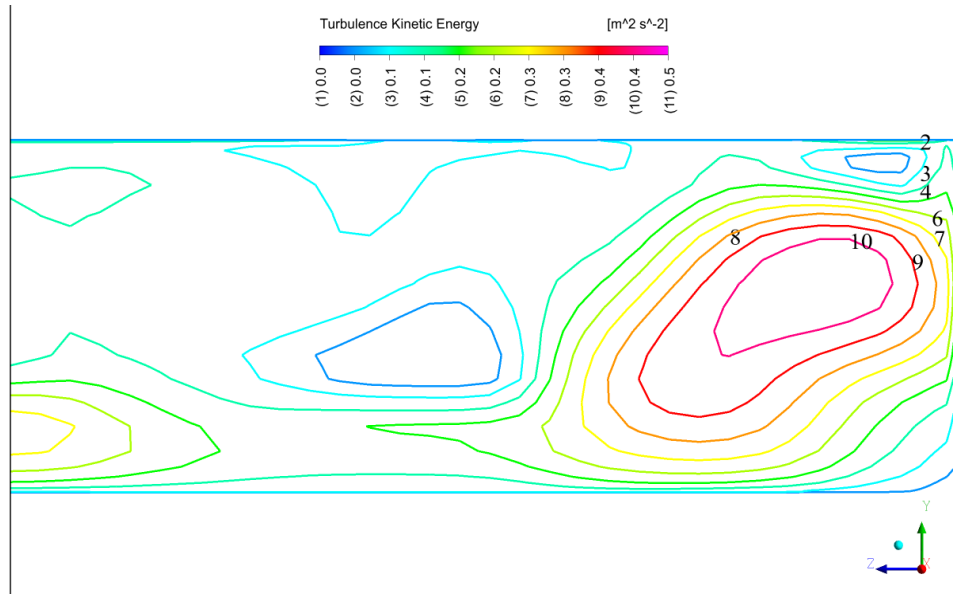


Figure 5-23. Distribution of  $k$  at cross-section P-11 (Figure 5.4). Other remarks are the same as in Figure 5.20.

After the curved boundary of the crest, turbulence kinetic energy represents the irregularity or randomness of the flow in zones close to the lower leg surface (Figures 5.22 and 5.23). It can be observed that turbulence kinetic energy values become small as water flowed along the siphon lower leg. The intensity of secondary flow reached a maximum value rapidly after the crest and weakens gradually downstream until the primary flow partly recovers before it is affected again by the deflector, leading to a sudden change in the flow patterns.

In Figure 5.24 (P-13), new cores of high  $k$  values appeared at the deflector on the lower surface of the siphon. The two main cores showed a maximum value of  $k = 0.6 \text{ m}^2/\text{s}^2$ . Also, a small core showed a value of  $k = 0.3 \text{ m}^2/\text{s}^2$  above the main core and close to the sidewall. In general, most high  $k$  value cores appear closer to the sidewall than to the plane of symmetry. At cross section P-13 after the deflector, the cross-sectional area of the flow at the deflector decreased, the flow velocity increased, and  $k$  was concentrated in the zone close to the lower surface of the conduit.

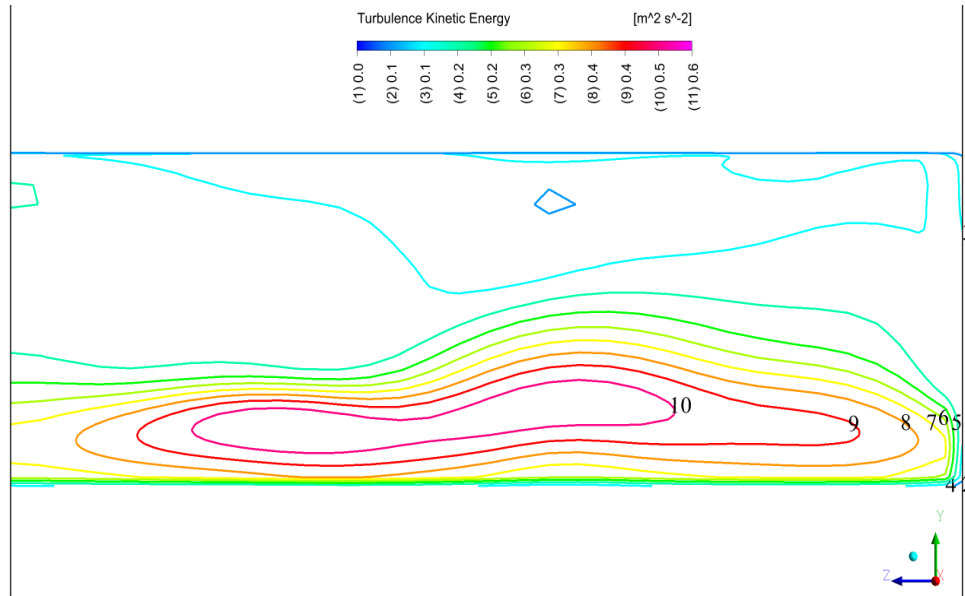


Figure 5-24. Distribution of  $k$  at cross-section P-13 (Figure 5.4). Other remarks are the same as in Figure 5.20.

Turbulence and secondary flow cause a loss of momentum resulting in wasted energy and reduce the efficiency of siphon discharge. The secondary flow extracts energy from the primary flow and uses it to rotate water mass.

## 5.8 Conclusions

This chapter presents detailed distributions of 3-D siphon flow velocity and turbulence kinetic energy. The distributions are very complicated and highly non-uniform in both the longitudinal and lateral direction. The following conclusions have been reached:

- The large curvature of the round lip of the siphon entrance causes the flow to separate from the upper surface of the upper leg all the way to the crown. In this separation zone, water circulates in elongated eddy motions and velocity shear produces strong turbulence.
- The 3-D flow velocity reaches the maximum magnitude in the vicinity of the crest. The velocity magnitudes varied along the length of the siphon conduit. At any given cross section perpendicular to the length, the magnitudes were small near the upper and lower surfaces of the conduit.
- The large curvature of the crest causes the flow to separate from the lower surface of the lower leg of the siphon conduit. The result is elongated eddy motions, large velocity shear

and high turbulence production. To some extent the flow recovers some degree of uniformity with increasing distance toward downstream.

- Further downstream at the deflector, the flow experiences a sudden expansion, giving rise to eddy motion, velocity shear, and hence turbulence.
- At most cross sections, the 3-D velocity exhibits rapidly varied magnitudes from point to point. The lowest magnitude occurs typically at the centre of the strongest secondary flow eddy.
- At most cross section, secondary flows show complicated structures with multiple eddies. The strength of the maximum secondary flow velocity relative to the maximum 3-D flow velocity at some cross sections reach 16%. The secondary flows reduce the discharge efficiency.
- The mechanisms for the generation of  $k$  and its distributions remain the same at different water levels in the upstream and downstream reservoirs. Turbulence kinetic energy is produced by intensified velocity shear at the entrance, crest and deflector.

# Chapter Six

## 6. Conclusions

### 6.1. Discussions and conclusions

Frequent, intense extreme weather events under climate change have been causing extra stresses on safe and efficient operations of reservoirs. The increase in the intensity and frequency of extreme rainfall events will probably cause more frequent flooding (Liuzzo and Freni, 2015). The projections provided by climate models indicate that the chance of occurrence of heavy rainfall is increasing due to climate change and the increasing greenhouse gases emission (Mailhot and Duchesne, 2010). Because the design of existing hydraulic systems was based on a statistical analysis of hydrological data for past events, it is important to restudy these structures under the new conditions. It is ever more important to improve the design of new spillways and rehabilitate existing spillways, which are an essential component of reservoir dam structures. These structures provide flood protection and support water resources developments. Among spillways, a siphon spillway is attractive because it is an ungated type of spillways and thus there is no need for human actions to control the flow. Water flows from an upstream reservoir through a siphon spillway to a downstream open channel. Flow through the siphon can be free flow or submerged exit flow, depending on the downstream water level. When the flow passes the curved surface of the siphon crest, there are large changes to the flow velocity and pressure. An increase in velocity in the crest region may cause the pressure to drop below the water vapour pressure, with risks of structure damage by cavitation.

A siphon spillway can pass large amounts of water with a small increase of the reservoir water level. Because of climate change, many siphon spillways have operated or will operate soon in submerged exit conditions, caused by a rise in the downstream water level. The submergence of siphon exits will lead to changes of the characteristics of flow through a siphon spillway. This creates an emerging issue, not dealt with in previous studies of siphon flow. Therefore, for the safety of reservoir dams and surrounding areas, it is important to study siphon flow in submerged exit conditions.

Previous experimental and numerical studies of siphons are limited to free discharge conditions. They create valuable knowledge about the mechanism of siphon functioning and flow characteristics. The flow through the siphon goes through four transitional stages before it reaches the state of full flow where the siphon conduit is completely filled with water, either due to the submergence of the exit or the use of a deflector (Head, 1971). In free discharge flow, the discharge coefficient is influenced by the geometry of the siphon (Tadayon and Ramamurthy, 2013). With regard to numerical modelling of siphon flow, the k- $\epsilon$  model of turbulence is reportedly suitable for predictions of siphon flow. The Dressler equation describes adequately the curvilinear flow over a circular crest (Ramamurthy and Vo, 1993). However, it is known how well the above-mentioned results apply to siphon flows in submerged exit conditions. The thesis research has contributed to filling a knowledge gap about siphon flows.

The flow along the crest surface is a curvilinear flow. This is a fundamental problem in fluid mechanics. In the discipline of hydraulic engineering, the flow characteristics in the crest region are of particular importance to the design of siphons. Chapters three to five of this thesis provide detailed discussions of the methods and results of curvilinear flow. The results are useful for assessing the hydraulic performance of siphons and the differences in performance between free discharge and submerged exit conditions, leading to improved design and operations of siphon spillways.

This thesis research uses a combined approach of numerical computations with laboratory experiments. The numerical computations extend the experimental results in an efficient, cost-saving manner, and produce results of detailed flow variables and structures that are difficult to observe in experiments. For the laboratory experiments, a scaled model siphon is designed and installed in the laboratory flume. The experiments produce discharge coefficients of submerged exit siphon flows. The numerical computations of three-dimensional two-phase flow predict the mean-flow velocity field, pressure field and turbulence quantities. The computations use RNG k- $\epsilon$  model for turbulence closure and the volume of fluid method for tracking the free water surface in the upstream and downstream reservoirs.

The findings from this thesis research are summarised in Chapters three to five. Highlights of the finding can be stated as follows:

- On the basis of laboratory experiments, the discharge coefficient is determined from measurements of discharges and water levels in the upstream reservoir and downstream

flume channel. The siphon discharge coefficient in submerged flow conditions ranges from 0.62 to 0.67. This is somewhat larger than the discharge coefficient in free flow conditions. The reported values of discharge coefficient may be used for the practical purpose of accessing the discharge capacity of a siphon spillway, at a given energy head.

- The numerical computations give discharge coefficients in a reasonable agreement with the experimental values of discharge coefficient. Therefore, the computational model discussed in the thesis may be used to study prototype siphons.
- With regard to flow characteristics, water flows uniformly from the reservoir toward the siphon entrance. At the entrance, flow streamlines contract and continue toward the crest. At the crest, the flow contracts again, and the centrifugal force affects the flow prior to flow development downstream.
- At the crest, the flow velocity increases with distance above the siphon crest, reaches the maximum at a small distance from the crest and then decreases towards the crown. The computed velocity distributions are significantly more accurate than the velocity distributions from the potential flow theory. The numerical computations cover the boundary layers along the upper and lower surfaces of the siphon conduit, but the potential flow theory does not.
- Secondary flow and turbulence exist at most cross sections along the siphon conduit. They are more profound in three main locations: in the vicinity of the crest, downstream the crest, and behind the deflector. Both secondary flow and turbulence reduce the efficiency of siphon discharge, and thus they should be minimised in the design/rehabilitation of siphon spillways.
- On the basis numerical computations, there are negative pressures in the crest region. The pressure decreases correspond to the increase of flow velocity. Negative pressures near the crest surface may drop below water vapour pressure at the prototype scale and can lead to the problem of cavitation. At the laboratory scale, it is not usual to have negative pressures to the extent of causing cavitation. Negative pressures at the prototype are much larger and problematic.

The originality of this research lies in the treatment of a new issue facing designers and operators of siphon spillways under climate change. The main contributions of this research are: 1) the creation of new knowledge about the siphon discharge coefficient and flow characteristics,

and 2) the identification of proper computational tools for predicting flows through siphons with similar geometry and structures.

One of the challenges/issues with using a scaled model siphon in the laboratory is unmatched dimensionless parameters with the prototype. The results from this thesis research have small values of the Froude number for the upstream reservoir, compared to negligible values in real world reservoirs. Also, the results have values of the Reynolds number for the flow through the model siphon conduit, which are lower than the values through typical siphons in real world reservoir dams. The lower values of the Reynolds number may have led to over-predictions of the boundary layer thickness along the solid surfaces of the siphon conduit. The unmatching dimensionless parameters are a limitation of this study, but their influence on the reported siphon discharge coefficient is not expected to be significant. The reason is that it is the geometry and curvature that have the dominant influence in the problem of siphon flows. This thesis research shows that the flow is sensitive to the submergence level, the shape of siphon entrance, the crest radius, and the presence of the deflector. This extensive list of influence factors makes it difficult to find universal graphs or empirical equations to determine the discharge coefficient and characteristics of siphon flows.

## **6.2. Further studies**

On the basis of the foregoing discussions and conclusions, the following recommendations are made to further investigate:

- the effects of various entrance shapes and crest radii on energy losses and thus on the efficiency of siphons, by means of laboratory experiments and numerical computations.
- the suitability of RNG  $k-\varepsilon$  model of turbulence for different siphon geometries and a variety of flow conditions.
- the dynamic and kinematic details of separation zones, which numerical computations would be the most suitable and cost-effective tools.
- Study cavitation potential.

In connection with cavitation potential, this study has shown cases of high flow velocity and low pressure over the spillway surface. At prototype scale, if the pressure drops significantly and below the water vapor pressure, the risk of cavitation becomes very likely and causes damage to the spillway. The collapsing of cavities can cause light to significant damages such as flow

modification, loss of materials, noise, structure vibration or failure, and even dam instability (Rahmeyer 1981). Over time, the damage in structures becomes so large that repair costs are very high. Therefore, it is important to limit the chance of cavitation occurrences. Falvey (1990) reported a case of damage to the Glen Canyon Dam Left Spillway Tunnel, forming a big hole of 11 m deep in the spillway. Cavitation in spillways is an important engineering safety issue.

Further study should continue the efforts made by previous researchers, who have attempted to predict cavitation in spillways and measure the level of cavitation damage by relating flow velocity and pressure with cavitation in spillways. It is worth giving highlights of the existing approach to investigating cavitation. A dimensionless parameter used to specify cavitation can be derived from Bernoulli's equation (Falvey 1990), which is known as the cavitation index  $\sigma = 2(P_o - P_v)/(\rho V_o^2)$ , where  $P_o$  is reference pressure,  $P_v$  is the vapor pressure,  $\rho$  is the density of water, and  $V_o$  is the reference velocity. It is clear that the governing parameters that control cavitation are the flow velocity, absolute pressure, and critical pressure. Foerster and Anderson (1969) built a 1:80 scale model of a real spillway. They identified the negative pressure on the carved boundary of the spillway as the source of the cavitation, and observed cavitation in the model at a flow velocity of 40 m/s. There is a knowledge gap in predictions of cavitation damage on spillways. Lee and Hoopes (1996) proposed a cavitation model using fuzzy mathematics, involving four different parameters related to cavitation index, flow velocity, material strength and operating time.

This study has provided details of flow separation. Investigations of cavitation damage should consider the influence of not only high velocity and low pressure, but also of flow separation (Rahmeyer 1981). Other influence conditions include the geometries of spillway entrance, exit, and crest. To control or eliminate damages, the strategies should focus on reducing the velocity, increasing the local pressure, streamlining, and smoothening the flow surface, and aerating the flow in the critical region.

This study has also given detailed predictions of flow velocity and pressure at different locations along the spillway. Such predictions may be used to give reference velocity and pressure values for calculations of the cavitation index  $\sigma$ . Falvey (1990) calculated  $\sigma$  for estimates of cavitation damage to a tunnel spillway. Falvey (1990) assumed a rapidly increase in damage with time of operation at high velocity, used historical records of flow through the spillway, and obtained empirical a relationship for estimates of the time before damage occurrence. The

estimates were given as a function of location and duration of spillway operation. Falvey (1990) showed surface irregularities, gate slots, and sudden changes in flow alignment as the typical source, which cause damages in a short distance downstream of the cavitation source. The damages do not progress upstream of the source. Falvey (1990) indicated that  $\sigma$  had a typical value of about 1.8; when  $\sigma > 1.8$ , cavitation would not occur; otherwise, cavitation would occur, and the extent of cavitation increased with decreasing  $\sigma$  values. To control cavitation, the study suggests generating a constant cavitation number spillway by changing the boundary (spillway surface) curvature and reducing flow velocity by increasing the surface friction.

This study has not addressed the effect of surface roughness. The effect of roughness on cavitation damage was experimentally investigated in Nie (2001). The experiments used copper wires of 0.24, 0.38, and 0.58 mm in diameter as surface roughness elements in a 17-cm wide Plexiglas model spillway. No cavitation damage occurred downstream of the rough surface, while cavitation did occur downstream of the smooth surface in the absence of roughness elements. The pressure behind the irregularity (wires) was affected by the curved surface due to the influence of centrifugal forces and by the vortex behind the irregularity. Also, turbulence increased as a result of the irregularity. Wan and Raza (2018) reported boundary irregularity as a mechanism of cavitation in a chute spillway. In a prototype-scale study of cavitation damage in a newly resurfaced spillway, Yusuf and Micovic (2020) compared the difference between the new smooth surface and previous rough surface and proposed a design with increased minimum pressures.

For the siphon spillway dealt with in this study, select three locations for evaluations of the cavitation index  $s$ : a short distance upstream of the crest at  $x = 1.66$  m, the crest at  $x = 1.644$  m, and a short distance downstream of the crest at  $x = 1.63$  m. Using the centreline maximum velocities and minimum pressures (Figure 4.19 shows the minimum pressure value) at model time  $t = 22.8$  s as reference values gives  $\sigma \approx 6$  at the location  $x = 1.63$  m and  $\sigma = 2.7$  at the other two locations. This model time ( $t = 22.8$  s) was selected for the evaluations of the index  $\sigma$ , because the velocity value at  $t = 22.8$  s and at the centerline of the crest is the maximum computed velocity value in this study.

Although there was a significant decrease in  $\sigma$  values along the crest surface, the values did not drop low enough and thus no cavitation would not occur in the laboratory size model. At prototype scale, it is possible for cavitation to occur, given that negative pressures were seen from the computational results. The negative pressure head will grow in linear scale in the prototype.

For instance, if the prototype-scale siphon is ten times larger than the model size, the negative pressure head will be ten times of the computed negative pressure. It is worth noting that the minimum pressure cannot drop below the vapor pressure where the vapor pressure prevents it from a further drop. In serious cavitation, two main dangers are expected: vibration, and resonance. Where there is resonance, even a small force in that area can make the structure to collapse. Therefore, it is very important to address the phenomena of cavitation.

## 7. References

- Ali, K.H.M. and Pateman, D., 1980. Theoretical and experimental investigations of air-regulated siphons. *Proceedings of the Institution of Civil Engineers*, 69(1), pp. 111-138.
- Babaeyan-Koopaei, K., Valentine, E.M. and Ervine, D.A., 2002. Case study on hydraulic performance of Brent Reservoir siphon spillway. *Journal of Hydraulic Engineering*, 128(6), pp. 562-567.
- Bos, M.G., 1976. Discharge measurement structures. Publication No. 161, Delft Hydraulic Laboratory, Delft, the Netherlands.
- Cassidy, J.J., 1965. Irrotational flow over spillways of finite height. *Journal of the Engineering Mechanics Division*, 91(6), pp. 155-173.
- Cassidy, J.J., 1970. Designing spillway crests for high-head operation. *Journal of the Hydraulics Division*, 96(3), pp. 745-753.
- Castro-Orgaz, O., 2008. Curvilinear flow over round-crested weirs. *Journal of Hydraulic Research*, 46(4), pp. 543-547.
- Chow, V.T., 1959. *Open-channel hydraulics*. McGraw-Hill, Caldwell, New Jersey.
- Coleman, H.W., Wei, C.Y. and Lindell, J.E., 2004. Hydraulic design of spillways. *Hydraulic design handbook*, pp.17-41. McGraw-Hill
- Dressler, R.F., 1978. New nonlinear shallow-flow equations with curvature. *Journal of Hydraulic Research*, 16(3), pp. 205-222.
- Ervin, D.A. and Oliver, G.C.S., 1980. The full-scale behaviour of air-regulated siphon spillways. *Proceedings of the Institution of Civil Engineers*, 69(3), pp. 687-706.
- Falvey, H.T., 1990. *Cavitation in chutes and spillways*. Denver: US Department of the Interior, Bureau of Reclamation.

Ferziger, J.H., Perić, M. and Street, R.L., 2002. Computational methods for fluid dynamics (Vol. 3, pp. 196-200). Springer, Berlin

Foerster, K.E. and Anderson, A.G., 1969. Model Study of the Spillway of the Reza Shah Kabir Project Khuzestan Water and Power Authority Ministry of Water and Power-Government of Iran.

Frizell, K.W., Renna, F.M. and Matos, J., 2013. Cavitation potential of flow on stepped spillways. *Journal of Hydraulic Engineering*, 139(6), pp.630-636.

Gribbin, J.E., 2013. *Introduction to Hydraulics & Hydrology: With Applications for Stormwater Management*. Nelson Education. Hager, W.H. and Bremen, R., 1988. Plane gate on standard spillway. *Journal of Hydraulic Engineering*, 114(11), pp. 1390-1397.

Head, C.R., 1971. A self-regulating river siphon. *Journal of Institution of Water Engineers*, 25(1), pp. 63-72.

Head, C.R., 1975. Low-Head Air Regulated Siphons. *Journal of the Hydraulics Division*, 101(3), pp. 329-345.

Hirt, C.W. and Nichols, B.D., 1981. Volume of fluid (VOF) method for the dynamics of free boundaries. *Journal of Computational Physics*, 39(1), pp. 201-225.

Houghtalen, R.J., Osman, A. and Hwang, N.H., 2017. *Fundamentals of hydraulic engineering systems*. Fifth edition. Prentice Hall, Hoboken, New Jersey.

Jones, W.P. and Launder, B.E., 1972. The prediction of laminarization with a two-equation model of turbulence. *International Journal of Heat and Mass Transfer*, 15(2), pp. 301-314.

Kermani, E.F., Barani, G.A. and Hesaroeeyeh, M.G., 2018. Cavitation damage prediction on dam spillways using Fuzzy-KNN modeling. *J Appl Fluid Mech*, 11(2), pp.323-329.

Khatsuria, R.M., 2004. *Hydraulics of spillways and energy dissipators*. CRC Press, Boca Raton, Florida.

Launder, B.E. and Spalding, D.B., 1974. The numerical computation of turbulent flows. *Computer Methods in Applied Mechanics and Engineering*, 3(2), pp. 269-289.

Lee, W. and Hoopes, J.A., 1996. Prediction of cavitation damage for spillways. *Journal of Hydraulic Engineering*, 122(9), pp.481-488.

Linsley, R.K. and Franzini, J.B., 1964. *Water-resources engineering*. McGraw-Hill, Highstown, New Jersey 08520

Liuzzo, L. and Freni, G., 2015. Analysis of extreme rainfall trends in sicily for the evaluation of depth-duration-frequency curves in climate change scenarios. *Journal of Hydrologic Engineering*, 20(12), p.04015036.

Mailhot, A. and Duchesne, S., 2010. Design criteria of urban drainage infrastructures under climate change. *Journal of Water Resources Planning and Management*, 136(2), pp.201-208.

Nie, M.X., 2001. Cavitation prevention with roughened surface. *Journal of Hydraulic engineering*, 127(10), pp.878-880.

Peltier, Y., Dewals, B., Archambeau, P., Piroton, M. and Erpicum, S., 2018. Pressure and velocity on an ogee spillway crest operating at high head ratio: experimental measurements and validation. *Journal of Hydro-environment Research*, 19, pp. 128-136

Pope, S.B., 2001. *Turbulent flows*. Cambridge University Press, Cambridge, U.K.

Rahmeyer, W.J., 1981. Cavitation damage to hydraulic structures. *Journal-American Water Works Association*, 73(5), pp.270-274.

Ramamurthy, A.S. and Vo, N.D., 1993. Application of Dressler theory to weir flow. *Journal of Applied Mechanics*, 60, pp. 163-166.

Ramamurthy, A.S., Vo, N.D. and Balachandar, R., 1994. A note on irrotational curvilinear flow past a weir. *Journal of Fluids Engineering*, 116(2), pp. 378-381.

Johnson, N. K. and Richardson, L. F., 1922. Weather Prediction by Numerical Process. *The Mathematical Gazette*, 11(159), pp. 125–125. Doi: 10.2307/3603284.

Savage, B.M. and Johnson, M.C., 2001. Flow over ogee spillway: Physical and numerical model case study. *Journal of Hydraulic Engineering*, 127(8), pp. 640-649.

Shih, T.H., Liou, W.W., Shabbir, A., Yang, Z. and Zhu, J., 1995. A new k- $\epsilon$  eddy viscosity model for high Reynolds number turbulent flows. *Computers & Fluids*, 24(3), pp. 227-238.

Schlichting, H. and Gersten, K., 2000. *Boundary-Layer Theory*. Springer, Berlin

Tadayon, R. and Ramamurthy, A.S., 2013. Discharge coefficient for siphon spillways. *Journal of Irrigation and Drainage Engineering*, 139(3), pp. 267-270.

Tennekes, H. and Wyngaard, J.C., 1972. The intermittent small-scale structure of turbulence: data-processing hazards. *Journal of Fluid Mechanics*, 55(1), pp. 93-103.

Tullis, B.P., 2011. Behavior of submerged ogee crest weir discharge coefficients. *Journal of Irrigation and Drainage Engineering*, 137(10), pp. 677-681.

USACE, 1990. *Hydraulic design of spillways*. Department of the Army Corps of Engineers, Washington, D.C. EM 1110-2-1603.

USBR, 1977. *Design of small dams*. U.S. Government Printing Office. Washington, D.C.

Vermeyen, T.B., Merritt, D.H. and Taylor, G.M., 1991. Design of high capacity spillways for Ritschard Dam, Colorado. In *Hydraulic Engineering* (pp. 394-399). ASCE.

Vermeyen, T.B., 1992. Uncontrolled ogee crest research. PAP-0609, U.S. Bureau of Reclamation.

Wan, W., Liu, B. and Raza, A., 2018. Numerical prediction and risk analysis of hydraulic cavitation damage in a High-Speed-Flow spillway. *Shock and Vibration*, 2018.

Wilcox, D.C., 1998. *Turbulence modeling for CFD*. DCW Industries, La Canada, CA.

Yakhot, V. and Orszag, S.A., 1986. Renormalization group analysis of turbulence. I. Basic theory. *Journal of Scientific Computing*, 1(1), pp. 3-51.

Yusuf, F. and Micovic, Z., 2020. Prototype-scale investigation of spillway cavitation damage and numerical modeling of mitigation options. *Journal of Hydraulic Engineering*, 146(2), p.04019057.

## 8. Appendix A: Data sheets of gauge pressures from numerical predictions.

Table A1. Comparison of predicted pressures between Runs RN2, RN3 and RN4. The cell sizes are 2, 3, and 4 mm, respectively. The  $(x, z)$  coordinates are (1.644, 0.125) m. Average Difference = -0.064

Vertical position	Pressure (Pa)			Difference
y (m)	RN4	RN2	RN3	$\delta p$ (%)
0.801	-304.070	-303.066	-285.976	0.001
0.801	-304.138	-303.122	-286.028	0.001
0.801	-304.183	-303.150	-286.073	0.001
0.801	-304.096	-303.161	-286.088	0.001
0.801	-303.664	-303.176	-286.041	0.000
0.802	-302.524	-303.132	-285.892	-0.001
0.802	-300.097	-302.997	-285.598	-0.003
0.803	-295.501	-302.734	-285.315	-0.007
0.804	-287.486	-302.300	-285.099	-0.015
0.805	-274.264	-301.644	-284.344	-0.027
0.807	-253.490	-300.702	-283.237	-0.047
0.811	-223.087	-299.396	-281.678	-0.075
0.814	-204.483	-297.631	-279.546	-0.092
0.815	-197.370	-295.302	-276.700	-0.097
0.819	-175.282	-292.283	-272.972	-0.115
0.822	-156.149	-288.433	-268.168	-0.131
0.826	-139.715	-283.588	-262.058	-0.142
0.830	-125.766	-277.556	-254.376	-0.150
0.834	-114.305	-270.118	-244.815	-0.154
0.837	-105.401	-261.024	-233.127	-0.154
0.841	-99.108	-250.056	-219.234	-0.149
0.845	-95.407	-237.130	-203.146	-0.140
0.849	-94.010	-222.238	-184.929	-0.127
0.851	-94.287	-205.520	-167.750	-0.110
0.853	-94.935	-203.618	-152.472	-0.107
0.854	-95.566	-190.301	-138.863	-0.093
0.854	-96.104	-176.504	-135.225	-0.079
0.855	-96.536	-163.959	-126.701	-0.067
0.855	-96.678	-152.525	-115.818	-0.055
0.855	-96.872	-142.082	-106.052	-0.045
0.855	-97.117	-132.526	-97.272	-0.035
0.855	-97.291	-123.755	-89.422	-0.026
0.855	-97.408	-123.486	-82.912	-0.026
0.855	-97.483	-115.681	-78.752	-0.018

Table A2. Data sheet of predicted velocity at  $(x, z) = (1.644, 0.125)$  m, for Runs SK4, RL4 and RN4.

X [ m]	Z [ m]	RL4 (Realizable k-ε model)		RN4 (RNG k-ε model)		SK4 (Standard k-ε model)	
		Y [ m]	Velocity u [ m s <sup>-1</sup> ]	Y [ m]	Velocity u [ m s <sup>-1</sup> ]	Y [ m]	Velocity u [ m s <sup>-1</sup> ]
1.64	0.125	0.808	0.000977	0.808	0.00095	0	0
1.644	0.125	0.808	1.140364	0.808	1.108663	0.807485	1.171901
1.644	0.125	0.8081	2.124045	0.8081	2.09955	0.80751	2.150323
1.644	0.125	0.8082	2.769323	0.8082	2.769809	0.807551	2.76084
1.644	0.125	0.8082	3.150078	0.8082	3.176622	0.807616	3.077611
1.644	0.125	0.80845	3.356615	0.8084	3.410209	0.807877	3.232089
1.644	0.125	0.8086	3.427461	0.8086	3.507046	0.80813	3.302884
1.644	0.125	0.809	3.426883	0.809	3.519639	0.808328	3.316268
1.644	0.125	0.8097	3.379198	0.8097	3.475791	0.808527	3.328507
1.644	0.125	0.8106	3.268698	0.8106	3.372663	0.809149	3.310427
1.644	0.125	0.8121	3.092074	0.8121	3.205261	0.810133	3.242248
1.644	0.125	0.8146	2.864822	0.8146	2.993662	0.811686	3.118421
1.644	0.125	0.8184	2.623842	0.8184	2.779063	0.813724	2.977605
1.644	0.125	0.8245	2.421198	0.8224	2.605346	0.814136	2.947328
1.644	0.125	0.8264	2.258187	0.8264	2.474078	0.817981	2.758482
1.644	0.125	0.8304	2.111808	0.8304	2.369442	0.822081	2.597198
1.644	0.125	0.8344	1.962091	0.8344	2.262717	0.822428	2.586655
1.644	0.125	0.8384	1.789354	0.8384	2.070995	0.826149	2.470631
1.644	0.125	0.8424	1.57708	0.8424	1.668516	0.830209	2.368815
1.644	0.125	0.8465	1.331756	0.8465	1.156381	0.834266	2.264305
1.644	0.125	0.8505	1.079234	0.85	0.720249	0.83798	2.092067
1.644	0.125	0.8545	0.845178	0.854	0.375335	0.838318	2.076368
1.644	0.125	0.8584	0.660749	0.8584	0.128919	0.84234	1.6759
1.644	0.125	0.8609	0.551554	0.86	-0.01126	0.846375	1.153891
1.644	0.125	0.8625	0.495817	0.8625	-0.08791	0.850401	0.706839
1.644	0.125	0.8635	0.464826	0.8635	-0.13373	0.854426	0.360168
1.644	0.125	0.8641	0.427469	0.864	-0.1683	0.858365	0.11603
1.644	0.125	0.8645	0.371037	0.8645	-0.19786	0.86085	-0.02229
1.644	0.125	0.8647	0.300944	0.8648	-0.21525	0.862423	-0.09753
1.644	0.125	0.8649	0.215493	0.864	-0.20595	0.863415	-0.1422
1.644	0.125	0.865	0.128225	0.865	-0.16069	0.864041	-0.17567
1.644	0.125	0.8651	0.06251	0.8651	-0.09769	0.864436	-0.20387
1.644	0.125	0.8651	0.023362	0.8651	-0.04267	0.864686	-0.21913
1.644	0.125	0.8652	0	0.865	0	0.864844	-0.20671

Table A3. Data sheet of predicted pressure at  $(x, z) = (1.644, 0.125)$  m, for Runs SK4, RL4 and RN4.

X [ m]	Y [ m]	Z [ m]	(Realizable k-ε model)		(RNG k-ε model)		(Standard k-ε model)	
			RL4		RN4		SK4	
			Pressure [ Pa]	Velocity [ m s <sup>-1</sup> ]	Pressure [ Pa]	Velocity [ m s <sup>-1</sup> ]	Pressure [ Pa]	Velocity [ m s <sup>-1</sup> ]
1.6400	0.8080	0.125	-5008.480	0.0010	-5112.455	1.1092	-4595.9844	1.2067
1.6440	0.8081	0.125	-5007.592	1.1404	-5105.067	2.1011	-4590.3936	2.2188
1.6440	0.8081	0.125	-5000.268	2.1240	-5082.069	2.7721	-4570.2354	2.8487
1.6440	0.8082	0.125	-4977.467	2.7693	-5031.679	3.1794	-4527.5215	3.1731
1.6440	0.8083	0.125	-4927.813	3.1501	-4938.955	3.4133	-4452.4517	3.3278
1.6440	0.8084	0.125	-4837.501	3.3566	-4786.580	3.5101	-4331.2002	3.3942
1.6440	0.8087	0.125	-4690.666	3.4275	-4554.192	3.5225	-4239.4146	3.4032
1.6440	0.8090	0.125	-4465.590	3.4269	-4217.264	3.4782	-4143.5796	3.4111
1.6440	0.8097	0.125	-4134.574	3.3792	-3758.076	3.3744	-3867.4094	3.3801
1.6440	0.8106	0.125	-3678.043	3.2687	-3185.194	3.2063	-3489.6548	3.2954
1.6440	0.8122	0.125	-3098.217	3.0921	-2544.033	2.9940	-3012.1440	3.1537
1.6440	0.8146	0.125	-2430.386	2.8648	-1943.444	2.7792	-2555.1030	2.9997
1.6440	0.8184	0.125	-1788.862	2.6238	-1495.768	2.6054	-2458.3796	2.9672
1.6440	0.8224	0.125	-1306.129	2.4212	-1172.959	2.4743	-1911.4460	2.7683
1.6440	0.8264	0.125	958.9194	2.2582	-926.1035	2.3700	-1488.6154	2.6031
1.6440	0.8304	0.125	-698.6908	2.1118	-730.5942	2.2638	-1462.4833	2.5925
1.6440	0.8344	0.125	-500.2492	1.9621	-576.4684	2.0730	-1176.0344	2.4756
1.6440	0.8384	0.125	-350.9824	1.7894	-480.4298	1.6716	-935.1725	2.3740
1.6440	0.8425	0.125	-247.2240	1.5771	-453.9359	1.3318	-743.4783	2.2701
1.6440	0.8465	0.125	-185.9019	1.3318	-471.1523	1.0792	-605.1591	2.0987
1.6440	0.8505	0.125	-159.9541	1.0792	-505.1157	0.8452	-592.5576	2.0831
1.6440	0.8545	0.125	-159.4975	0.8452	-540.7734	0.6607	-496.1658	1.6835
1.6440	0.8584	0.125	-173.5665	0.6607	-565.4051	0.5516	-469.0316	1.3318
1.6440	0.8609	0.125	-188.7291	0.5516	-579.9672	0.4958	-487.3395	1.0792
1.6440	0.8625	0.125	-199.5704	0.4958	-588.5323	0.4648	-521.2465	0.8452
1.6440	0.8635	0.125	-206.2093	0.4648	-593.6945	0.4275	-556.5493	0.6607
1.6440	0.8641	0.125	-210.1563	0.4275	-597.0326	0.3710	-581.0039	0.5516
1.6440	0.8645	0.125	-212.8741	0.3710	-599.2614	0.3009	-595.5778	0.4958
1.6440	0.8648	0.125	-214.8666	0.3009	-600.7203	0.2155	-604.2081	0.4648
1.6440	0.8649	0.125	-216.2614	0.2155	-601.6699	0.1282	-609.4362	0.4275
1.6440	0.8650	0.125	-217.2061	0.1282	-602.2899	0.0625	-612.7798	0.3710
1.6440	0.8651	0.125	-217.8286	0.0625	-602.6918	0.0234	-614.9849	0.3009
1.6440	0.8651	0.125	-218.2308	0.0234	-602.9130	0.0000	-616.4181	0.2155
1.6440	0.8652	0.125	-218.4522	0.0000	-602.9130	0.0000	-617.3450	0.1282

Table A4. Values of  $U$  for Run RN4 at different elevations in the crest region (Lines 2, 4 and 8).

Line 2		Line 8		Line 4	
Y/d	U/U <sub>max</sub>	Y/d	U/U <sub>max</sub>	Y/d	U/U <sub>max</sub>
14.05409	0.00047	14.05408	0	14.05408	0
14.05457	0.236411	14.05457	0.206697	14.05457	0.175605
14.05533	0.400233	14.05533	0.378796	14.05533	0.329089
14.05653	0.489335	14.05653	0.472085	14.05653	0.417909
14.05843	0.545437	14.05843	0.5297	14.05843	0.472405
14.06144	0.585583	14.06144	0.570324	14.06144	0.510731
14.06618	0.619063	14.06618	0.603157	14.06618	0.5414
14.07367	0.65255	14.07367	0.635123	14.07367	0.570464
14.08548	0.682078	14.08548	0.667696	14.08548	0.600604
14.10412	0.699442	14.10412	0.692468	14.10412	0.628964
14.12617	0.705584	14.12617	0.701271	14.12617	0.644212
14.13348	0.708097	14.13348	0.704688	14.13349	0.649602
14.17963	0.711497	14.17963	0.710167	14.17963	0.658406
14.23666	0.706376	14.23666	0.70446	14.23666	0.654825
14.25188	0.703485	14.25188	0.701682	14.25188	0.652928
14.3296	0.682929	14.3296	0.68267	14.3296	0.64103
14.35921	0.675282	14.35921	0.675479	14.35921	0.636776
14.40769	0.661554	14.40769	0.661233	14.40769	0.627988
14.43823	0.654431	14.43823	0.653722	14.43823	0.623287
14.48451	0.641698	14.48451	0.640834	14.48451	0.61491
14.53752	0.626174	14.53752	0.626085	14.53751	0.601572
14.56016	0.61889	14.56016	0.619224	14.56016	0.595254
14.63476	0.569846	14.63476	0.576832	14.63476	0.543462
14.66688	0.521707	14.66688	0.5304	14.66688	0.499082
14.70863	0.456938	14.70863	0.467437	14.70863	0.44004
14.78195	0.303057	14.78195	0.300567	14.78195	0.321725
14.84358	0.197418	14.84358	0.180184	14.84358	0.241577
14.85505	0.177922	14.85505	0.157951	14.85505	0.226818
14.92735	0.093242	14.92735	0.058338	14.92735	0.149421
14.9962	0.036443	14.9962	-0.01436	14.9962	0.089112
15.03984	0.003708	15.03984	-0.04998	15.03984	0.057809
15.06745	-0.01422	15.06745	-0.06856	15.06745	0.039733
15.08493	-0.02475	15.08493	-0.07897	15.08493	0.028502
15.09598	-0.03134	15.09598	-0.08499	15.09598	0.021077
15.10297	-0.03646	15.10297	-0.08886	15.10297	0.01444
15.10739	-0.04076	15.10739	-0.09003	15.10739	0.007272
15.11019	-0.04244	15.11019	-0.08512	15.11019	-0.00037
15.11196	-0.03798	15.11196	-0.06914	15.11195	-0.00654
15.11307	-0.0262	15.11307	-0.04374	15.11307	-0.00761
15.11378	-0.0122	15.11378	-0.01862	15.11378	-0.0043
15.11423	0	15.11423	0	15.11423	-4.4E-06

Table A5. Values of  $U$  for Run RN4 at different elevations above the crest (Lines 1, 7 and 9).

Line 1		Line 7		Line 9	
Y/d	U/Umax	Y/d	U/Umax	Y/d	U/Umax
14.13945	0	14.13945	0.000282	14.13945	0.000132
14.13945	0.433554	14.13988	0.377622	14.13988	0.129549
14.13945	0.701316	14.14057	0.668638	14.14057	0.296207
14.13945	0.822807	14.14166	0.79478	14.14166	0.421097
14.13945	0.906984	14.14339	0.881911	14.14339	0.514704
14.13945	0.962725	14.14611	0.940552	14.14611	0.594344
14.13945	0.992173	14.15042	0.972953	14.15042	0.661577
14.13945	1.000206	14.15722	0.984913	14.15722	0.708971
14.13945	0.987015	14.16798	0.978832	14.16798	0.737611
14.13945	0.951981	14.18498	0.950694	14.18498	0.753519
14.13945	0.900539	14.21184	0.903533	14.21184	0.754352
14.13945	0.83838	14.25428	0.843863	14.25428	0.736932
14.13945	0.775864	14.32133	0.774825	14.32133	0.70412
14.13945	0.724081	14.39135	0.722024	14.39135	0.673979
14.13945	0.685122	14.46138	0.682755	14.46138	0.648259
14.13945	0.654591	14.53141	0.652272	14.53141	0.62586
14.13945	0.621628	14.60144	0.622146	14.60144	0.597673
14.13945	0.557987	14.67147	0.565144	14.67147	0.535264
14.13945	0.436914	14.74151	0.441319	14.74151	0.431259
14.13945	0.299919	14.81154	0.288169	14.81154	0.328022
14.13945	0.192934	14.88158	0.165736	14.88158	0.24935
14.13945	0.1102	14.95162	0.068662	14.95162	0.184149
14.13945	0.050781	15.02125	-0.00832	15.02125	0.126817
14.13945	0.015417	15.06515	-0.04584	15.06515	0.093388
14.13945	-0.00433	15.09284	-0.06499	15.09284	0.071759
14.13945	-0.01613	15.1103	-0.07558	15.1103	0.056707
14.13945	-0.02361	15.12132	-0.08174	15.12132	0.045697
14.13945	-0.02951	15.12827	-0.0859	15.12827	0.035476
14.13945	-0.03478	15.13266	-0.08775	15.13266	0.024491
14.13945	-0.03807	15.13543	-0.08427	15.13543	0.012467
14.13945	-0.03616	15.13717	-0.07018	15.13718	0.000276
14.13945	-0.02647	15.13828	-0.04561	15.13828	-0.00612
14.13945	-0.01284	15.13897	-0.01981	15.13897	-0.00472
14.13945	-4.7E-05	15.13941	-3.5E-05	15.13941	-9.2E-06

Table A6. Values of  $U$  for Run RN4 at different elevations in the crest region (Lines 3, 5 and 6).

Line 3		Line 5		Line 6	
Y/d	U/Umax	Y/d	U/Umax	Y/d	U/Umax
14.01069	-1.08497E-05	14.01069	0	14.01069	0
14.01131	-0.006697496	14.01131	-0.00498	14.01131	-0.00975
14.01181	-0.009117352	14.01181	-0.0085	14.01181	-0.01534
14.01229	-0.011481848	14.01229	-0.01196	14.01229	-0.02087
14.01385	-0.010528733	14.01385	-0.02072	14.01385	-0.0294
14.01632	-0.001222483	14.01632	-0.02973	14.01632	-0.03098
14.02024	0.017696631	14.02024	-0.03674	14.02024	-0.02338
14.02646	0.057335031	14.02646	-0.04094	14.02646	0.001427
14.03634	0.151363765	14.03634	-0.04323	14.03634	0.076923
14.052	0.349504011	14.052	-0.04476	14.052	0.271095
14.07367	0.56857336	14.07367	-0.04465	14.07367	0.528456
14.07677	0.600048246	14.07678	-0.04471	14.07677	0.563399
14.10091	0.690676311	14.10091	-0.03945	14.10091	0.672089
14.11442	0.712666027	14.11441	-0.02321	14.11442	0.705798
14.1311	0.717308943	14.1311	0.056563	14.1311	0.71388
14.16492	0.72167487	14.16492	0.308995	14.16492	0.722641
14.17039	0.721917051	14.17039	0.357556	14.17039	0.723405
14.20327	0.720013782	14.20327	0.54291	14.20327	0.720182
14.24737	0.714070019	14.24737	0.681218	14.24737	0.712212
14.25293	0.712985278	14.25293	0.691382	14.25293	0.710857
14.30094	0.700271257	14.30094	0.691093	14.30094	0.69698
14.33033	0.690617154	14.33033	0.685051	14.33033	0.686705
14.36619	0.679504361	14.3662	0.671246	14.36619	0.67507
14.40603	0.665730588	14.40603	0.656191	14.40603	0.660791
14.44738	0.653220944	14.44738	0.641213	14.44738	0.64805
14.48044	0.642514484	14.48044	0.629588	14.48044	0.637192
14.55162	0.619187266	14.55162	0.605526	14.55162	0.615211
14.55414	0.618306838	14.55414	0.604661	14.55414	0.614385
14.62689	0.573878811	14.62689	0.559843	14.62689	0.573531
14.69087	0.490532234	14.69087	0.483702	14.69087	0.488235
14.69961	0.478628294	14.69961	0.472918	14.69961	0.476048
14.77148	0.352158107	14.77148	0.370597	14.77148	0.335866
14.84341	0.240993005	14.84341	0.28817	14.84341	0.208484
14.88718	0.186170741	14.88719	0.250313	14.88719	0.145932
14.91508	0.151266866	14.91508	0.226069	14.91508	0.106044
14.98871	0.082340661	14.98871	0.171384	14.98871	0.020903
15.03492	0.041054388	15.03492	0.138339	15.03492	-0.021
15.06398	0.017915216	15.06398	0.11588	15.06398	-0.04219
15.08226	0.003954626	15.08226	0.099303	15.08226	-0.0537
15.09377	-0.004878331	15.09377	0.08655	15.09377	-0.06044
15.10101	-0.010666521	15.10101	0.074882	15.10101	-0.06526
15.10557	-0.015664762	15.10557	0.061962	15.10557	-0.0683

Table A7. Vertical distributions of pressure from the siphon crest to crown in the centreline at  $z = 0.125$  m

Pressure [ Pa]	Pressure [ atm]	$P/\gamma$ [m]	y [ m]	y/d
-18,200	-0.180	-1.850	0.808	14.100
-18,200	-0.179	-1.850	0.808	14.100
-18,100	-0.179	-1.850	0.808	14.100
-18,000	-0.178	-1.840	0.808	14.100
-17,800	-0.175	-1.810	0.808	14.100
-17,300	-0.171	-1.770	0.808	14.100
-16,600	-0.164	-1.700	0.809	14.200
-15,600	-0.154	-1.590	0.809	14.200
-14,000	-0.138	-1.430	0.810	14.200
-11,800	-0.117	-1.210	0.811	14.200
-9,160.0	-0.090	-0.934	0.812	14.200
-6,120.0	-0.060	-0.624	0.815	14.300
-3,230.0	-0.032	-0.329	0.818	14.300
-1,080.0	-0.011	-0.110	0.822	14.400
444.00	0.004	0.045	0.826	14.500
1,590.0	0.016	0.162	0.830	14.500
2,490.0	0.025	0.254	0.834	14.600
3,220.0	0.032	0.329	0.838	14.700
3,820.0	0.038	0.390	0.842	14.700
4,190.0	0.041	0.427	0.847	14.800
4,280.0	0.042	0.437	0.851	14.900
4,280.0	0.042	0.436	0.855	15.000
4,250.0	0.042	0.433	0.858	15.000
4,230.0	0.042	0.431	0.861	15.100
4,220.0	0.042	0.430	0.863	15.100
4,220.0	0.042	0.430	0.864	15.100
4,220.0	0.042	0.430	0.864	15.100
4,210.0	0.042	0.430	0.865	15.100
4,210.0	0.042	0.430	0.865	15.100
4,210.0	0.042	0.430	0.865	15.100
4,210.0	0.042	0.429	0.865	15.100
4,210.0	0.042	0.429	0.865	15.100
4,210.0	0.042	0.429	0.865	15.100

Table A8. Data of potential flow solution from Dressler (1978) and numerical solution from Run RN4, in comparison to the potential flow solution.

X [m]	Y [m]	Y/d	U [m/s]	U/Umax	Ri [m]	d [m]	y' [m]
1.64	0.8080	14.200	-	-	0.0191	0.0572	-
1.64	0.8080	14.200	3.2430	0.4340	0.0191	0.0572	0.0000
1.64	0.8080	14.200	5.2458	0.7010	0.0191	0.0572	0.0001
1.64	0.8080	14.200	6.1546	0.8230	0.0191	0.0572	0.0001
1.64	0.8080	14.200	6.7842	0.9070	0.0191	0.0572	0.0002
1.64	0.8080	14.200	7.2012	0.9630	0.0191	0.0572	0.0004
1.64	0.8090	14.200	7.4215	0.9920	0.0191	0.0572	0.0006
1.64	0.8090	14.200	7.4815	1.0000	0.0191	0.0572	0.0010
1.64	0.8100	14.200	7.3829	0.9870	0.0191	0.0572	0.0016
1.64	0.8110	14.200	7.1208	0.9520	0.0191	0.0572	0.0026
1.64	0.8120	14.200	6.7360	0.9010	0.0191	0.0572	0.0041
1.64	0.8150	14.300	6.2711	0.8380	0.0191	0.0572	0.0066
1.64	0.8180	14.300	5.8035	0.7760	0.0191	0.0572	0.0104
1.64	0.8220	14.40	5.4161	0.7240	0.0191	0.0572	0.0144
1.64	0.8260	14.500	5.1247	0.6850	0.0191	0.0572	0.0184
1.64	0.8300	14.500	4.8963	0.6550	0.0191	0.0572	0.0224
1.64	0.8340	14.600	4.6498	0.6220	0.0191	0.0572	0.0264
1.64	0.8380	14.700	4.1737	0.5580	0.0191	0.0572	0.0304
1.64	0.8420	14.800	3.2681	0.4370	0.0191	0.0572	0.0344
1.64	0.8460	14.800	2.2434	0.3000	0.0191	0.0572	0.0384
1.64	0.8500	14.90	1.4431	0.1930	0.0191	0.0572	0.0424
1.64	0.8540	15.000	0.8243	0.1100	0.0191	0.0572	0.0464
1.64	0.8580	15.000	0.3798	0.0508	0.0191	0.0572	0.0504
1.64	0.8610	15.100	0.1153	0.0154	0.0191	0.0572	0.0529
1.64	0.8630	15.100	- 0.0324	- 0.0043	0.0191	0.0572	0.0545
1.64	0.8640	15.100	- 0.1207	- 0.0161	0.0191	0.0572	0.0555
1.64	0.8640	15.100	- 0.1766	- 0.0236	0.0191	0.0572	0.0561
1.64	0.8650	15.100	- 0.2208	- 0.0295	0.0191	0.0572	0.0565
1.64	0.8650	15.100	- 0.2602	- 0.0348	0.0191	0.0572	0.0568
1.64	0.8650	15.100	- 0.2847	- 0.0381	0.0191	0.0572	0.0569
1.64	0.8650	15.200	- 0.2705	- 0.0362	0.0191	0.0572	0.0570
1.64	0.8650	15.200	- 0.1980	- 0.0265	0.0191	0.0572	0.0571
1.64	0.8650	15.200	-0.0961	-0.0128	0.0191	0.0572	0.0571
1.64	0.8650	15.200	-	-	0.0191	0.0572	0.0571
1.64	0.8080	14.200	-	-	0.0191	0.0572	-